Anatomically Informed Image Reconstruction for Time of Flight Positron Emission Tomography

Palak Wadhwa

University of Leeds

Biomedical Imaging Science Department

School of Medicine

Faculty of Medicine and Health

&

Invicro

Submitted in accordance with the requirements for the degree of

Doctor of Philosophy

February 20, 2020

Intellectual Property and Publications

The candidate confirms that the work that has been submitted in this thesis is her own, except where work which has formed part of jointly authored publications has been included. The contribution of the candidate and the other authors to this work has been explicitly indicated in this thesis. The candidate also confirms that appropriate credit has been given where reference has been made to the work of others.

Joint Publications

Work from the following jointly authored publications, which are listed in the Bibliography, is included in this thesis:

Journal papers

Palak Wadhwa, Kris Thielemans, Nikolaos Efthymiou, Kristen Wangerin, Nicholas Keat, Elise Emond, Timothy Deller, Ottavia Bertolli, Daniel Deidda, Gaspar Delso, Michel Tohme, Floris Jansen, Roger Gunn, William Hallett and Charalampos Tsoumpas. PET Image Reconstruction Using Physical and Mathematical Modelling For Time of Flight PET-MR Scanners in the STIR Library. In *Methods; **2020***. URL : https://doi.org/10.1016/j.ymeth.2020.01.005

The candidate had the main contribution towards this paper. She designed the PET image reconstruction implementation in STIR library for the time-of-flight scanner and implemented the required classes and utilities in the C++ programming language proposed. She also proposed and carried out intensive testing to validate all the implementations using real datasets. She performed all the image reconstructions and image analysis, as well as paper writing. She also conducted PET/MR scans along with co-author Nicholas Keat and acquired phantom datasets.

Co-authors, Kris Thielemans, Nikos Efthymiou, Elise Emond, Ottavia Bertolli and Daniel Deidda, have implemented the basic building blocks in the STIR library. Co-authors, Kristen Wangerin, Timothy Deller, Michel Tohme, Floris Jansen and Gaspar Delso, provided the vendor's reconstruction software. Gaspar Delso also provided one phantom dataset used in this paper. Co-author, Nicholas Keat has reviewed the paper to provide corrections. The last three co-authors supervised the project, provided patient dataset, acquired the ethical review and funding.

Mercy I Akerele, **Palak Wadhwa**, Jesus Silva-Rodriguez, William Hallett and Charalampos Tsoumpas. Validation of the physiological background correction method for the suppression of the spill-in effect near highly radioactive regions in positron emission tomography. In *EJNMMI Physics*, 2018, volume 5, pages 34. URL : https://doi.org/10.1186/s40658-018-0233-8.

The candidate had a major contribution in this paper as she developed the STIR code that was required to reconstruct the images for phantom and patient scans from GE SIGNA PET/MR. She proposed the phantom scan and acquired the real phantom dataset presented in this paper. The candidate supported the first author by providing necessary training and support to reconstruct images using STIR for this paper and then also conducted all the reconstructions using

different reconstruction algorithms that were used for analysis and presented in the supplementary material for this paper.

The first author, Mercy I Akerele implemented the study, conducted the image reconstructions, image analysis and wrote the paper. The co-author, Jesus Silva-Rodriguez provided advice on the methodology of this paper. The co-author, William Hallett provided the patient dataset and acquired the ethical review. The co-author, Charalampos Tsoumpas is responsible for the conceptualisation of the idea, supervision, paper review and corrections.

Nikos Efthimiou, Elise Emond, **Palak Wadhwa**, Christopher Cawthorne, Charalampos Tsoumpas and Kris Thielemans. Implementation and validation of time-of-flight PET image reconstruction module for listmode and sinogram projection data in the STIR library. In *Physics in Medicine & Biology*, 2019, volume 64, pages 035004. URL : https://doi.org/10.1088/1361-6560/aaf9b9.

The candidate had a minor role in this paper which was mainly focussed on testing the implemented code. She implemented a test classes in C++ language for validating the time-of-flight (TOF) implementations as reported in the paper and then she performed intensive tests to debug the code which had a pivotal role in the final code release.

The first author Nikos Efthimiou implemented the C++ code as described in the paper in the STIR library, performed GATE simulations, conducted tests to validate the code and wrote the paper. The coauthor Elise Emond helped in debugging and code testing. Co-authors Christopher Cawthorne, Charalampos Tsoumpas and Kris Thielemans supervised the project, helped in code development and reviewed the paper for corrections.

Evgueni Ovtchinnikov, Richard Brown, Christoph Kolbitsch, Edoardo Pasca, Casper da Costa-Luis, Ashley G. Gillman, Benjamin A. Thomas, Nikos Efthimiou, Johannes Mayer, **Palak Wadhwa**, Matthias J Ehrhardt, Sam Ellis, Jakob S. Jørgensen, Julian Matthews, Claudia Prieto, Andrew J. Reader, Charalampos Tsoumpas, Martin Turner, David Atkinson and Kris Thielemans. SIRF: Synergistic Image Reconstruction Framework. In *Computer Physics Communication: **2020***, volume 249, pages 107087. URL : https://doi.org/10.1016/j.cpc.2019.107-087.

The candidate had a substantial role in this paper and she implemented a part of the C++ code for the hybrid kernel expectation maximisation class and also developed the C++ code for PET image reconstruction from the data extracted from GE SIGNA PET/MR. The code is developed using the STIR library.

The main author and most of the co-authors were involved in code development and all authors were involved in paper writing and revisions.

Conference Papers

Palak Wadhwa, Kris Thielemans, Ottavia Bertolli, Nikos Efthimiou, Elise Emond, Benjamin A. Thomas, Michel Tohme, Gaspar Delso, William Hallett, Roger Gun, David Buckley and Charalampos Tsoumpas. Implementation of Image Reconstruction for GE SIGNA PET/MR PET Data in the STIR Library. In *Nuclear Science Symposium and Medical Imaging Conference Proceedings (NSS/MIC).* IEEE, 2018, Sydney, Australia, pages: 1-3. URL: https://doi.org/1-0.1109/NSSMIC.2018.8824341

The candidate had the main role in this paper. She proposed and implemented all the C++ code within the STIR library. She conducted all the phantom scans, image reconstructions, image analysis and paper writing.

The co-authors were responsible for provide phantom and patient datasets.

Mercy I Akerele, **Palak Wadhwa**, Stefaan Vanderberghe and Charalampos Tsoumpas. Comparison of Partial Volume Correction Techniques for Lesions Near High Activity Regions. In *Nuclear Science Symposium and Medical Imaging Conference Proceedings (NSS/MIC).* IEEE, 2017, Atlanta, Georgia.

The candidate had a major role in this paper as she implemented the C++ code in the STIR library which has been utilized in this paper to reconstruct datasets. She also provided hands-on support and training to the first author whenever necessary to reconstruct datasets from GE SIGNA PET/MR.

The first author is responsible for image reconstructions, image analysis and paper writing. The co-authors are responsible for paper review.

Evgueni Ovtchinnikov, David Atkinson, Christoph Kolbitsch, Benjamin A. Thomas, Ottavia Bertolli, Casper O. da Costa-Luis, Nikolaos Efthimiou, Ronald Fowler, Edoardo Pasca, **Palak Wadhwa**, Elise Emond, Julian Matthews, Claudia Prieto, Andrew J. Reader, Charalampos Tsoumpas, Martin turner and Kris Thielemans. SIRF: Synergistic Image Reconstruction Framework. In *Nuclear Science Symposium and Medical Imaging Conference Proceedings (NSS/MIC).* IEEE, 2017, Atlanta, Georgia.

The candidate had a minor role in this paper. She acquired the phantom scan, implemented the software framework to reconstruct the PET dataset for GE SIGNA PET/MR and reconstructed the PET image for the phantom dataset.

All other authors were involved in developing and testing of the code. The first author wrote the paper.

Conference Abstracts

Palak Wadhwa, Kris Thielemans and Charalampos Tsoumpas. Validation of Recent Developments in STIR Library for GE SIGNA PET/MR Scanner Using Real Data. In *Conference on Bio-Medical Instrumentation and Related Engineering and Physical Sciences.* BIOMEP 2017, University of West Attica, Greece (Oral Presentation).

Palak Wadhwa, Kris Thielemans, Ottavia Bertolli, Nikos Efthimiou, Elise Emond, Benjamin A. Thomas, Michel Tohme, Gaspar Delso, William Hallett, Roger Gun, David Buckley and Charalampos Tsoumpas. Implementation and Validation of Image Reconstruction for PET Data from GE SIGNA PET/MR Scanners In the STIR Library. In *Nuclear Science Symposium-Medical Imaging Conference.* IEEE 2018, Sydney, Australia (Poster Presentation).

Palak Wadhwa, Nikos Efthimiou, Kris Thielemans, Elise Emond, Kristen A. Wangerin, Gaspar Delso, Steven J. Archibald, William Hallett, Roger Gunn, David Buckley and Charalampos Tsoumpas. Validation of Time-of-Flight Image Reconstruction for GE SIGNA PET/MR Scanner Using STIR Toolkit. In *8th Conference on PET/MR and SPECT/MR,* 2019, Munich, Germany (Poster Presentation).

Palak Wadhwa, Daniel Deidda, Kris Thielemans, William Hallett, Roger Gunn, David Buckley and Charalampos Tsoumpas. Anatomically Informed Time-of-Flight PET Image Reconstruction with STIR Toolkit. In *15th European Molecular Imaging Meeting.* EMIM 2020, Thessaloniki, Greece (Poster Presentation).

Mercy I Akerele, **Palak Wadhwa**, Stefaan Vandenberghe and Charalampos Tsoumpas. Comparison of Partial Volume Correction Techniques for Lesions Near High Activity Regions. In *Nuclear Science Symposium and Medical Imaging Conference.* IEEE, 2017, Atlanta, Georgia (Oral Presentation).

Mercy Akerele, Nikos Efthimiou, **Palak Wadhwa**, Jesus Silva-Rodriguez and Charalampos Tsoumpas. Impact and Correction of the Bladder Uptake on Tumor Quantification. In *Nuclear Science Symposium and Medical Imaging Conference.* IEEE, 2016, Strasbourgh, France (Poster Presentation).

Evgueni Ovtchinnikov, David Atkinson, Christoph Kolbitsch, Benjamin A. Thomas, Ottavia Bertolli, Casper O. da Costa-Luis, Nikolaos Efthimiou, Ronald Fowler, Edoardo Pasca, **Palak Wadhwa**, Elise Emond, Julian Matthews, Claudia Prieto, Andrew J. Reader, Charalampos Tsoumpas, Martin Turner and Kris Thielemans. SIRF: Synergistic Image Reconstruction Framework. In *Nuclear Science*

Symposium and Medical Imaging Conference (NSS/MIC). IEEE, 2017, Atlanta, Georgia (Poster Presentation).

Awards

The awards and bursaries that funded entire and parts of this work are included below.

1. This research is funded by a Medical Research Council Industrial CASE PhD Scholarship (MR/M01746X/1). The scholarship awarded by Medical Research Council covered stipend, fees (at national rate), consumables and travel. The total award was approximately £146,000.

2. This research is also partly funded by Invicro (Imanova Bursary) that covered small sum of stipend and other consumables including experimental costs and travel.

3. CCP PET MR Exchange Programme Grant was awarded as a part of this work to incorporate the implementations made in open-source software, Software for Tomographic Image Reconstruction (STIR) and Synergistic Image Reconstruction Framework (SIRF).

4. CCP PET MR 2020 Gold Award was awarded to the candidate for her contributions to STIR for GE SIGNA PET/MR data handling.

Acknowledgements

I would like to express my deepest gratitude to my supervisors Dr. Charalampos Tsoumpas, Prof. David Buckley and Dr. William Hallett (Invicro) for their supervision, support and motivation throughout the PhD. Their critical feedback and honest comments were very beneficial for my scientific development and have helped me improve significantly. I would like to offer my special thanks to Dr. Charalampos Tsoumpas for the acquired MRC funding, which allowed me to undertake this project. I would also like to express my gratitude to Prof. Roger Gunn (Invicro) for being my supervisor which allowed me to collaborate with Invicro, London, UK. This was positive as this allowed me to understand the industrial aspect of Positron emission tomography (PET) research. This collaboration was helpful to acquire clinical and phantom datasets which also provided me with hands-on experience.

I would like to offer my special thanks to Prof. Kris Thielemans (University College London) for his great support towards the main implementations that were necessary to reconstruct real datasets from the GE SIGNA PET/MR scanner. I would also like to thank him for supporting the integration of my development within open-source software which is a major contribution of this thesis. I would like to thank the Collaborative Computational Project in Positron Emission Tomography and Magnetic Resonance imaging (CCP PET MR) as it allowed me to collaborate with Prof. Kris Thielemans by funding my visit to the Institute of Nuclear Medicine, UCL in London.

I would like to thank my collaborators from GE Healthcare, Dr. Kristen Wangerin, Dr. Floris Jansen, Dr. Michel Tohme and Dr. Timothy Deller for their beneficial insight and support which helped me to make all the developments possible.

I would like to thank Dr. Daniel Deidda (National Physics Laboratory), Dr. Nikos Efthimou (University of York), Dr. Elise Emond (Brainlab), Dr. Nicholas Keat (Invicro), Prof. Stefaan Vandenberghe (University of Ghent), Prof. Michel Koole (KU Leuven) and Ms Ester D'Hoe for their initial support and help in making this project a possibility. I would further like to thank Leeds Institute of Cardiovascular and Metabolic Medicine (LICAMM) for providing a conducive environment which allowed me to undertake the PhD with maximum possible

support. I would also like to thank Martin Plumb and Ian Wilson for their support and help at all instances with IT.

Finally, I would like to give my heartiest thanks to my family, mom (Vanita), dad (Neeraj) and Ansh without whom this would not have been possible at all. Their unconditional support in all areas is unmatched and the only reason I could make this through. Their motivation helped me go even further than I could have ever imagined. Thank you so much for being my backbone during this journey and being my support which allowed me to reach the top of the mountain. And lastly, I wish to thank you nanu (Ramesh Chandra Salhotra), nanima (Kanta Salhotra) and dadu (Sudhama Krishna Wadhwa) for your blessings which are priceless.

Abstract

PET has an important role in disease diagnosis, drug development and patient management. PET images are accompanied with computed tomography (CT) or magnetic resonance (MR) to provide the complementary structural information. GE SIGNA PET/MR is the state-of-the-art clinical scanner that aims at combining TOF-PET with anatomical and soft-tissue MR imaging. This work aims at modelling the mathematical and physical processes of TOF-PET data for the GE SIGNA PET/MR within an open-source software, STIR. This work further examines the developments made to implement the acquisition model using typical (ordered subsets expectation maximisation (OSEM)) and advanced iterative algorithms (TOF-OSEM and TOF-kernelised expectation maximisation (KEM)).

TOF-PET improves conventional PET imaging as it localises the event along the line of response (LOR) within a small region with an uncertainty which is calculated using the timing resolution of the detectors. It demonstrates robustness despite the presence of small errors, inconsistencies or patient motion in the acquired data. The GE SIGNA PET/MR have a timing resolution of 390 ps. The aim of this work is to exploit TOF-PET and further include the anatomical information from MR images to facilitate robust PET reconstructions.

All the developments made in this thesis were compared with the vendor's reconstruction software (GE-toolbox). Real phantom and clinical datasets were used for the analysis. The calculated emission and data corrections using developments made in STIR were in excellent agreement with the GE-toolbox despite the absence of dead-time and decay effects within the current developments. Reconstructions using OSEM and TOF-OSEM algorithms demonstrated a good agreement with the GE-toolbox concerning quantitative, resolution and structural based analysis. TOF-KEM reconstructions demonstrated a slight improvement in quantification as compared to TOF-OSEM with STIR.

The thesis demonstrates the first instance of real data reconstruction for TOF-PET data using TOF-OSEM and TOF-KEM algorithms. The developments made in this thesis provide a platform to investigate the effects of a novel reconstruction algorithm, TOF-KEM on the dose and scan time reduction using real clinical datasets.

Contents

Acronyms

[^{18}F]FDG	[^{18}F]-fluorodeoxyglucose. 12, 14, 15
[^{18}F]NaF	[^{18}F]-sodium fluoride. 15
2-D	2-dimensional. xxiii, 23
3-D	3-dimensional. xxv, 19, 76, 88
AC	attenuation correction. xxiv, xxv, 50, 59, 60, 79, 80
ACD	annihilation coincidence detection. 17
APD	Avalanche photodiode. 59
BGO	Bismuth germanium oxide. 17, 18
CT	computed tomography. xi, 2, 13, 14, 50, 52, 53, 57–59, 81
DICOM	Digital Imaging & COmmunication in Medicine. 73, 74, 81
ET	Emission Tomography. 64
FOV	field of view. xxiii, 13, 18–20, 77, 92, 93
FWHM	Full Width Half Maximum. xv, xvi, xxviii, xxix, xxxiii, 100, 102, 107, 118–124, 146
HDF5	Hierarchical Data Format 5. 73–76, 82, 86

HKEM	hybrid kernelised expectation maximisation. 65
ID	identifiers. 76
KEM	kernelised expectation maximisation. xi, xiv, xv, xxiv, xxv, 4, 7–9, 67, 68, 79, 80, 93, 95, 105
LM	Listmode. xiv, 19, 26, 27, 39, 65, 66, 72–76, 82, 85
LOR	line of response. xi, xxiii, xxiv, 3, 16, 17, 19–22, 24, 27, 29, 40, 42, 45, 49, 52, 73, 76–78, 84
LSO	lutetium oxyorthosilicate. 17, 59
LYSO	lutetium-yttrium oxyorthosilicate. 18, 19, 59
MLEM	Maximum likelihood expectation maximisation. 31, 34, 39, 40
MR	magnetic resonance. xi, xiv, xxiv, xxv, xxxiii, 1–10, 14, 45, 50, 52, 54, 57–61, 66–69, 71, 73, 83, 87–89, 92, 93, 96, 105, 158
MRAC	Magnetic Resonance Attenuation Correction. xiv, xxiv, xxv, 59, 60, 72–74, 78–81
NaI[Tl]	thallium-doped sodium iodide. 18
NMV	Net Magnetisation Vector. 55, 57
OSEM	ordered subsets expectation maximisation. xi, 9, 39, 40, 53, 66, 72

PET	Positron emission tomography. ix, xi, xiv, xxiii–xxv, xxxiii, 1–14, 17–20, 23–26, 29, 40, 43–45, 49–54, 57–61, 64–69, 71, 73, 74, 81–83, 87–90, 92, 93, 96, 105, 107, 143, 156
PIFA	PET Image For Attenuation. xxiv, xxv, 73, 74, 78–81, 83
PLS	parallel level sets. 65
PMT	photomultiplier tube. 18, 59
PSF	point spread function. 145
RF	Radio Frequency. 55, 57
ROI	region of interest. 71
SIRF	Synergistic Image Reconstruction Framework. vii, xiv, 7, 66
STIR	Software for Tomographic Image Reconstruction. vii, xi, xiv, xv, xxiv, xxv, 4, 6–8, 44, 54, 64–67, 69, 71, 72, 74–76, 79–85, 87–89, 92, 93, 96, 98, 99, 105, 107, 108
SUVR	Standardised Uptake Value Ratio. xv, xvi, xxxiii, 102, 107, 125, 126, 134, 147, 148, 152
TOF	time-of-flight. iii, xi, xiv–xvi, xxiv, xxv, 3, 4, 6–9, 19, 52–54, 60, 68, 69, 71, 73, 76, 79, 80, 84, 88–96, 98, 99, 101, 105, 107–109, 112, 143, 146, 147
US	Ultrasound. 57
UTE	ultrashort echo time. 60
UV	ultraviolet. 18
ZTE	zero echo time. 60, 74

List of Figures

List of Tables

Chapter 1

Introduction

1.1 Context and Motivation

Positron emission tomography (PET) and magnetic resonance (MR) modalities are complementary imaging modalities (Lasocki and Hicks [2019]). PET provides highly specific and sensitive in vivo images of molecular and metabolic information, whereas, MR provides high-resolution images of anatomical and functional information (Lasocki and Hicks [2019]). The ability of PET to detect molecular abnormality along with the MR to detect and anatomically localise the lesion can be used in a complementary manner to improve the diagnostic accuracy and further remove the need for biopsy. Particularly, the combination of PET and MR has demonstrated to be beneficial in neuro-oncology. MR is used as a standard clinical test in neuro-oncology and particular MR sequences such as T1-weighted, T2-weighted and diffusion-weighted imaging are used to indicate the intracranial lesions. Lasocki and Hicks (2019) have discussed that the PET imaging using newer radio-tracers which target specifically neuro-endocrine tumours such as

gallium-68 labelled 1,4,7,10-tetraazacyclododecane-N,N',N",N"'-tetraaceticacid-Tyr3-octreotate (GaTate), when combined with the MR, demonstrates accurate detection (due to PET and MR) and localisation (due to MR) of the intracranial lesions. Combining PET and MR imaging has also demonstrated to be important in patient management and therapy planning. Similarly, PET/MR can provide complementary information in cardiology and oncology using MR techniques such as cine-MRI and novel PET radio-tracers. This has led to the incorporation of PET and MR into single systems. Although the hardware components of PET and MR are incorporated together, there is a lack of synergistic imaging for these modalities (Ovtchinnikov et al. [2020]). This lack has created a detrimental effect on the motivation for using the combined PET/MR modality. Unlike the combination of PET with computed tomography (CT), which produces combined output that is greater than the sum of the individual, combined PET/MR has not yet conclusively demonstrated an advantage over the individual modalities (Mayerhoefer et al. [2020]). The combination of PET with CT had led to a significant improvement in PET images and clinical diagnosis as CT provided the attenuation map which is significant for PET data correction. Although PET/MR has demonstrated to provide complementary information, it has a major drawback due to the cost of the scanner installation and maintenance. Further, PET/MR has lower patient throughput as compared to PET/CT (Mayerhoefer et al. [2020]).

The availability of pre-developed open-source software, with the ability to read raw PET and MR data, can overcome the challenging nature of implementing and validating novel image reconstruction algorithm for multi-modality scanners. This can also remove the need for duplication of utilities required to

read raw PET/MR data and implementation of iterative reconstruction algorithms for PET/MR scanners at different scientific sites by offering a platform for collaboration (Ovtchinnikov et al. [2020]). To facilitate the software development for combined PET/MR scanners, part of this thesis includes the development and implementation of the software necessary to reconstruct time-of-flight (TOF)-PET data extracted from the GE SIGNA PET/MR scanner and make it available as a part of open-source software (Wadhwa et al. [2020]).

The concern with clinically used reconstruction techniques is that they demonstrate an inherent increase in statistical noise over iterations (Jaskowiak et al. [2005]). The statistical noise affects image quantification and lesion detectability. The reconstructions are stopped after 2 or 3 iterations so that the images are not degraded by the noise and this may lead to less accurate quantification (Ahn et al. [2015], Akerele et al. [2017]). TOF-PET imaging reduces the image noise and improves image contrast (Surti [2015]). Further, TOF-PET reconstruction also demonstrates robustness by reducing the effect of data inconsistency and patient motion (Conti [2010], Surti [2015], Turkington and Wilson [2009]). This is because the TOF information limits the coincident event spatially along the line of response (LOR) using a spatial weighting factor which is dependent on the timing resolution of the scanner. This spatial weighting of TOF competes with the spatial weighting of inconsistent attenuation or normalisation factors and corrects the data (Conti [2010], Mehranian and Zaidi [2015]). Similarly, the events affected by motion are accurately localised along the LOR using the TOF information. The combination of PET and MR modality also provides an opportunity to improve image quantification with imaging algorithms that can exploit the cross-modality similarities which can thus prove to be advantageous for both

PET and MR individual images (Ovtchinnikov et al. [2020]). The kernelised expectation maximisation (KEM) algorithm uses anatomy-based kernels to guide PET reconstruction which further reduces iterative noise build-up (Wang and Qi [2014], Deidda et al. [2018b, 2019]). This thesis aims at improving PET image quantification by using MR information with reconstruction for TOF-PET data (Wang and Qi [2014], Deidda et al. [2018b], Efthimiou et al. [2019], Wadhwa et al. [2020]). It demonstrates reconstructions with novel iterative reconstruction algorithms for the GE SIGNA PET/MR.

KEM iterative reconstruction algorithm (Deidda et al. [2018b, 2019], Wang and Qi [2014]) along with TOF-PET imaging (Efthimiou et al. [2019], Wadhwa et al. [2020]) can help to reduce injected dose and scan times, whereas, this requires future investigation (Surti [2015], Deidda et al. [2018b]).

1.2 Purpose of the Thesis

The main goal of this thesis is to develop and implement advanced image reconstruction techniques by combining TOF-PET imaging with kernelised reconstruction. This overarching goal was achieved by dividing the developments into sub-parts:

1. Model and implement the non-TOF and TOF PET acquisition process for GE SIGNA PET data within the open-source software, Software for Tomographic Image Reconstruction (STIR). The mathematical and physical modelling of the acquisition process for GE SIGNA PET/MR scanner in open-source library, STIR, has not been done before as this scanner is a recent clinical scanner. Further, GE SIGNA PET/MR processes the PET

data differently to the previously implemented scanners within STIR. Particularly, it has its own conventions and data organisation. Thus, in order to reconstruct the data acquired from this scanner using the open-source library, it was a necessity to incorporate the scanner and its acquisition process within STIR.

2. Implement the calculation of the correction factors for the effects that degrade the PET image reconstructions for GE SIGNA PET data such as normalisation, randoms and background effects. All the implementations are carried out using the measurements extracted from the GE SIGNA PET/MR.

3. Expand STIR library by introducing various new classes and utilities to read and process GE data formats.

4. Validate the above implementations by comparing the results calculated with STIR with those calculated using the vendor's reconstruction software (referred to as GE-toolbox in this thesis). GE-toolbox has been created with greater details about the scanner as they manufactured the scanner and can model it with finer accuracy within the software. The approach demonstrated in this thesis is an approximation to the GE scanner, and hence, it is compared with the GE-toolbox. For example, the scanner is not an exact cylinder, but STIR library approximates it as such, whereas, GE-toolbox accounts for the non-cylindrical geometry of the scanner within the system matrix. Further, GE-toolbox is a proprietary closed-source software and a black-box, and the acquisition process modelled within the software is not known. The implementations made during this work demonstrates

an effort to make the acquisition model available as a part of the open-source software, STIR, which now allows the reconstruction of PET data acquired from the GE SIGNA PET/MR scanner. The comparison of final reconstructions using STIR with the GE-toolbox are of major importance to ensure that the implementations made within the open-source software are accurate and the scanner is modelled to the best possible approximation. Also to point out the complexity of this implementation, it is necessary to understand that the underlying acquisition model was improved iteratively by rigorously comparing the reconstructions using STIR with the GE-toolbox. Thus, the scanner and acquisition process was modelled to the highest possible accuracy within the given limitation of GE-toolbox being a black-box.

5. Demonstrate and validate both routine and advanced image reconstruction techniques (including TOF and kernelised reconstruction) and compare them against the GE-toolbox reconstructions. The advanced reconstruction algorithm TOF-KEM is the novel part of this thesis and reconstructions with real scanner data using this algorithms has not been demonstrated before.

This thesis provides a platform for the PET research community to use the current implementations and reconstruct non-TOF and TOF PET data extracted from any current GE PET scanner.

This thesis also provides methods to recover the PET activity and reduce noise by using MR anatomical information (Deidda et al. [2018b], Wadhwa et al. [2020]). Further, this thesis also provides a novel reconstruction algorithm, TOF-KEM for clinical PET/MR scanners.

1.3 Key Contributions of the Thesis

The main contribution of this thesis are summarised below:

1. Classes to handle PET data from GE SIGNA PET/MR are implemented in STIR.

2. TOF-KEM algorithm was implemented for TOF-PET data and validated for the first time with real data.

3. All work in the thesis is available or will be available soon, as part of STIR and Synergistic Image Reconstruction Framework (SIRF), as open-access software.

The contributions made in this thesis will further allow all current and future STIR users to produce accurate reconstructions with GE SIGNA PET/MR without the need of re-investigating the developments. The thesis contributes to the PET community by providing an important tool with substantial examples of incorporating a new clinical scanner in open-source software. The developments made in this thesis not only provide a platform to reconstruct PET data from GE SIGNA PET/MR but will allow other users to reconstruct data acquired from any GE PET scanner using conventional and advanced reconstruction algorithms mentioned in this thesis. This is because the software implemented during this thesis can be used to reconstruct data from any clinical GE scanner as most acquired data from GE scanners have the same format. Further, the users can reconstruct GE PET data using novel TOF-KEM algorithm as demonstrated within this work can be majorly beneficial for studies with lower count rates.

1.4 Thesis Overview

There are six chapters in this thesis that describe the major implementations made to incorporate the first TOF PET-MR scanner model ever available in an open-source emission tomography reconstruction software and its applications in the clinical environment. The thesis chapters are summarised below in order to provide an overview of the entire thesis:

Chapter 2: Background

This chapter discusses the necessary background to lay the foundation of the thesis. It starts by explaining the basics of PET and introduces the data acquisition procedure in conventional scanners. It then progresses to explain the mathematical formulation of the typically used image reconstruction algorithms and the available methods for correcting PET data due to degrading effects. Finally, this chapter discusses the background of the novel iterative reconstruction algorithms used in this thesis as well as all relevant software.

Chapter 3: Methods

This chapter presents the implementation of physical and mathematical methods required to model the scanners acquisition process in STIR library. This chapter initially focuses on TOF and non-TOF PET data implementation from GE SIGNA PET/MR within the STIR library. It further develops the theory behind TOF-KEM reconstruction method. It then describes the acquired phantom and clinical data and summarises the reconstruction setup and statistical image analysis methods used for validation of the reconstructions. The software devel-

opment, data acquisitions, reconstruction setup and image analysis presented in this chapter are published in Wadhwa et al. [2018, 2020] and were presented as a poster at IEEE Medical Imaging Conference, Sydney, Australia, 2018 and 8^{th} Conference on PET-MR and SPECT/MR, Munich, Germany, 2019.

Chapter 4: Results

This chapter presents the results which compare the iterative reconstructions for the datasets with the vendor's reconstruction software. The emission and data corrections histograms are also compared with the vendor's extracted histogram and corrections. It further describes findings that demonstrate the improvement in image quality for reconstructed images with the TOF-KEM method for real data. This chapter compares quantitatively the images reconstructed for patient and phantom datasets with standard (ordered subsets expectation maximisation (OSEM) and TOF-OSEM) and novel (TOF-KEM) iterative reconstruction algorithms. The results presented in this chapter are published in Wadhwa et al. [2018, 2020] and were presented as a poster at the IEEE Medical Imaging Conference, Sydney, Australia, 2018 and at the 8^{th} Conference on PET-MR and SPECT/MR, Munich, Germany, 2019.

Chapter 5: Discussion

This chapter discusses the results that are demonstrated in Chapter 4 and highlights the similarities between GE-toolbox and STIR-based calculated emission and data correction histograms. It also illustrates the quantitative comparison of the performance of clinical and novel iterative reconstruction algorithms. Part of this chapter is published in Wadhwa et al. [2018, 2020] and was presented as

a poster at the IEEE Medical Imaging Conference, Sydney, Australia, 2018 and at the 8^{th} Conference on PET-MR and SPECT/MR, Munich, Germany, 2019.

Chapter 6: General Conclusion and Future Work

This chapter summarises the most important findings of the thesis and discusses further potential opportunities that have been created by this work.

1.5 Ethical Review

Patient scans acquired under a clinical study performed at Invicro with the ethics number 17/ WM/0084.

Chapter 2

Background

2.1 PET

2.1.1 Introduction to PET

PET is a non-invasive imaging modality that is widely employed in clinical diagnosis, patient management (Sachs and Bilfinger [2005]), drug development (Matthews et al. [2012]), treatment response (Stasa and Rajer [2015]) and clinical research. The modality has proven to be highly specific and sensitive to detect the uptake of radio-labelled molecules in vivo (Jones [1996]) which can explain its widespread use as discussed previously. The specificity of the PET modality is due to the radiolabelled molecules available that can be attached to the specific biomarkers and pharmaceuticals that target the specific organ functions. The sensitivity of the PET modality is due to the electronic collimation of the PET detectors as discussed later in section 2.1.1. The main areas of clinical applications of PET include:

- Neurology: PET allows quantification of cerebral blood flow, metabolism,

oxygen consumption in different parts of the brain and receptor binding for initial diagnosis and assessment of brain tumours, epilepsy, Parkinson's disease (Walker et al. [2018]), Alzheimer disease, dementia (Motara et al. [2017], Zhang et al. [2017]) and movement disorders (Gunn et al. [2015], Herholz and Heiss [2004]).

- Oncology: The measurement of the rate of consumption of the radiolabelled glucose analogue or [^{18}F]-fluorodeoxyglucose ([^{18}F]FDG) allows the quantification of metabolic activity for cancer diagnosis, staging, differentiation between malignant and benign tumours and treatment response (Kelloff et al. [2005], Price and Green [2011], Goelz et al. [1985]). PET can be used in patient management by assessing the response towards the therapy. This can help in the decision to continue or discontinue the therapy by measuring tumour size in the scanned images. Malignant tumours have higher metabolic activity rates than benign tumours (Goelz et al. [1985]). PET is not only helpful in disease diagnosis and patient management, but its applications extend to oncological drug development for lung, lymphoma, prostate, sarcoma, ovary, breast and colorectal cancers (Kelloff et al. [2005]).

- Cardiology: In ischemic heart failure, there is a metabolic shift that is reported from fatty acid consumption to glucose utilisation. Since PET can measure the myocardial glucose metabolism, it can be used as a diagnostic and patient management tool for myocardial ischemia. PET also allows the quantification and assessment of the myocardial perfusion and viability (Robson et al. [2017a]). Myocardial perfusion indicates reduced

blood flow through the heart vessels, which is localised using PET. This can provide a test for the narrowed or blocked heart vessels (Robson et al. [2017a]). Cardiac viability scans can further clinically indicate if there is a possibility of the heart muscles to go back to normal after placement of a coronary stent or surgically operating to reroute the blood flow along the coronary arteries (Robson et al. [2017a]). PET can also detect the calcium or plaque deposition in the coronary arteries which is related to atherosclerosis detection (Lindner and Sinusas [2013], Alie et al. [2014]).

As discussed above, PET is a highly successful molecular imaging modality in clinical imaging, therapy response and clinical research. PET is a sensitive modality that has evolved from collimated detectors based planar imaging techniques to a 25-cm long axial field of view (FOV) electronic collimator-based detection process, as discussed in detail in section 2.1.2. The FOV of PET scanners, which can image the human torso, is covered with thousands of detectors. A large number of detectors placed all around the radioactive object that is to be scanned makes PET a highly sensitive modality which can detect radiation emitted from very small quantities of injected radiotracers. The PET modality, is for instance, extremely successful in imaging molecular abnormalities, whereas it lacks the ability to localize it structurally (Blodgett et al. [2007], Jennings et al. [2015]). A modality that can provide structural information, such as CT, can be used alongside PET. The resulting image from PET and CT scans can be fused together to localise the abnormalities within the patient body. The PET and CT scans are conducted at separate times and are prone to inter-scan motion. The skull is mainly prone to rigid motion (although, neck, tongue and throat can move non-rigidly) which can be corrected for during the image fusion.

In contrast, motion correction is a major issue in the body due to significant deformations and large movements of the organs in the body. This drawback has lead to the development of hybrid imaging modalities such as PET/MR. The structural and the functional information can also be extracted from MR scans, which can be used as the complementary information to PET scans. The hybrid PET/MR scanners have an added advantage over the individual PET and MR scanners (Robson et al. [2017b]). The hybrid PET/MR is beneficial as MR has no ionising radiation. This makes it a low radiation hybrid modality as compared to PET/CT.

2.1.2 PET Radiotracers

A PET radioactive tracer or commonly known as radiotracer is a synthetic chemical compound comprising of a specific biomolecule (the molecule which is targeted to be taken up by a specific tissue or organ) where one or more of its atoms are replaced by a radio-isotope (Buechel et al. [2015]). The radio-isotopes are produced by accelerating and bombarding the protons or deuterons onto a stable target using a cyclotron (Gillings [2013]). When the biomolecule is taken up by the target tissue or organ, there is a freely available radio-isotope which decays naturally and contributes to the detected activity (Buechel et al. [2015]).

Over the past years, there has been an observed increase in the number of [^{11}C]-labelled, [^{13}N]-labelled and [^{18}F]-labelled radiotracers which has significantly contributed towards the success of PET imaging (Gunn et al. [2015]). These radiotracers are used to image a large range of molecular abnormalities that are present in the diseased or abnormal tissues. The most significant PET radiotracer that is used in the clinic is [^{18}F]FDG (Ido et al. [1978], Gillings [2013]).

[^{18}F]FDG has proven to be highly successful in brain imaging and tumour imaging. Another example of commonly used radiotracer is [^{18}F]-sodium fluoride ([^{18}F]NaF). [^{18}F]NaF is used to image the bones and plaques, for instance, in coronary arteries for atherosclerotic imaging (Kwiecinski et al. [2020]).

2.1.3 From Positron Emission to Photon Detection

A picomolar amount of radiotracer is administered within the body, and the molecule is taken up by the target tissue, which results in the radioligand being freely available within the tissue. The recommended dose for a 5 min acquisition and bed overlap of less than 25% is around 2.5 MBq per every kg of body weight (Boellaard et al. [2010]). The radioligand is proton-rich and unstable, which leads to the beta decay within its nucleus, where the proton gets converted to the neutron, emitting a positron and a neutrino. The positron resulting from the beta decay is antimatter, which travels a short distance within the tissue before losing all its energy due to its interactions. During its interaction with the atoms of the tissue, the positron is scattered by, the peripheral electrons by a small distance or 'range' (Lois et al. [2020]). After losing the kinetic energy, the positron then annihilates with a local electron causing an 'event' to occur, where a pair of γ rays (or photons) that travel at approximately 180° to each other are formed.

The rest mass, or m_0, of the electron and the positron is equal to 9.1×10^{-31} kg. The γ rays travel at the speed of light (c=3×10^8 m/s). According to conservation of energy, the emitted γ rays have energy of 0.511 MeV, where 1 MeV=1.6×10^{-13} J (kgm^2/s^2) and must travel in opposite directions to each other.

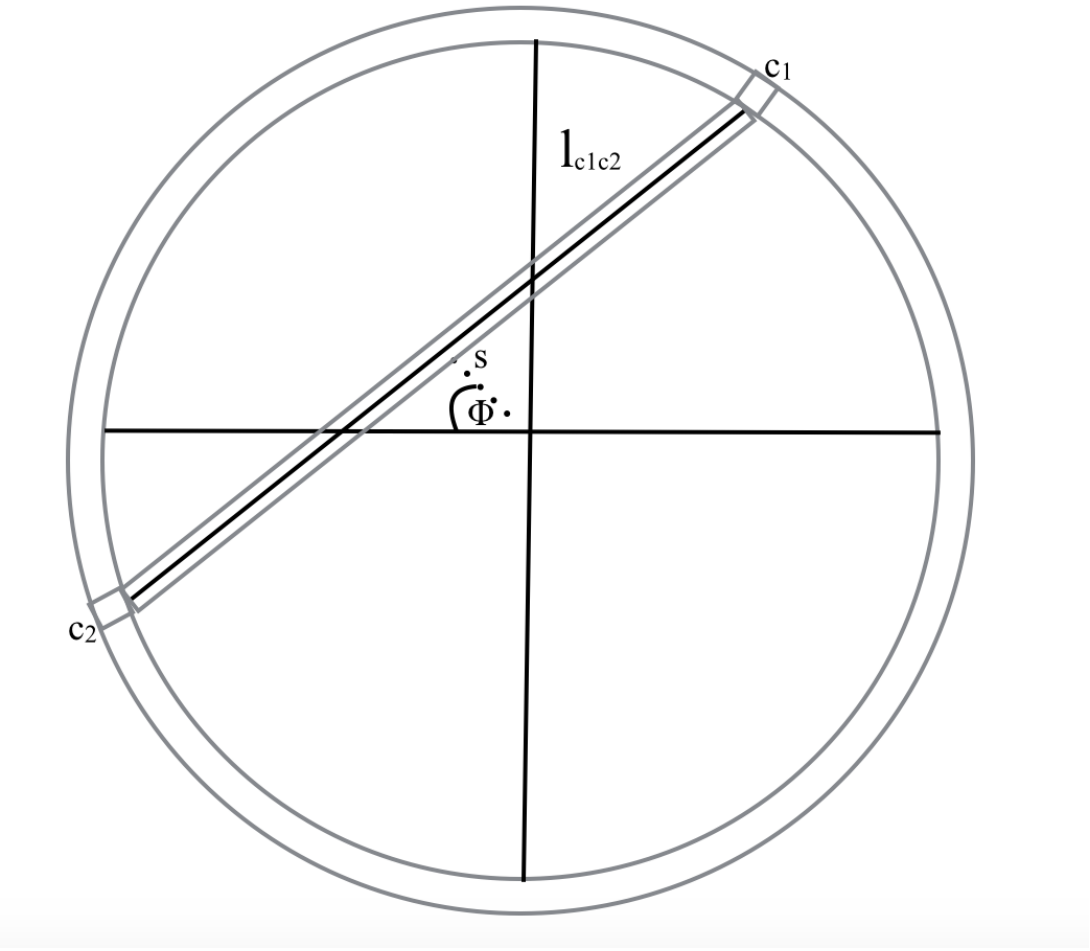

Figure 2.1: This figure demonstrate a LOR joining the centers of two detector crystals c_1 and c_2. All annihilation events occurring within the parellelepiped volume or 'tube of response' joining the surface areas of the crystals c_1 and c_2, that detected the annihilation, are stored by the scanner as LOR $\mathbf{l}_{c1c2}$. The scanner thus, stores an event as a LOR with spatial angle, 'ϕ' and perpendicular distance from the center, 's'.

These γ rays are detected by the detectors that are placed around the radioactive object. In an ideal scenario, where the γ rays are not scattered, they are recorded by a pair of detectors which have electronics to estimate the time difference between the arrival of the photons. This time difference must be within

the 'coincident time' of the scanner to be regarded as a coincident event. This forms the basic principle of PET detection, which is called as annihilation coincidence detection (ACD). The coincidence event must have occurred along a 'tube of response' that joins the two detectors that detected the photons (Fahey [2002], Defrise et al. [2005]). Each event that occurs within the volume or the 'tube of response' joining two detector surfaces are represented as 'LOR' as illustrated in Figure 2.1.

2.1.4 Photon Detection

As discussed in the previous section, PET is based on the principle of coincidence detection along the LOR. This section describes in detail, how the PET detectors classify the events as coincident.

The PET scanner is composed of multiple rings of detectors that are placed next to each other along the axial direction of the scanner. This leads to nearly 16,000 crystal-based detectors that cover the surface of the PET scanner (Jones and Townsend [2017]). These scintillation crystals are made up of inorganic material doped with an activator ion (Melcher [2000]). These materials absorb high energy photons, such as γ rays, and convert them into visible light. This is because the scintillator crystals have high density and high atomic number. These crystals have valence and conduction bands with an energy gap of 5 eV or more and are doped to create new energy levels within the band gaps. The photon that is absorbed by the crystal results in the emission of the scintillation photons as the excited activator ions lose their energy and come back to the valence band. The light that is emitted upon this relaxation is typically blue (Melcher [2000]). Bismuth germanium oxide (BGO), lutetium oxyorthosilicate (LSO) and

lutetium-yttrium oxyorthosilicate (LYSO) are a few of the crystals that are used as the detectors in currently used PET scanners. The traditional PET scanners used thallium-doped sodium iodide (NaI[Tl]) as the detectors which are then connected to a photomultiplier tube (PMT). Current PET scanners are comprised of blocks of detectors where each block is coupled to a PMT by a coupling material that has a refractive index similar to the scintillator material. The PMT detects the light in visible and ultraviolet (UV) ranges and generate electrons. In current PET scanners, the position of incident visible light is localised along the surface of the PMT which gives the information of scintillation crystal which detected the γ ray (Melcher [2000], Vandenberghe et al. [2016], Vandenberghe and Marsden [2015]).

Along with the position of the detection, γ ray energy and time of arrival of the ray onto the scintillator is measured and stored. In traditional PET scanners, that used scintillators such as BGO, the event is considered to be a 'coincident event' if two simultaneous photons are detected within the coincident time window of 2 ns (Moses [2001]). The PET detectors have internal clocks which register the time of arrival of one of the γ rays as it hits the scintillator. This opens the coincident time window for all other detectors, and if the other γ ray is registered by another detector within this time window, it is accepted and stored as a coincident event.

A typical PET scanner has its transaxial FOV of nearly 60 cm. The γ rays travel at the speed of light i.e. 3×10^8 m/s. According to the simple mechanics equation, $speed = distance/time$, the coincident time window is calculated to be 2 ns for a typical PET scanner.

The γ rays being detected within this time window are considered to be

simultaneous, and it is deduced that the 'coincident event' must have occurred along the LOR that joins the two detectors that detected them. Scintillation crystals with faster decay time, such as LYSO, improve the timing resolution significantly and can allow for 'TOF' imaging.

2.1.5 PET Data Acquisition

PET quantitatively measures the metabolic activity of the irregular tissue within the body with the help of a specific radiotracer. As discussed in the previous section 2.1.3, the detection mechanism of PET works on coincident detection and PET detectors measure and store information including the time of arrival, energy and the positions of the detectors for the incident γ ray.

The PET scanner stores the detected events in one of the two formats as described below:

- Listmode (LM) Format: LM data format is a stream of sequential events detected by PET crystals. In order to localise the position of an event within the FOV of the scanner, crystal transaxial and axial ID's are stored with it. The energy and time information is also stored for each event.

- Histogram Format: Histogram is the most common data format that is stored by PET scanners (Fahey [2002]). For histogram format, the scanner allots a large memory space for an array where each array element corresponds to a possible detector pair (or LOR). Traditional scanners had metal barriers called 'septa' between the rings to block inter-ring detections. Since current scanners do not have septa within the rings, this array is composed of all possible LOR for a cylindrical 3-dimensional (3-D) PET

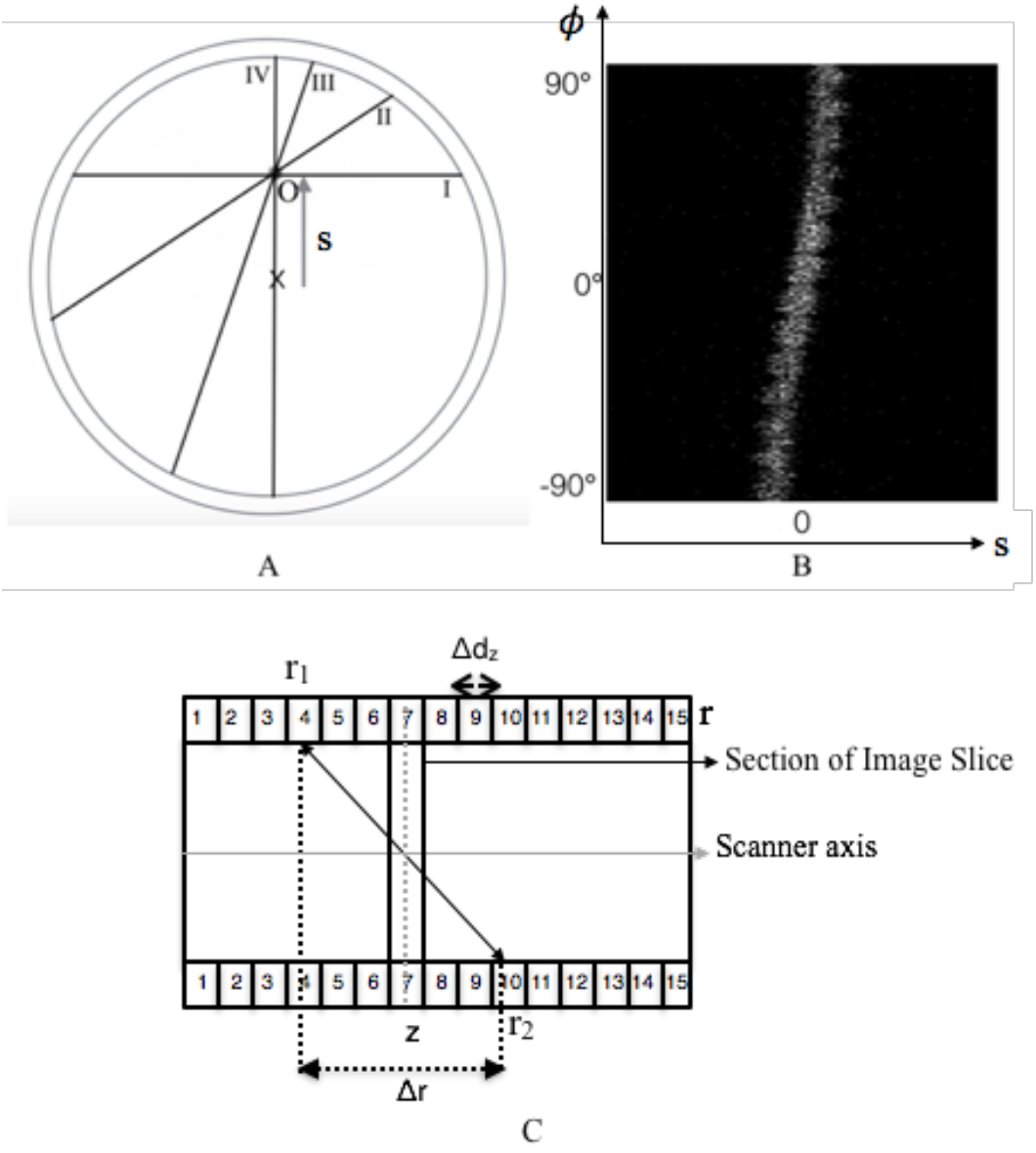

Figure 2.2: This figure demonstrate the PET acquisition process. (A) The image represents a radioactive source placed at position O within the FOV of the scanner. The gamma rays are emitted by the radioactive material and detected by the detectors at the end of the LOR's I, II, III and IV. The LOR's I, II, III and IV makes an angle of 0°, 33.3°, 71.7° and 90° with the centre of the gantry and is displaced from the centre. (B) The sinogram formed by plotting the displacement of the LOR from the centre on the x-axis and the angle on the y-axis is also depicted. (C) The cross-section of scanner geometry along scanner axis (or z-axis). The oblique LOR for an event detected by detectors having a ring difference $\Delta r = r_2 - r_1$ with axial position z is demonstrated. The width of each ring of the scanner which is represented as Δd_z is also demonstrated.

scanner. This allows coincidence detection in not only direct rings, which implies that the detection occurs within one ring, but also oblique rings, where the detection takes place in different rings. The scanner stores the following information for each detection:

1. Shortest distance of the LOR from the centre of the scanner, represented as 's' as can be seen in Figure 2.2 (B),
2. The azimuthal angle of the LOR represented as 'ϕ' as can be seen in Figure 2.2 (B),
3. The ring difference between the detectors that detected the events represented as 'Δr' as can be seen in Figure 2.2 (C) and
4. The axial position represented as 'z' as can be seen in Figure 2.2 (C).

Each histogram is a 4D array of 'bins'. Each bin is completely defined by the segment number, axial position, tangential position and view number where (Lima [2016]):

1. Tangential position is calculated as: $tangential = \frac{s}{binsize}$, where the $binsize$ of the scanner is calculated as the projection of the detector crystal along the x-axis of the scanner. Thus, tangential positions for a scanner are a set of discrete numbers that depend on the total number of bins.
2. View number is calculated as: $view = \frac{\phi}{sampling}$, where $sampling$ refers to the azimuthal angle sampling. The azimuthal angle sampling is equal to the ratio of the total number of detectors within the scanner and '2π'. Thus, view numbers are a set of discrete numbers that

varies from 0 to half the total number of detectors per ring. It should be noted that the azimuthal angle runs from 0° to 180° due to the symmetry in the detection of the γ rays along the opposite direction.

3. Segment number is calculated using 'Δr'. Segment numbers are a set of discrete numbers that represents all the possible ring differences allowed for the scanner. All the bins with common ring differences are merged together as one.

4. Axial number is calculated as: $axial = \frac{r_1+r_2}{2} * \Delta d_z$, where r_1 corresponds to the ring number for first detected γ ray, r_2 corresponds to the ring number for the second detected γ ray of the coincident event and Δd_z corresponds to the width of the ring for the scanner as can be seen in Figure 2.2 (C) (Lima [2016]).

When an event is detected along a LOR or the 'bin', the count in the element corresponding to that bin is incremented by 1. The number of events that are detected along a particular LOR can be obtained by reading the array element. The 2D arrays for a particular segment and axial positions resemble a 'sinogram' as demonstrated in Figure 2.2 (A), and so will be referred to as a sinogram hereafter. The sinogram, which is a 2D array of view and tangential positions. Thus, a histogram format is essentially a 4D array of 3D segment varying arrays where each array is further composed of axial position varying sinograms as demonstrated in Figure 2.3.

When 3D arrays of LOR's with the same view number, also referred to 'projection angle', are grouped together, it is called a 'projection'. A 4D array of 3D view varying projections (or 2D viewgrams for each segment)

form the complete 'projection data' (Fahey [2002]).

Michelogram

In order to describe sinogram mashing (or angular compression) and the Michelogram, a cylindrical PET scanner, having 15 rings and 8 detector modules as demonstrated in Figure 2.4, will be used. As discussed above, the histogram

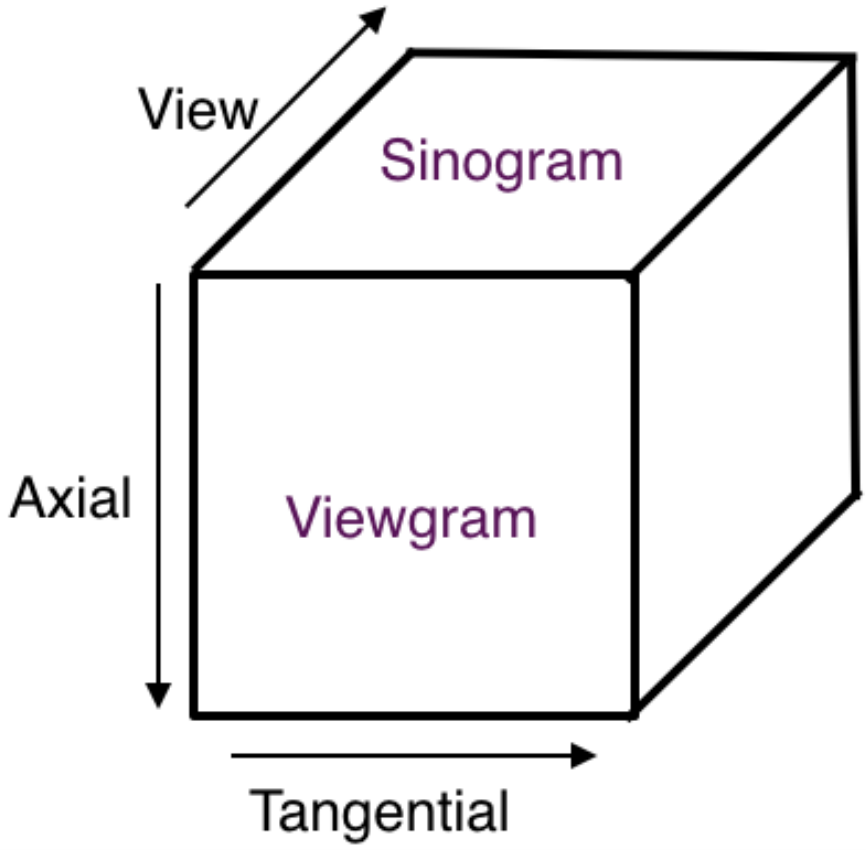

Figure 2.3: This figure demonstrates the 2-D sinogram with varying axial positions and viewgram with varying view numbers.

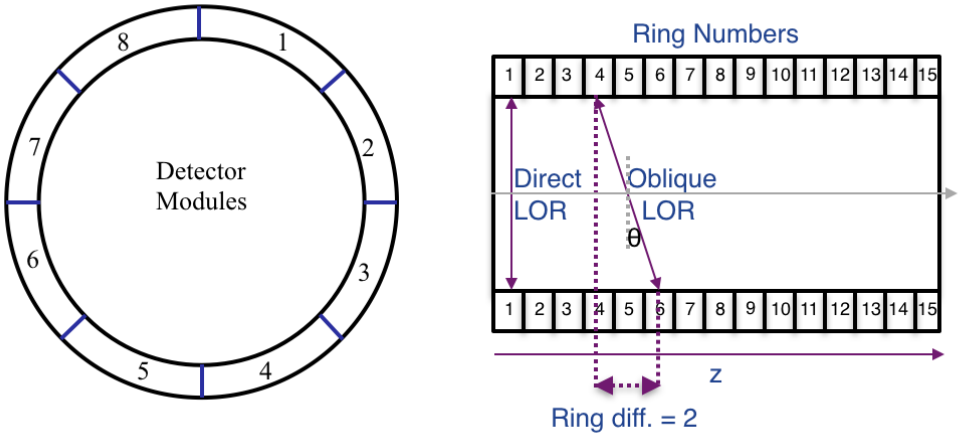

Figure 2.4: This figure demonstrates a PET scanner along transaxial and axial cross-section for a 15 ring scanner with each ring composed of 8 detector modules. The figure shows the direct LOR which implies that the event has occurred within a single ring. It also shows oblique LOR where the event occurred between ring number 4 and 6. This oblique LOR occurs in the segment that makes angle θ (co-polar angle) as demonstrated in the figure.

format arranges the acquired data in such a way that LOR's having similar physical properties are combined. When 3D arrays of multiple ring differences are merged to form a single array, the acquired data is said to have 'axial compression' or 'span' (Fahey [2002]). The Michelogram is a diagram that presents the axial compression present in the acquired projection data. An example of a Michelogram for the 16 ring scanner, that saves acquired data with span 1, is demonstrated in Figure 2.5. Span 1 has no axial compression, and thus, it does not combine the direct and oblique LOR's. For a 15 ring scanner with span 1, as demonstrated in Figure 2.5, ring differences vary from -14 to +14, where negative ring differences correspond to negative segment numbers, and positive ring differences correspond to the positive segment numbers. The ring difference

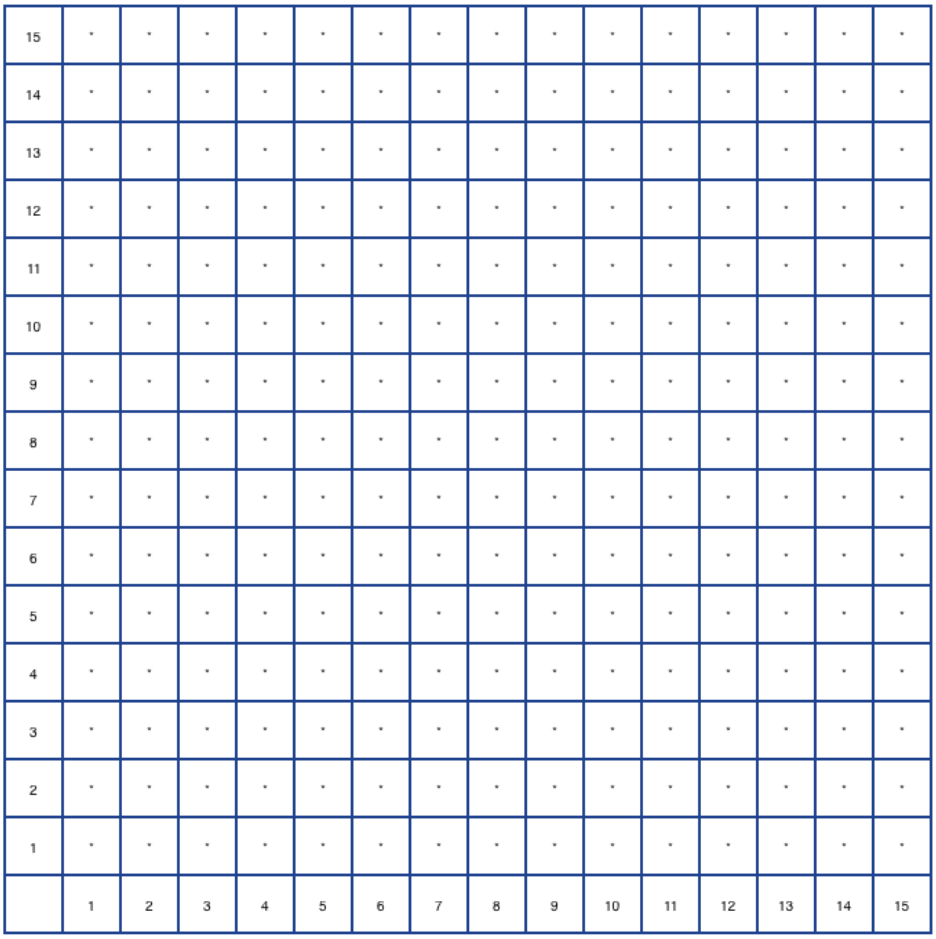

Figure 2.5: This figure represents a Michelogram for a 15 ring PET scanner and with span 1 where no ring differences are mashed.

0 corresponds to segment 0, and there are 15 direct axial positions (or transaxial planes) in this segment. Similarly, ring difference 1 corresponds to segment number 1, and there are 14 oblique planes within this segment, and so on. When there is a span in the data, there are ring differences that are combined to form a single segment. Figure 2.6 illustrates a Michelogram for a 15 ring scanner that stores the data with span 7, where ring differences 3 and 4 are mashed together

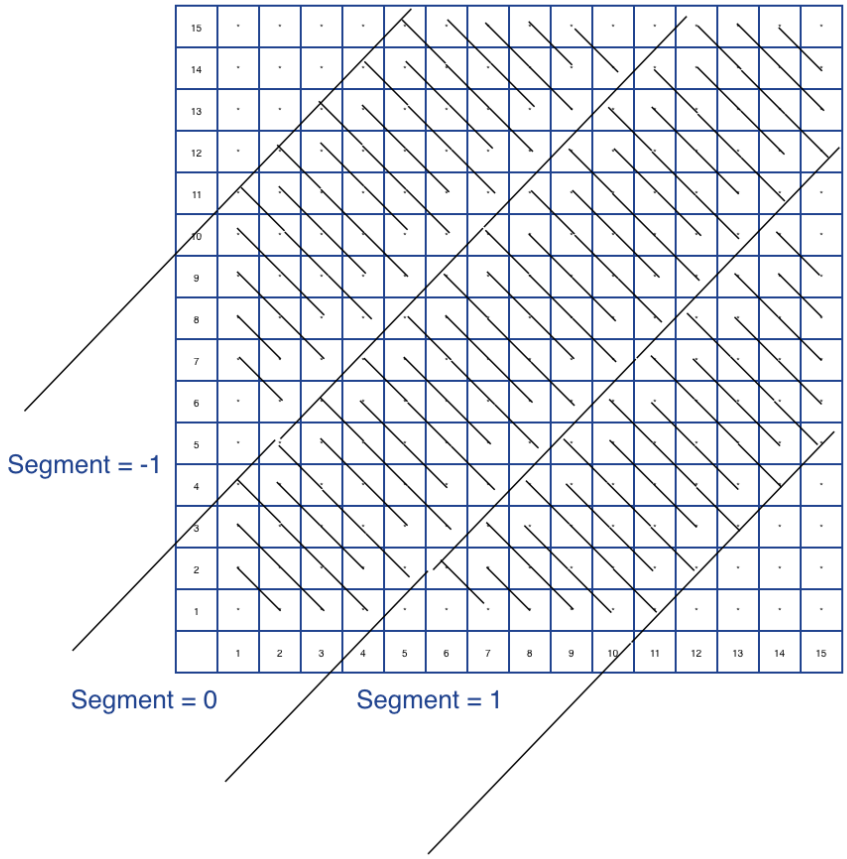

Figure 2.6: This figure represents a Michelogram for a 15 ring PET scanner with span 7 where ring differences=3+4 are mashed together.

in one segment.

LM versus Histogram Data Format

The LM data format preserves the spatial information of the events as they are stored along with the detector position information and the time of arrival information. Whereas, the sinogram data format groups together the events with common spatial characteristics which leads to the loss of spatial information in sinogram data format.

The LM data format can also be beneficial when the number of detected events is less than the number of LOR's as it can help to reduce the computer memory used. It is also possible to convert the LM data into sinogram format whereas, it is not possible to create LM data from sinograms, as the time and energy information is lost.

2.1.6 Acquisition Model

The radioactive distribution of an object filled with a radioactive tracer and placed within the PET scanner can be mathematically modelled as follows:

$$y = Ax + b, \tag{2.1}$$

where $y = [y_p]$ is a vector that represents the measured data acquired by scanning the object, $A = [a_{pm}]$ is a matrix that represents the system matrix, $x = [x_m]$ is a vector that represents the image parameters and b is a vector that represents the background coincidences (including randoms and scatter). The system matrix A models the probability of a positron annihilation occurring in voxel m being detected as a photon-pair coincidence by the detector pair p. It basically represents the sensitivity measure at each voxel m of the scanner. The sensitivity of each voxel m combines the detector efficiency, geometric and attenuation effects.

Image Representation

The unknown radioactivity distribution of the 3D object that is being imaged can be defined as a continuous function, $f(\mathbf{r})$ over spatial locations $\mathbf{r}$. Since the measured data obtained from the scanner comprises of limited data quantities,

the continuous function, $f(\mathbf{r})$ needs to be discretized in order to be computed. This is done by using a set of $m = 1, ..., M$ spatial basis functions, $\beta_m(\mathbf{r})$ to approximate $f(\mathbf{r})$ as (Reader and Zaidi [2007]):

$$f(\mathbf{r}) = \sum_{m=1}^{M} x_m \beta_m(\mathbf{r}), \tag{2.2}$$

where $\beta_m(\mathbf{r})$ represents the voxels that cover the FOV of estimated image and x_m represents the M-dimensional vector with each vector element represents the estimated image parameter or the voxel value (Reader and Zaidi [2007]).

Thus, the estimated image parameters, x_m represents the calculated value of radiotracer concentration (in units such as MBq/ml) within each voxel, m. The 3D image, $\hat{x}$ is calculated by appropriately using the image parameters as the elements of the matrix (Reader and Zaidi [2007]).

Data Representation

The measured PET data or the projection data in the measurement space is an array of sinograms or viewgrams and it is used to estimate the image (Reader and Zaidi [2007]). Projection data, y, is a P-dimensional vector with each vector element representing a bin, where each bin has a value representing the total number of coincidences detected by the detector pair $p = 1, 2, ..., P$ (Reader and Zaidi [2007]).

2.1.7 Counting Statistics

During a PET scan, a radiotracer is administered in the patient body to visualize the metabolic activity of the target tissue or organ. The detectors placed around

the body of the patient detect the emissions within a region and the emissions are proportional to the concentration of the radiotracer uptake (Lima [2016]). Due to the low quantity of administered dose in PET, the measurements or events detected with PET are generally limited (Rzeszotarski [1999]). Since the measured events are discrete and random, and the probability of detection per unit time is typically very small, the measurement process can be modelled using Poisson statistics (Rzeszotarski [1999]).

2.1.8 Image Reconstruction: Formulating the Problem

In a real scenario, the number of events detected by a standard whole-body PET scan with nearly 16,000 crystals are nearly a few hundred million. This is an estimated number for events detected in a typical 20 minutes scan for a 70 kg object with the administered activity of nearly 200 MBq. The measured projection data, y in equation 2.1, is a matrix of a few hundred million elements, called LOR. Each element or LOR stores annihilation event based on the detection parameters such as detection position, time and energy. If it is assumed that the object to be reconstructed has dimensions of $256 \times 256 \times 89$ voxel elements and that the object is scanned, as discussed above, for a 20 minute duration, then matrix x will have over 100 million parameters that must be estimated using equation 2.1. As can be seen, equation 2.1 is a linear equation and it can be re-written as:

$$y - b = Ax, \tag{2.3}$$

where y and b are in projection data space and have the same matrix size.

The image x can be calculated as:

$$x = A^{-1}(y - b). \tag{2.4}$$

Further, if the transpose of matrix A which is represented as A^T is applied to the above equation 2.3, it results in (Reader and Zaidi [2007]):

$$A^T(y - b) = A^T Ax. \tag{2.5}$$

Thus, if the measured data, y, is corrected for the background events, b, then the image, x, that represents the activity distribution of the object can be calculated as:

$$x = (A^T A)^{-1} A^T (y - b) \tag{2.6}$$

In the above equations, matrices A and $A^T A$ are huge and non-sparse (typically containing elements greater than 10^{14}) matrices which do not allow easy computation for pseudo-inverse (Reader and Zaidi [2007]).

Further, the above inverse problem as described in equation (2.4) is ill-conditioned. The condition number for matrix (condition number is calculated by taking the ratio of the largest to smallest singular value) demonstrates how sensitive is the solution to the changes or fluctuations (in the problem presented in this chapter these changes correspond to statistical noise) of the measured data. The condition number calculated for a very small matrix A of size 8×8 is around 250,000 (Llacer and Meng [1985]) and the condition number of the matrix of size 13×13 has been impossible to calculate with 48-bit mantissa. This shows the ill-conditioned nature of the matrix A. Ill conditioned nature of the

above inverse problem implies that even small errors (noise) in measured data will contribute towards large errors in the estimated image. Thus, the solution of x is basically a meaningless and bad approximation to the underlying image if it exists at all and does not give an accurate model of the actual underlying physical processes (Kabanikhin [2008], Tarokh [2017]). Whereas, the iterative reconstruction method such as Maximum likelihood expectation maximisation (MLEM) allows complete flexibility in the modelling of PET physical processes (such as attenuation and normalisation) within the matrix, A. Further, iterative methods estimate the underlying image by maximising the objective function which includes the assumption on the statistical distribution of the noise. Another benefit of iterative methods is that the matrix A is not stored within the memory but rather the respective matrix element having row, p and column, m is calculated on-the-fly which reduces the computational burden unlike the calculation of inverse of the matrix A which requires to be stored within the computer memory (Reader and Zaidi [2007]).

2.1.9 Image Reconstruction

Analytical Reconstruction

In analytical reconstruction methods, the continuous 3D radioactive object, $f(\mathbf{r})$, is not discretized into voxels. Whereas, the practical implementation of this method involves the calculation of discrete approximation of the continuous solution (Reader and Zaidi [2007]). The reconstruction problem here is to estimate $f(\mathbf{r})$ using a set of 2D parallel projections. It is assumed in the analytical reconstruction methods that 2D parallel projections (which are further a set of 1D LORs), $R(\mathbf{t}, \hat{\mathbf{c}})$ is equal to the line integrals through $f(\mathbf{r})$ as (Reader and Zaidi

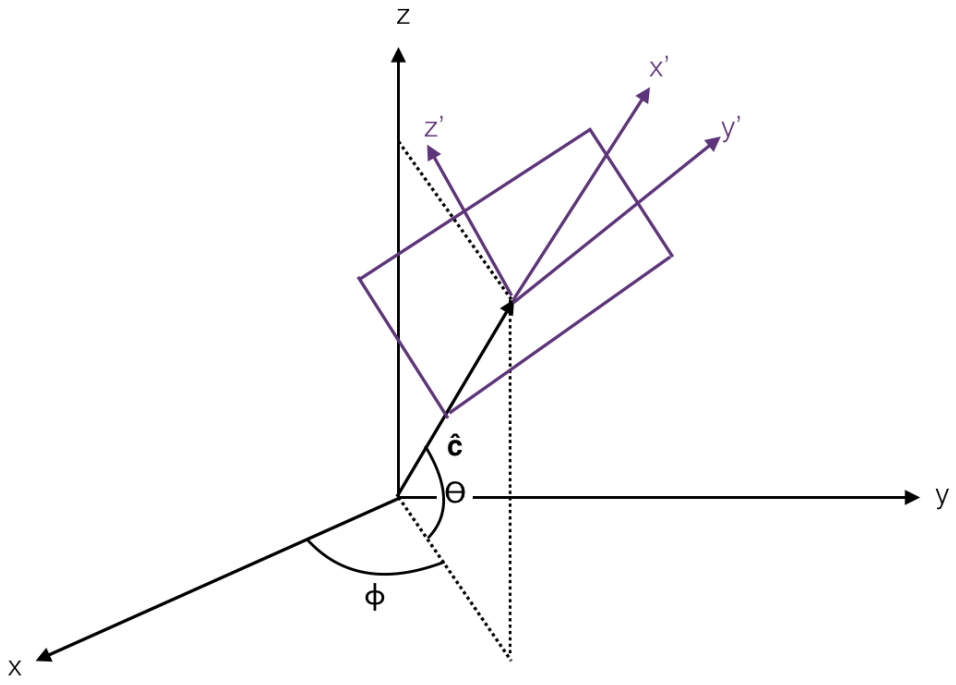

Figure 2.7: A representation of 2D parallel projection located at position vector $\mathbf{t}$ and oriented along unit vector $\hat{\mathbf{c}} = (\theta.\phi)$. This plane contains projections along all 1D LORs that are characterized by orthogonal distance s and along unit vector $\hat{\mathbf{c}}$.

[2007]):

$$R(\mathbf{t}, \hat{c}) = \int_{-\infty}^{\infty} f(\mathbf{t} + x'\hat{\mathbf{c}})dx' \tag{2.7}$$

where $\mathbf{r} = [xyz]^T$ is decomposed into two vectors $\mathbf{t}$ and $x'\hat{\mathbf{c}}$. Basically, the 2D parallel projection of the underlying radiotracer distribution, $f(\mathbf{r})$, is a $y' - z'$ plane located using position vector, $\mathbf{t} = [y'z']^T$ and oriented along the unit vector $\hat{\mathbf{c}} = (\theta, \phi)$, where θ is the co-polar angle and ϕ is the azimuthal angle as can be seen in Figure 2.7 (Reader and Zaidi [2007]).

Fourier Slice Theorem states that the Fourier Transform of the 2D parallel

projection, $T(\nu_t, \nu_{\hat{c}}) = \mathcal{F}[R(\mathbf{t}, \hat{\mathbf{c}})]$, is equal to the central plane of the FT of 3D radioactivity distribution, $F(\nu_x, \nu_y, \nu_z) = \mathcal{F}[f(\mathbf{r})]$ for the same orientation, $\hat{\mathbf{c}} = (\theta, \phi)$. This implies if FT for all 2D parallel projections (where θ and ϕ varies between 0° and 180°) are calculated, then all the planes of $F(\nu_x, \nu_y, \nu_z)$ can be filled up subsequently. Thus, the 3D radioactivity distribution, $f(\mathbf{r})$ can be easily calculated by taking the 3D inverse FT of $F(\nu_x, \nu_y, \nu_z)$, $f(\mathbf{r}) = \mathcal{F}^{-1}[F(\nu_x, \nu_y, \nu_z)]$ (Reader and Zaidi [2007]).

In the case of 2D PET reconstruction, the Fourier Slice Theorem states that the FT of 1D projection $L(s, \phi)$ (for each projection angle ϕ varying from 0 to 180°), $P(\nu, \phi) = \mathcal{F}[L(s, \phi)]$, is equal to the central section of FT of 2D radioactive distribution $f(x, y)$, $F(\nu_x, \nu_y) = \mathcal{F}[f(x, y)]$ at the same ϕ. In this case, the 2D radioactive distribution $f(x, y)$ can be calculated by taking the 2D inverse FT, $f(x, y) = \mathcal{F}^{-1}[F(\nu_x, \nu_y)]$ (Reader and Zaidi [2007]). This is Fourier transform or direct method.

Generally, the projections are 'smeared-back' along the same angle and position as detected. This is called back-projection. When projections along all orientations, $\hat{c}$ are smeared back, the superposition causes blurring which is removed by applying 'ramp filter' to the projections. The filtered projections obtained by using 'ramp filter' are backprojected within the FOV to estimate the underlying radiotracer distribution and this method is called Filtered Back Projection (Reader and Zaidi [2007]).

The above discussed analytical image reconstruction methods are generally considered inadequate as they do not model the statistical noise of the measured data. Thus, the analytical algorithms are not available within current clinical scanners such as GE SIGNA PET/MR and not used in this study. Thus, iterative

methods are generally used in the clinical environment.

Iterative Image Reconstruction

The main iterative reconstruction algorithms that are used in the clinical environment are discussed below:

MLEM

MLEM is an iterative algorithm that calculates the parameters which maximise the likelihood of a modelled random process for the observed data.

The measured PET data, y_p is best modelled using the Poisson distribution as discussed in section 2.1.7. The equation presented below demonstrates the measured data mathematically as:

$$y_p \sim Poisson(\sum_{m \in M} a_{pm} x_m + background), \tag{2.8}$$

where *background* refer to scatter and random events.

The expectation, $\overline{y_p}$ of the measured data, y_p is defined as:

$$\overline{y_p} = \mathbb{E}[y_p] = \sum_{m \in M} x_m a_{pm}. \tag{2.9}$$

where $\overline{y_p}$ represents the model of the mean of the measured data. The elements of $\overline{y_p}$ are basically the average number of counts that would have been measured in each tube that joins the detector pair p if the same experiment was repeated an infinite number of times. Thus, the mean data, $\overline{y_p}$ is never observed but is basically obtained from equation 2.9 (Reader and Zaidi [2007]).

An estimator $\hat{x}$ is calculated which maximises the log-likelihood or the 'objective function', $l(y \mid x)$ as below:

- The likelihood, $L(y \mid x)$ is defined as the product of the probability mass function of independent random variables, y_p as follows:

$$L(y \mid x) = \prod_{p \in P} P(y \mid \overline{y}) = \prod_{p \in P} e^{-\overline{y_p}} \frac{\overline{y_p}^{y_p}}{y_p!}, \tag{2.10}$$

  where $P(y \mid \overline{y})$ represents the probability of obtaining measured data y_p with expectation, $\overline{y_p}$ (Reader and Zaidi [2007]).

- The log-likelihood is thus:

$$l(y \mid x) = lnL(y \mid x) = \sum_{p \in P} y_p \ln \overline{y_p} - \overline{y_p} - \ln y_p!. \tag{2.11}$$

  After substituting $\overline{y_p}$ from equation 2.9 in equation 2.11, the log-likelihood can be written as:

$$l(y \mid x) = \sum_{p \in P} \sum_{m \in M} y_p \ln(x_m a_{pm}) - \sum_{p \in P} \sum_{m \in M} x_m a_{pm} - \sum_{p \in P} \ln y_p! \tag{2.12}$$

  Below is the double derivative of $l(y \mid x)$:

$$\frac{\partial^2 l(y \mid x)}{\partial x_k \partial x_l} = -\sum_{p \in P} \frac{y_p a_{pk} a_{pl}}{(\sum_{m \in M} a_{pm} x_m)^2}, \tag{2.13}$$

  where x_k and x_l represents the voxel values for voxel k and l respectively, a_{pk} and a_{pl} represents the probability that an event detected by detector

pair p is emitted within voxel k and l respectively. In the above equation, y_p, a_{pk} and a_{pl} are values greater than zero.

The log-likelihood is a concave function, as the calculated double derivative of the $l(y \mid x)$ (described in equation 2.13) with respect to image parameter, x_k and x_l is negative.

The measured data, y_p is considered as incomplete observed data as it denotes the value of measured counts within tube joining detector pairs, p and the exact location of emission is unknown. Whereas, $G = [G_{pm}]$ represents the matrix of complete unobserved data which consist of counts detected along the tube joining the detector pairs, p and emitted in voxel, m (Dempster et al. [1977]).

The complete unobserved data, G_{pm} is related to the measured data, y_p as:

$$y_p = \sum_m G_{pm}. \tag{2.14}$$

The expectation, $q = [q_{pm}]$ of the complete data G_{pm} is defined as:

$$q_{pm} = \mathbb{E}[G_{pm}] = x_m a_{pm}. \tag{2.15}$$

where q_{pm} represent the elements of matrix q and q represents the model of the mean of the complete unobserved data. The mean data q is never observed but is basically obtained from equation 2.15 (Reader and Zaidi [2007]).

The complete unobserved data, G_{pm} relates the measured data, y_p with the reconstructed image as in equation 2.15. The expectation maximiza-

tion algorithm basically computes the conditional expectation of the log-likelihood of the complete unobserved data, G_{pm}, using the given measured data, y_p and the current image estimate, x^j and then maximizes it (Leahy and Qi [2000]).

This expectation maximization algorithm can be formulated as:

$$\hat{x}^{j+1} = \underset{x}{\operatorname{argmax}}\, \mathbb{E}[l(G \mid x) \mid y, \hat{x}^j], \tag{2.16}$$

where $\hat{x}^{j+1}$ represents the estimated image update at iteration $j+1$ and $\hat{x}^j$ represents the estimated image at the current iteration j.

- The conditional expectation for $l(G \mid x)$ w.r.t y and $\hat{x}^j$, denoted as $\mathbb{E}[l(G \mid x) \mid y, \hat{x}^j]$, is calculated as (Lange and Carson [1984]:

$$\mathbb{E}[l(G \mid x) \mid y, \hat{x}^j] = \mathbb{E}\Big[\sum_{p \in P}\sum_{m \in M} G_{pm} \ln(x_m a_{pm}) - x_m a_{pm} - \ln G_{pm}! \mid y, \hat{x}^j\Big], \tag{2.17}$$

where $l(G \mid x)$ is substituted according to the equation 2.12.

Since, expectation follows linearity, the above equation can be re-written as:

$$\mathbb{E}[l(G \mid x) \mid y, \hat{x}^j] = \sum_{p \in P}\sum_{m \in M} \Big(\mathbb{E}[G_{pm} \mid y, \hat{x}^j] \ln(x_m a_{pm}) - x_m a_{pm}\Big) + O, \tag{2.18}$$

where $\mathbb{E}[G_{pm} \mid y, \hat{x}^j]$ represents the conditional expectation of independent Poisson random variables, G_{pm} w.r.t y and the current image estimate $\hat{x}^j$ and O are factors that are independent of x_m and are omitted, while maximising the expectation with respect to x_m as they are zero.

Since, G_{pm} is modelled as Poisson statistics (follows from equation 2.8 and equation 2.14), the conditional probability distribution of G_{pm} is a Binomial distribution. The expectation of this Binomial distribution is product of its parameters with parameters $(\sum_{m\in M} G_{pm}, \frac{\mathbb{E}[G_{pm}]}{\sum_{m\in M}\mathbb{E}[G_{pm}]})$. Thus, equation 2.18 can be re-written using equation 2.14 as (Lange and Carson [1984], Vardi et al. [1985], Blume [2008]):

$$\mathbb{E}[l(G \mid x) \mid y, \hat{x}^j] = \sum_{p\in P}\sum_{m\in M}\left(y_p \frac{\hat{x}_m^j a_{pm}}{\sum_{k\in M}\hat{x}_k a_{pk}} \ln(x_m a_{pm}) - x_m a_{pm}\right) + O, \tag{2.19}$$

- Finally, the expectation of objective function is maximised as the objective function is concave. This is done by setting the derivative of expectation of the objective function to zero as shown below:

$$\frac{\partial \mathbb{E}(l(G \mid x) \mid y, \hat{x}^j)}{\partial x_m} = \sum_{p\in P}\mathbb{E}[G_{pm} \mid y, \hat{x}^j] x_m^{-1} - \sum_{p\in P} a_{pm} = 0. \tag{2.20}$$

The equation 2.20 follows from equation 2.18. By substituting the value of $\mathbb{E}(l(G \mid x) \mid y, \hat{x}^j)$ in equation 2.20, the new estimate of the image parameter, x_m can be obtained as (Vardi et al. [1985]):

$$x_m = \frac{\hat{x}_m^j}{\sum_{p\in P} a_{pm}} \sum_{p\in P} a_{pm} \frac{y_p}{\sum_{k\in M} a_{pk}\hat{x}_k^j}, \tag{2.21}$$

Thus the MLEM takes the form of:

$$\hat{x}_m^{j+1} = \frac{\hat{x}_m^j}{\sum_{p\in P} a_{pm}} \sum_{p\in P} a_{pm} \frac{y_p}{\sum_{k\in M} a_{pk}\hat{x}_k^j}, \tag{2.22}$$

where $\hat{x}_m^{j+1}$ represents the updated image estimate with iteration $j+1$ from the image estimate of previous iteration, $\hat{x}_m^j$ The above equation is represented for a very simple case where the acquired data do not have any scatter or randoms. This is never the case and in a real life scenario, the acquisition model is as presented in equation 2.1. This implies the equation 2.22 is modified as follows:

$$\hat{x}_m^{j+1} = \frac{\hat{x}_m^j}{\sum_{p\in P} a_{pm}} \sum_{p\in P} a_{pm} \frac{y_p}{\sum_{k\in M} a_{pk}\hat{x}_k^j + b_p}, \tag{2.23}$$

where b_p represents the background histogram which is calculated by adding randoms correction and scatter correction sinograms.

In case the acquired data is in LM format instead of histogram format, LM events can be directly reconstructed using the LM-MLEM algorithm as mentioned and discussed in (Barrett et al. [1997], Snyder and Politte [1983], Reader et al. [1998a,b], Parra and Barrett [1998], Levkovilz et al. [2001]).

The LM-MLEM update equation is defined as:

$$\hat{x}_m^{j+1} = \frac{\hat{x}_m^j}{\sum_{p\in L} a_{pm}} \sum_{p\in L} a_{pm} \frac{1}{\sum_{k\in M} a_{pk}\hat{x}_k^j + b_p}, \tag{2.24}$$

where L represents the list of events.

OSEM Algorithm

MLEM algorithm is computationally demanding as it has slow convergence(Shepp and Vardi [1982], Parra and Barrett [1996]). The OSEM algorithm is an accelerated version of MLEM and uses subsets of the acquired data to compute image estimates (Hudson and Larkin [1994]). Due to its faster convergence, OSEM algorithm is a clinically preferred reconstruction algorithm. The OSEM algorithm

is defined as:

$$\hat{x}_m^{j+1} = \frac{\hat{x}_m^j}{\sum_{s \in S_z} a_{sm}} \sum_{s \in S_z} a_{sm} \frac{y_s}{\sum_{k \in M} a_{sk} \hat{x}_k^j + b_s} \tag{2.25}$$

where $\hat{x}_m^j$ represents the intensity of m_{th} voxel of the estimated image updated over the sub-iteration j, y_s represents measured event detected by the detector pair s of the subset S_z, a_{sm} represents the probability of an event occurring in voxel m being detected by the detector pair s of the subset S_z, b_s represents the background term to account for the sum of randoms and scatter events for the detector pair s of subset S_z. In the above equation, S_z represents the subset of detector pairs and $z = 1, 2, 3, ..., Z$ represents the number of subsets with Z being the total number of subsets. In MLEM, with every iterative update, the iteration value incremented by 1. Since OSEM is accelerated version of MLEM, it processes data as subsets (blocks) within one full iteration. So each iteration corresponds to a full cycle of sub-iterations across all subsets (i.e. iterations = sub-iterations/subsets). The subsets for OSEM algorithms are generally selected as a divisor of the blocks of detector within a ring of the scanner (Hudson and Larkin [1994]). This is because Hudson and Larkin have demonstrated that in order to reconstruct PET data with OSEM algorithm, the LOR's must be rebinned in the subsets with a particular order. This ensures that activity in every voxel is equally contributed by events in all the subsets (Hudson and Larkin [1994]).

Stopping Rule

MLEM algorithm iteratively computes the expectation of the objective function and maximises it to converge towards the maximum likelihood estimate. How-

ever, the iterative updates get noisier and develop 'noise' artefact (peaks and valleys) as the image updates climb the likelihood hill towards the maximum likelihood estimate (Snyder et al. [1987]). As shown by Snyder et. al. (1985), there is an increase in image noise over iterations, which is due to the unconstrained maximum likelihood estimation of the density function (Snyder and Miller [1985]). Due to the fundamental nature of the problem, a stopping rule is important as the noisy images can be avoided at lesser iterations. Various stopping rules have been investigated, which allows stopping the reconstruction just before the iteration, where the image deterioration (image deterioration refer to the sharp changes in the intensity near the edges of the imaged object) begins (Veklerov et al. [1988], Veklerov and Llacer [1987], Gaitanis et al. [2010], Bissantz et al. [2006]). The image deterioration depends on the measured number of counts and tend to occur at a later iteration if the measured number of counts are higher, whereas, it occurs at an earlier iteration if the measured number of counts are lower. Veklerov and Llacer (1987) suggested to calculate a parameter, H, which is a part of Pearson's χ^2 test after each image update and to stop the reconstruction where the parameter H is minimized (Veklerov and Llacer [1987]). Bizzante et. al. (2016) proposed a stopping rule which uses the scaled partial sums of the normalised difference between measured data and forward projection of the image at every iteration and a critical model parameter (which is the median of the test statistics) to deduce the optimal image update (Bissantz et al. [2006]). Although these stopping rules are available, they have not yet proven to have practical value in the clinic (Hamill and Bruckbauer [2002], Gaitanis et al. [2010], Barrett et al. [1994], Kontaxakis and Tzanakos [1992]). The 'noise' artefact is also prevalent in OSEM algorithm due to its fundamental

nature. In clinic, the iterative process is generally stopped after 2 or 3 iterations and then a Gaussian filter is applied to suppress the 'noise' artefacts (Meikle et al. [1994], Liow and Strother [1991], Asma et al. [2012], Ahn et al. [2015]).

2.1.10 Data Corrections

Each coincidence event can be associated to a LOR that joins the detector pairs where the event was detected. A LOR is associated with multiple coincidence events detected by the respective detector pairs. The coincidence events are also called 'prompts' (Bolus et al. [2009]). The prompts not only comprise 'true' coincidences but also 'random' and 'scatter' coincidences which degrade the data and thereby reconstructed images. A 'true' coincidence refers to the event which actually took place along the LOR (Bolus et al. [2009]).

Scattered and Random Coincidences

The photon travelling from the place of annihilation towards the detectors does not always have a smooth journey. It can get scattered with the object leading to scattered and random coincidences. When one or both of the γ rays gets scattered due to body tissue along its way to the detector, it is said to be 'scattered' coincidence and the LOR is misplaced from the actual annihilation location (Bolus et al. [2009]). This coincidence contributes to the image background, thereby leading to the loss of contrast and hence poor quantification of the image. When two scattered events from unrelated coincidence are detected within a coincidence window, this again leads to false and misplaced coincidence and is called 'random' coincidence.

These coincidences need to be accounted for as they contribute to image

degradation and artefacts, and in clinical situations, they are corrected during image reconstruction. These coincidences contribute to the image background and are represented as b in equation 2.1.

In a typical clinical situation, the randoms and scatter correction histograms are calculated using the methods described below. The histograms are further included within the iterative reconstruction process as the background term. These corrects for the embedded noise effects within the measured data during the reconstruction and artefacts due to scatter and random events are not present within the final PET images.

Scatter Correction

The photons in PET are generally scattered due to Compton scattering (Zaidi and Montandon [2007]). Every non-scattered photon is expected to have 511 keV energy. Photons that suffer Compton scattering experiences a loss of energy with the scattered energy, E_s, and a change in incoming direction with a scattering angle, θ. The scattered energy is described as:

$$E_s = \frac{E}{1 + \frac{E}{m_0 c^2}(1 - cos\theta)}, \tag{2.26}$$

where E is the energy of the incoming photon and m_0 is the rest mass of the photon. All the photons that are deflected by large angles have the scattering energy that falls outside of the 'coincidence energy window' (where coincidence energy window corresponds to the scanner specific energy window to detect coincidence events) and thus, are not relevant for scatter correction. The photons that have a small scattering angle, less than 35°, are the ones that need to be

scatter corrected. This is because they will retain more energy and will be detected within the coincidence energy window (i.e. usually above 430keV). For GE SIGNA PET/MR scanner, the coincidence energy window is set between 425-650 keV.

The scatter correction can be modelled and estimated using various methods such as multiple energy window, convolution and de-convolution based approaches and statistical-reconstruction based scatter correction. The most commonly used method is single scatter simulation (SSS) (Watson et al. [1996]). The SSS method is implemented in open-source software, STIR, and uses the emission data along with the attenuation image to reconstruct the attenuation corrected image (Tsoumpas et al. [2004]). It uses the attenuation image to estimate scatter points and calculate the scattering probability for each point based on the Klein-Nishina equation (Klein and Nishina [1929]). The scattering probabilities are then added for each scatter points and interpolated to create the entire scatter correction histogram. The estimated scatter correction histogram is finally scaled with the factors calculated using the tail-fitting method (Thielemans et al. [2007], Polycarpou et al. [2011]). Double scatter simulation is also implemented in STIR but it is not used as it is computationally slow (Tsoumpas et al. [2005]).

Randoms Correction

Two non-related scattered photons which are detected as a coincidence event by the PET scan are called 'accidental' or 'random' coincidences. They contribute to image degradation and must be corrected for, to estimate accurate image quantification. In clinical PET, random coincidences are estimated and corrected

for during the reconstruction. The randoms can be estimated for each detector pair using the following methods (Oliver and Rafecas [2016]):

- Randoms from singles (RFS) estimation: The random events (represented as R_{ij}) along a LOR joining detectors i and j are estimated using the rates of single events recorded by detectors i and j within a coincidence window of the scanner. The randoms estimation is described by (Stearns et al. [2003], Stearns and Lonn [2011]):

$$R_{ij} = 2\tau S_i S_j, \tag{2.27}$$

  where S_i, S_j is the detected singles rate by detector i and j respectively and τ is the coincidence time window.

  This method is almost noiseless as there are much greater number of detected single events per unit time, but it may have bias (Stearns et al. [2003]). This bias may arise due to the inaccuracies in singles rate measurement.

  GE SIGNA PET/MR uses this method to estimate the random events (Stearns and Lonn [2011]). Within the PET detectors of this scanner, there are single counters which accumulate the registered single events. The accumulated single events are passed on to the digital coincidence processor. The digital coincidence processor records each event at a timestamp with the timing resolution of τ_{LSB}. Assuming that a coincident event is registered when the difference between the recorded time is W, then the effective coincidence window, t_{eff} will be $(2W + 1)\tau_{LSB}$ (Stearns et al. [2003]). For the entire acquisition with acquisition time, T_{acq}, the calculated randoms

events are (Stearns et al. [2003], Stearns and Lonn [2011]):

$$R_{ij} = \frac{(2W+1)\tau_{LSB} S_i S_j}{T_{acq}} = \frac{t_{eff} S_i S_j}{T_{acq}}. \tag{2.28}$$

The calculated single events are prone to activity decay of the source and the intrinsic activity of the detector (Stearns and Lonn [2011]). The scanner has Lutetium-based scintillator crystals which have intrinsic activity even when zero activity is present within the field of view (Stearns and Lonn [2011]). This factor is included within the modelling of single events and is accounted for within the randoms correction by the scanner. It has also been reported by Stearns and Lonn (2011), that the random events are affected by the detector dead-time (dead-time is defined as the time of paralysis of each crystal when it does not detect any event as it is processing the previously detected event). The scanner also accounts for dead-time correction within the randoms correction calculations (Stearns and Lonn [2011]).

Decay and dead-time effects are explained in detail (Stearns and Lonn [2011]):

1. Decay Correction: The radioactive source decays over time during the acquisition. This isotope decay is not taken into account in equation 2.28. Whereas, GE SIGNA PET/MR scanner corrects for decay within the randoms correction model (Stearns and Lonn [2011]). The decay correction are increasingly important for longer scan duration with more than one half-life of the imaged radio-isotope (Stearns and Lonn [2011]). The decay factor is small and the value is between

$1.00 - 1.01$ when the acquisition time is less than on-half life of the injected radio-isotope.

2. Dead-time Correction: An experiment conducted by Stearns and Lonn (2011) using a phantom filled with ^{82}Rb (75 sec half-life) and GE scanner demonstrated that detector dead-time effects can be seen within the acquired data even early on within the scan. GE SIGNA PET/MR scanner accounts for the dead-time effects within the randoms correction model (Stearns and Lonn [2011]). Dead-time effects are small for clinical situations and increase with the injected dose substantially.

3. Intrinsic Activity of Scintillators: GE SIGNA PET/MR scanner uses LYSO crystals as scintillators. Lutetium-based crystals have intrinsic activity and have observed to produce randoms coincidence events even when there is no activity present within the scanner. GE SIGNA PET/MR scanner accounts for the intrinsic activity as a background term within the randoms correction model (Stearns and Lonn [2011]).

The RFS model is adapted by GE SIGNA PET/MR scanners to account for decay, dead-time and intrinsic activity as follows (Stearns and Lonn [2011]):

$$s_x(t) = s_x^0 e^{-\lambda t} + b_x, \tag{2.29}$$

where $s_x(t)$ represents the calculated singles rate at time, t, s_x^0 represents the singles rate at $t = 0$, b_x represents the intrinsic activity of the LYSO crystals ($b_x = 0$ for non-lutetium scintillator) and λ represents the decay constant of the radioisotope. The dead-time effect is also taken into account

within the model as (Stearns and Lonn [2011]):

$$\sigma_x(t) = s_x(t)e^{-\tau_D s_x(t)}, \tag{2.30}$$

where $\sigma_x(t)$ represents the effective singles rate output from detector, x, at time, t, τ_D is the paralyzing dead-time of the detector.

Finally, the RFS estimation (equation 2.28) which accounts for decay, dead-time and intrinsic activity correction is defined as (Stearns and Lonn [2011]):

$$R_{ij} = \frac{t_{eff}\sigma_i(t)\sigma_j(t)}{T_{acq}}, \tag{2.31}$$

where $\sigma_i(t)$ is the effective singles rate from detector i at time t, $\sigma_j(t)$ is the effective singles rate for detector j at time t.

- Randoms estimation using the delayed window: In this method, the coincident events detected are duplicated by applying a delayed time such that the events do not fall within the coincidence window (Oliver and Rafecas [2016]). A random event is detected when the delayed γ ray is detected as coincident with a non-delayed γ ray. This method relies on the fact that the correlation between delayed and non-delayed (or original) streams is broken. This method is more accurate than randoms from singles estimation, but the delayed window method needs to be stored in a different channel than the prompt events, which further needs an increase in storage to double. Also, the randoms have higher levels of statistical noise as this method uses coincidences to estimate the randoms. The Siemens mMR scanner estimates the random events using this method (Delso et al. [2011a]).

Normalisation Correction

The PET detectors have different detection efficiency, which leads to systematic and random errors (Theodorakis et al. [2013]). These errors lead to artefacts in PET images which degrade the image quantification. These systematic and random errors are called normalisation errors.

Normalisation errors can be estimated as calibration factors for each LOR using a 'blank scan' (Defrise et al. [1991b]). A blank scan is a scan where a uniform source of known activity is placed within the gantry to irradiate the detectors with the equivalent activity over a constant period of time. The calibration factors for each detector, are calculated to normalise the differences between detector responses as a ratio of the number of coincidences detected during a blank scan and the mean number of coincidences averaged over all LORs. The limitations of the calculated efficiency is in the direct correlation with the statistical accuracy of the blank scan.

In current scanners, the normalisation correction is calculated using the technique proposed by Casey and Hofmann (Casey and Hoffman [1986]). The method proposed calculates the normalisation factors along each LOR and assumes that the sensitivity of each LOR can be expressed as the product of each detector efficiencies and radially-dependent geometric factor (Theodorakis et al. [2013], Defrise et al. [1991b]). These geometrical factors depend on the detector positions and are calculated for each scanner once, and the same array of geometric factors are used thereafter. The detector efficiency factors are calculated more often as they change over time. In current scanners, the detector efficiency is calculated daily during quality checks.

Attenuation Correction

The γ rays get attenuated as they pass through tissues within the body which leads to the reduction of the energy of the detected radiation. Attenuation is calculated as:

$$I = I_0 e^{-\sum_i \mu_i X_i} \tag{2.32}$$

where I is the intensity of the attenuated radiation with initial intensity I_0, μ_i corresponds to the linear attenuation coefficient of the tissue i and X_i corresponds to the thickness of the tissue i where the radiation passed through. Traditionally, CT has been used as a companion to PET due to its ability to provide electron density information of the object placed in the scanner which can be used to calculate the PET based attenuation coefficients. However, PET scanners which are combined with MR has a significant drawback as MR scanners are only capable of giving proton density information which cannot be used to calculate the attenuation correction (AC) factors.

This lack of attenuation information with MR could be resolved by using traditional PET attenuation calculation techniques (Vandenberghe and Marsden [2015]). A torus shaped source containing a tube filled with radioactive [^{68}Ge] or [^{137}Cs] is used to calculate attenuation. In this method, the source is scanned with and without the patient placed within the gantry, to estimate the electron density of the tissues of the patient (Bowen et al. [2016]), by calculating the intensity of detected radiation. This PET scan used to calculate the attenuation is termed as 'transmission scan'. Currently, this method is only validated using simulated studies for PET/MR scanners. The current clinical protocol uses MR images to calculate the attenuation correction histogram. Although, the MR images do

not give electron density information, they give soft tissue contrast and excellent anatomical details. These high-resolution anatomical images are segmented to provide the entire volume of each tissue which is further assigned with pre-calculated PET attenuation factors. Mean attenuation factors (for PET at 511 keV) for tissues are reported in the literature, for example, the attenuation factor for air= $0.0058cm^{-1}$, lung = 0.0349 cm^{-1}, fat = 0.0895 cm^{-1}, water = 0.0987 cm^{-1} and bone = 0.1178 cm^{-1} (Kim et al. [2012]). The resulting segmented tissue assigned with PET attenuation factors are combined together to get a attenuation map from MR images which is forward projected to calculate the attenuation correction histogram.

The above-mentioned data correction techniques are used to calculate the histograms which are used directly within image reconstruction algorithms to calculate the fully corrected PET images.

Well Counter Calibration

The reconstructed images are in units of detected counts which must be translated into units of injected activity for quantitative accuracy (Wilson et al. [1991]). The conversion of units is determined using a well counter which is a cylindrical scintillation crystal with a well within the crystal. PET radiotracer is placed within this well and detected by the scintillator (Lodge et al. [2015]). There is a photo-multiplier placed at the end of the scintillator and measurements are made in counts per minute (cpm). These units are converted to the units of activity/cpm using the table provided by the manufacturer for different possible isotopes (Lodge et al. [2015]). This factor is calculated at the time of the scanner installation.

2.1.11 TOF-PET

The basic principle behind TOF imaging is that the γ rays are detected by faster scintillating crystals with greatly improved timing resolution (Vandenberghe et al. [2016]). The current clinical scanners achieve a timing resolution of 220 ps for PET/CT (van Sluis et al. [2019]) and 390 *ps* for PET/MR scanner (Grant et al. [2016]). The improved timing resolution thereby improves the localisation of the event along the LOR. This is because of the simple mechanics equation (Vandenberghe et al. [2016]):

$$\Delta t = 2\frac{\Delta x}{c}, \tag{2.33}$$

where Δt represents the difference in arrival times of the coincident γ rays with improved timing precision, Δx represents the uncertainty in the localisation of the event along the LOR where the event has occurred, and c is the speed of γ rays. For example, with a timing resolution of 200 *ps*, the uncertainty in the position of the event along the LOR is calculated to be 30 *mm* (Moses [2003]). For an even better timing resolution of 20 *ps*, the uncertainty reduces to 3 *mm*. Thus, the TOF information is hugely helpful in improving the contrast recovery and signal to noise ratio, which further improves image reconstruction performance even with low count statistics (Conti [2011]).

These advantages and availability of cheaper computing power along with advanced iterative reconstruction methods have inspired manufacturers to assemble TOF-PET scanners with CT or MR modalities. GE SIGNA and Philips Ingenuity TF are two PET/MR scanners with improved timing resolution of 390 *ps* and 525 *ps* respectively (Vandenberghe et al. [2016]). Siemens Biograph

PET/CT has even faster timing resolution of 220 ps (van Sluis et al. [2019]).

TOF-OSEM

Unlike conventional PET scanners where the measured coincidence event is localised along the LOR joining the detector pairs, the TOF PET scanners localise the measured event within a number of voxels along the LOR which belong to the individual TOF bins, $t = 0, 1, ..., T$, where T corresponds to the total number of bins. Thus, the measured TOF data can be defined as a matrix y_{pt}, where each event is recorded along the LOR p and TOF bin t. The TOF bins are equally sampled along the coincidence window with the width, $\Delta = 2\tau/T$, where τ corresponds to the width of the coincidence window.

The system matrix of the acquisition model as described in equation 2.1 is modified as a_{ptm}. A TOF kernel matrix is multiplied to a_{pm} to form the system matrix, a_{ptm} for the measured TOF data, y_{pt}. Each element of TOF kernel matrix corresponds to the TOF spatial weighting coefficient which models the probability of detection of an event occuring in voxel, m to be detected by detector pair, p and in a certain TOF bin, t (Mehranian et al. [2016], Efthimiou et al. [2019]).

The statistical distribution of the measured noisy TOF PET data, y_{pt} can be mathematically modelled as:

$$y_{pt} \sim Poisson(\sum_{m \in M} a_{ptm} x_m + r_{pt} + s_{pt}), \tag{2.34}$$

where r_{pt} and s_{pt} represents the random and scatter events respectively, detected within the detector pair p and TOF bin t (Mehranian et al. [2016]).

The log-likelihood to be maximised for estimating the image parameters, x_m

for acquired TOF PET data, y_{pt} is:

$$l(y \mid x) = \sum_{p \in P} \sum_{m \in M} y_{pt} ln(\overline{y_{pt}}) - \overline{y_{pt}} - lny_{pt}!, \tag{2.35}$$

where $\overline{y_{pt}}$ represents the expectation of y_{pt} (Mehranian et al. [2016]).

Thus, the expectation maximisation algorithm is used to maximise the log-likelihood and estimate image $\hat{x}$ from TOF PET data as:

$$\hat{x}_m^{j+1} = \frac{\hat{x}_m^j}{\sum_{p \in P} a_{ptm}} \sum_{p \in P} a_{ptm} \frac{y_{pt}}{\sum_{k \in M} a_{ptk} \hat{x}_k^j + b_{pt}}, \tag{2.36}$$

where x_m^j represents the estimated intensity of the m^{th} voxel updated over the sub-iteration j and b_{pt} represent the matrix of the background events to account for randoms r_{pt} and scatter s_{pt} events detected in detector pair p and TOF bin t.

The TOF-OSEM algorithm (Mehranian et al. [2016]) was implemented within STIR by Efthimiou et. al. (2019). This algorithm has been validated within STIR using simulated data (Efthimiou et al. [2019]) and is validated further in this thesis for clinical datasets with the state of the art TOF PET/MR scanner. The algorithm is described as (Wadhwa et al. [2020]):

$$\hat{x}_m^{j+1} = \frac{\hat{x}_m^j}{\sum_{s \in S_z} a_{stm}} \sum_{s \in S_z} a_{stm} \frac{y_{st}}{\sum_{k \in M} a_{stk} \hat{x}_k^j + b_{st}}, \tag{2.37}$$

where y_{st} is a matrix representing the TOF projection data for a detector pair s within the subset S_z and timing bin t, a_{stm} is a matrix representing the probability of an event occurring in voxel m being detected by a detector pair s within the subset S_z and the timing bin number t, b_{st} is a matrix representing the back-

ground term to account for the sum of randoms and scatter events for a detector pair s within the subset S_z and timing bin t. S_z represents the subset of the detector pairs s and z is the number of subset.

2.2 Magnetic Resonance Imaging (MRI)

2.2.1 Introduction to MRI

MRI is an imaging modality particularly employed in clinical diagnosis as it provides detailed anatomical and functional images. It images protons in the hydrogen nuclei of water and lipid molecules found within the human body (Westbrook and Kaut [1998]). In the presence of an externally applied magnetic field, the protons of hydrogen nuclei interact with the applied field and precess with a frequency that is proportional to the applied magnetic field. The net magnetic field produced as a result of this interaction is called the Net Magnetisation Vector (NMV) (Westbrook and Kaut [1998]).

An oscillating magnetic pulse having the precessional frequency of protons is applied to the patient and is absorbed by the protons causing the NMV to move out of alignment from the direction of the static magnetic field (called longitudinal plane) and flips towards the transverse plane. The applied Radio Frequency (RF) pulse also makes the protons to move in phase (Westbrook and Kaut [1998]).

When the RF pulse is switched off, the NMV induces voltage fluctuations within the receiver coil which is read out as MR signal (Westbrook and Kaut [1998]). The protons lose their absorbed energy and the loss of absorbed energy leads to (Westbrook and Kaut [1998]):

- An increase in the amount of magnetisation along the longitudinal direction. This is termed as T1 recovery.
- A decrease in the amount of the magnetisation along the transverse direction due to the de-phasing (protons interact and begin to precess out-of-phase with one another) of the individual protons. This is termed as T2 decay (Westbrook and Kaut [1998]).

2.2.2 MR Sequences

There are various MR sequences that are used in MRI. A common technique used in PET/MR imaging is the Dixon technique, as it gives segmented map of fat and water, which is used for PET attenuation correction as further described in section 2.3.

Dixon Sequence

Images obtained from the Dixon sequence are fat and water images which exploit the difference in the resonant frequencies of the hydrogen nuclei found in fat and water respectively. The hydrogen nuclei of fat are linked with carbon, whereas, the hydrogen nuclei of water are linked to oxygen. In water, the oxygen attracts the shared electrons more strongly than hydrogen, which implies that the hydrogen in the water molecule is more susceptible to the external magnetic field. Whereas, in fat, the shared electrons remain in the hydrogen atom cloud and thus, the hydrogen atom is protected. This leads to a difference in precessional frequency of the hydrogen nuclei in fat and water. This difference in the resonance frequency is termed as "chemical shift" (Coombs et al. [1997]). At 3T, there is a chemical shift of 450 Hz.

Since fat and water have a chemical shift, the NMV of fat and water precess at different frequencies and move in and out of phase with each other. At 3T, fat and water protons fall out of phase (called opposite phase) at 1.1 msec and they fall in phase (in-phase) at 2.2 msec after the RF pulse excitation. This causes the signal produced in the receiver coils to be a 'water minus fat' during opposite-phase and 'water plus fat' signal during in-phase. Images are processed to achieve water-only and fat-only images by carrying out voxel-by-voxel addition or subtraction according to:

$$Fat = \frac{(In\_phase – Opposite\_phase)}{2} \tag{2.38}$$

$$Water = \frac{(In\_phase + Opposite\_phase)}{2} \tag{2.39}$$

Dixon sequence, therefore, gives a segmented map of fat-only and water-only images. This technique divides the body into tissue classes: water and fat Coombs et al. [1997].

2.3 Multi-Modality PET

PET is a quantitative visualisation tool that images the function of abnormal tissue using target-specific radiotracers as described above (Lammertsma [2017], Bastiaannet et al. [2004]). The ability to image the functional activity gives PET an advantage over other morphology-based conventional imaging modalities, such as MR, Ultrasound (US) and CT, in diagnosing and patient management (Pennant et al. [2010], Schiepers et al. [1995]). PET images provide important infor-

mation for various clinical applications, but are prone to degraded image quality and quantification due to various reasons such as attenuation, Compton scattering, positron range and motion (Zaidi [2001], Jødal et al. [2012], Vandenberghe and Marsden [2015], Catana [2015]). Attenuation effects have been resolved by combining the PET modality with CT which provides the electron density map of the scanned object (Townsend et al. [2003]). In current clinical environments, PET/CT is largely used and there are only standalone PET scanners available for breast and brain (Czernin and Schelbert [2004], Ishikita et al. [2010]). Although, there is a major advantage of PET/CT combined modality which improves image quality and quantification and thus patient management, there is a major drawback as it provides nearly double the amount of radioactive dosage to the scanned patient (Akin and Torigian [2012]). The other drawback is that PET/CT is only a sequential imaging modality and does not allow simultaneous imaging.

Recently, combined PET/MR scanners have been introduced and the PET research community has developed a major interest in PET/MR scanners due to various benefits that are involved with MR scanners over CT (Judenhofer et al. [2008], Antoch and Bockisch [2009]). One of the advantages is that the MR scanner lacks ionising radiation which can allow the scanning of a sensitive group of patients, such as children and pregnant women, with PET/MR modality. Although, the main advantage of MR over CT, is that MR provides soft tissue contrast which can be beneficial in the brain, abdominal and musculoskeletal imaging (Antoch and Bockisch [2009], Ehman et al. [2017]). Another advantage of using MR imaging modality is that the positron range reduces in the presence of magnetic field and the positrons only move along the magnetic field, which improves the in-plane resolution in PET images (Kolb et al. [2015], Hammer

et al. [1994]). PET/MR imaging modality allows simultaneous functional and anatomical imaging which can help to reduce the motion effects as MR can provide high temporal imaging information to correct for motion (Kolbitsch et al. [2014]).

Despite the above-mentioned advantages, combining PET/MR modality into a single unit was challenging. The conventional PET modality has PMTs that are incompatible withMR due to their sensitivity towards the magnetic field (Judenhofer et al. [2008]). This has been resolved by using the solid-state detectors that are insensitive to magnetic field, such as Avalanche photodiode (APD)s, LYSO and LSO. Apart from this, a current challenge with PET/MR modality is the lack of a gold standard attenuation correction method with MR for PET attenuation affected data.

There have been various methods that have been investigated to extract Magnetic Resonance Attenuation Correction (MRAC) images from the MR images including atlas-based and direct imaging segmentation-based methods (Chen and An [2017]). The atlas-based method estimates PET attenuation values from a MR images. This is done using a large training data of CT anatomical images and deriving a computational relationship from this CT image to get the MR image. The computational algorithm that estimates the MR image from the CT image can further be used to estimate the pseudo-CT image for a given MR image when the CT is not available. Thus, an attenuation image can be estimated using the MR image. There are various ways which can be used to derive the computational relationship between MR and CT images including machine learning methods (Chen and An [2017]).

The other way to extract the AC image using the MR image, that has been

exploited, is the segmentation-based method. This method utilises direct MR anatomical sequences such as Dixon, ultrashort echo time (UTE) and zero echo time (ZTE) to extract the patient anatomy. These images are further segmented along the volume, and each region is assigned with the PET attenuation correction factors. Dixon images are acquired within a few seconds, and UTE or ZTE images are acquired within a few minutes, which is quite favourable to keep the attenuation correction protocol short (Chen and An [2017]).

Although segmentation-based and atlas-based are highly used MRAC methods, there are significant drawbacks associated with these methods. With the presence of anatomical abnormalities or unusual tissue density within the data, the atlas-based method will produce large AC errors. This is because these abnormalities are different from the training dataset and computational algorithms cannot accounted for them. The drawback associated with the segmentation-based method is because the sequences such as UTE and ZTE cannot differentiate between bone and air. This can lead to large AC errors when air cavities are wrongly assigned as bone (this can occur in situations where the bone is removed or not present). Apart from this, the MR extracted images are prone to noise and artefacts, which can undermine the accuracy of this method (Chen and An [2017]).

2.4 GE SIGNA PET/MR

Scanner Specifications

This PET/MR scanner is composed of a MR-compatible TOF-PET scanner fitted within the bore of a 3T MR scanner as can be seen in Figure 2.8 (Grant et al.

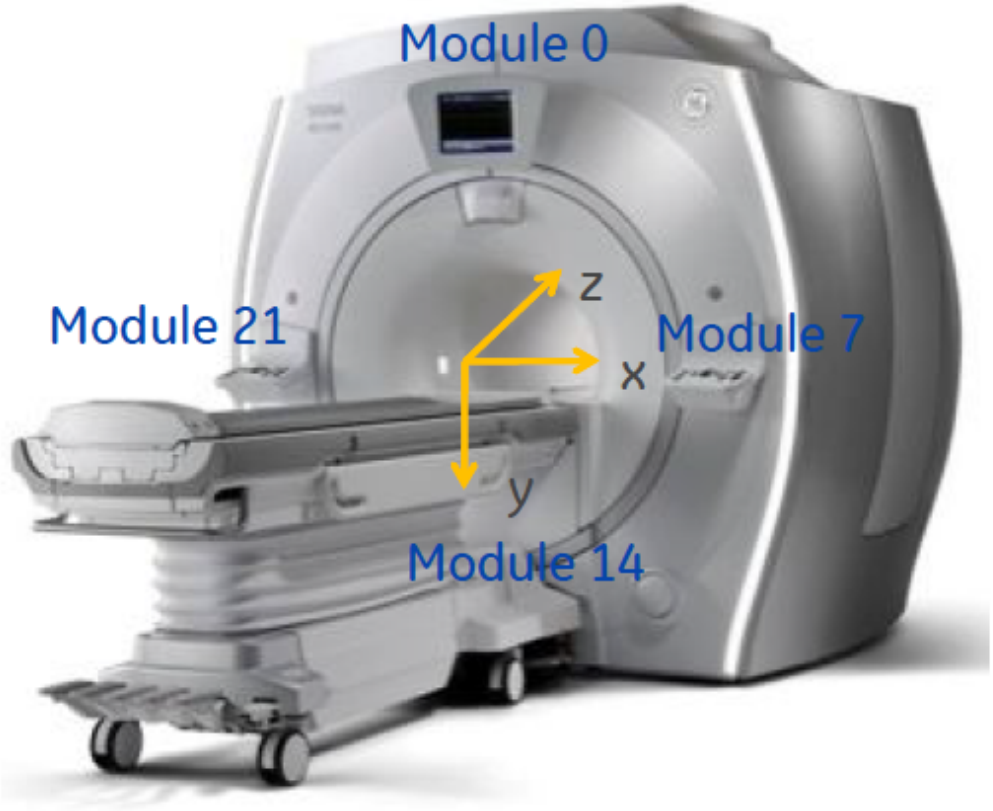

Figure 2.8: GE SIGNA PET/MR scanner is composed of 28 detector modules with module 0 located vertically above the iso-center of the MR scanner.

[2016]). The axial field of view of the PET component of this scanner is 25 cm. It comprises of Lutetium-Yttrium Oxyorthosilicate (LYSO) crystal-based detectors, Silicon PhotoMultipliers (SiPM) and other fast processing electronics (Vandenberghe et al. [2016], Hsu et al. [2017]). The SiPM is magnetically insensitive to electromagnetic fields which makes it possible to scan PET data while collecting MR data (Grant et al. [2016]).

PET Component Configuration

The PET component of the scanner is composed of 28 detector modules placed next to each other to form a cylindrical insert. The detector module 0 is centred vertically above the isocenter of the MR scanner and the crystal 0 is positioned at an offset of -5.23° from the vertical centre in the anticlockwise direction when viewed from the back of the scanner as can be seen in Figure 2.8. Each detector module has 5 detector units placed simultaneously along the z-axis with a crystal-free gap of size 2.8 mm. There are 4 blocks of crystals in each detector units composed of 4×9 crystals. The dimensions of each crystal is $5.3 \times 3.95 \times 25$ mm^3 along the axial, tangential and radial directions. There are 3×6 SiPMs for each 4×9 crystal configuration. The total number of detectors in this scanner is 20,160 (Wadhwa et al. [2020]).

2.5 Image Reconstruction Software

Every clinical scanner is available with software which can allow image reconstruction of the data and the images used for further clinical applications such as kinetic modelling, clinical diagnosis and therapy planning. GE scanners come along with in-built reconstruction software and an offline reconstruction software

called GE-Toolbox, which is used in this thesis.

2.5.1 GE-Toolbox

GE-Toolbox is an object-oriented MATLAB based software framework provided by the vendor that allows offline PET image reconstruction. It is comprised of various MATLAB, C and C++ (wrapped inside MATLAB-callable wrappers) functions and utilities. These functions and utilities are used to reconstruct and analyse PET data. The software framework is compatible with GE PET/CT as well as PET/MR scanners. The DICOM data acquired at the end of a scan are used as input for reconstruction for this software and reconstructions are conducted after setting the reconstruction parameters. The functions and utilities in the toolbox model the system matrix including scanner geometry, detector dead-time/pile up and attenuation effects. The model implementation in the toolbox also accounts for the physical effects, including the random and scatter events. The modelling has proprietary information and is a 'black box'.

Although all scanners have an accompanying reconstruction software, this software is not available at all sites. In research, data sharing (especially for phantoms) can be helpful in improving the research efficiency. Thus, a software platform that can readily provide a framework to reconstruct data is of high significance for the research community. Different research groups have contributed towards creating license-based software platforms that readily allows image reconstruction. Michigan Image Reconstruction Toolbox (MIRT) is a MATLAB-based software platform that provides various iterative and non-iterative image reconstruction algorithms (Fessler [2018]). A sparse iterative reconstruc-

tion library (ASPIRE) and Tomographic Image Reconstruction Interface of the Universite de Sherbrooke (TIRIUS) as well are software platforms available for emission tomographic reconstruction (Fessler [1995]). These libraries have regularised and unregularized reconstruction methods implemented for users (Fessler [1995]). Another available software library is PET Reconstruction Software toolkit (PRESTO), which focuses on a novel scanner-independent geometrical description of 3D PET data and optimising the reconstruction times (Scheins and Herzog [2008]). The open-source reconstruction software called STIR (http://stir.-sf.net) used in this thesis for PET image reconstruction is described in the next section.

2.5.2 STIR

STIR is an open-source reconstruction library comprising of various classes, functions and utilities to reconstruct Emission Tomography (ET) data (Thielemans et al. [2012]). It is designed to be modular and has an inheritance between classes which allows it to be extended to incorporate novel algorithms and scanner geometries conveniently without the need of re-implementing existing attributes and functions. The inheritance structure of the STIR library implies that there are base classes and descendent classes can inherit the attributes and behaviour of these base classes without needing to re-implement the code again. The basic building blocks of STIR are described below:

- Basic Data Storage Classes: All input and output data that is processed in STIR can be arranged as an array which is a basic data storage class implemented. The images that are stored are based on 3-dimensional arrays which can be built on the base class. STIR also has Cartesian grids

defined within a base class for images. Projection data and projection data information are read and stored within 'ProjData' and 'ProjDataInfo' base classes respectively, which are defined within STIR. Further, STIR also allows storing dynamic projection data and gated projection data. Apart from projection data, LM data can also be imported in STIR and base classes that are implemented for LM data include 'CListModeData' and 'CListRecord'. The LM base classes allow reading of each event and extract all the information from the acquisition to store these events such as detector pair information. The input and output base classes provide the building blocks to import projection or LM data and write the image data.

- Scanner Geometry Building Block: STIR has a base class where cylindrical scanner geometry is implemented. It currently does not support other geometry types with gaps whereas there is a major study conducted which can be used to support this (Thielemans et al. [2012], Khateri et al. [2019]). Most clinical PET scanners are cylindrical and STIR can define user-based scanners.

- Reconstruction Class Building Blocks: STIR has base classes implemented for analytical and iterative reconstructions which can further be inherited to develop novel reconstruction algorithms such as parallel level sets (PLS) (Tsai et al. [2017]) and hybrid kernelised expectation maximisation (HKEM) (Deidda et al. [2018b, 2019]) as described and used in subsequent chapters.

STIR provides a platform for the PET research community where the library is expandable to "fit the needs" of new users as the field progresses by deriving

new classes from basic building blocks (Thielemans et al. [2012], Wadhwa et al. [2020, 2018]). Currently, STIR is used to reconstruct PET emission data using analytical and iterative reconstruction algorithms (Thielemans et al. [2012]). Most commonly used reconstruction algorithms such as MLEM and OSEM are already implemented within the library (Beisel et al. [2008], Thielemans et al. [2012]). The structure of STIR allows for the incorporation of the newly introduced commercial scanners. An example of such implementation is demonstrated in the subsequent chapter. Although STIR is a modular programming tool which allows users to reconstruct data from the clinical scanners, it has its limitations. Some of these include a lack of flexibility in scanner geometry and conventions (Thielemans et al. [2012], Wadhwa et al. [2020, 2018]). Nevertheless, STIR is a continually evolving software and incorporates more reconstruction algorithms such as LM-OSEM, which makes it a robust open-source software to implement new scanners.

2.5.3 SIRF

As discussed above, there are clinically available PET/MR scanners which are provided by major clinical manufacturers. Although the hardware component of PET/MR modalities have been combined, there is no software that allows synergistic PET/MR reconstructions. This lack of software availability has been overcome by the introduction of SIRF (downloadable from: https://github.com/CCP-PETMR) (Ovtchinnikov et al. [2020], Brown et al. [2019]). This software combines already available PET and MR image reconstruction softwares, STIR and gadgetron in one reconstruction software and allows synergistic image reconstruction (Ovtchinnikov et al. [2020], Brown et al. [2019]).

2.6 Anatomically-Informed Image Reconstruction Algorithms

With open-source software such as STIR, there are greater possibilities of improving image reconstructions using novel iterative algorithms. With the introduction of clinical PET/MR modalities, the PET images can be improved using MR anatomical information. Novel iterative algorithms that utilises MR kernels to reconstruct PET images, called KEM, have already been implemented in STIR and are further expanded in this thesis.

2.6.1 KEM Algorithm

The KEM algorithm was first proposed by (Wang and Qi [2014]) and was developed in STIR library by Deidda et al. (2019). This algorithm is based on a machine learning technique and it aims to extract a kernel matrix using the MR feature vectors. The PET image is modelled as a sum of weighted kernels k_{fm} as described:

$$x_m = \sum_{f=1}^{N_m} \lambda_f k_{fm}, \tag{2.40}$$

where value at voxel m of image, x_m, is represented by the linear combination of the kernel matrix (k_{fm} represents its fm^{th} elements and f and m represent the elements of the feature vectors that form the kernel matrix), N_m represents the number of feature vectors and λ_f represents the kernel weights (Deidda et al. [2019]). Feature vectors represents the voxel intensities within a patch (or cubic array) extracted from MR image.

The acquisition model represented in equation 2.1 is modified using the equa-

tion 2.40 as:

$$y = AK\lambda + b, \tag{2.41}$$

where $K = [k_{fm}]$ represents the kernel matrix and $\lambda = [\lambda_f]$ represents a vector of kernel weights.

Thus, the image reconstruction algorithm here is used to estimate the kernel weights, λ. The standard expectation maximisation algorithm can be directly used to estimate the kernel weights.

The kernel weights are reconstructed as follows:

$$\lambda_f^{j+1} = \frac{\lambda_f^j}{\sum_{m \in M} k_{fm} \sum_{s \in S_j} a_{sm}} \sum_{m \in M} k_{fm} \sum_{s \in S_j} a_{sm} \frac{y_s}{\sum_{l \in M} a_{sl} \sum_{o \in N_m} k_{om} \lambda_o^j + b_s}. \tag{2.42}$$

The final image, $\hat{x}$ which contains the PET radioactive information is obtained by substituting the last iteration of equation 2.42 within equation 2.40 (Deidda et al. [2019]).

2.7 Summary

PET images have a low resolution which affects the quantification and detection of small regions. This study targets improved image quantification as well as contrast recovery and signal to noise ratio using novel iterative reconstruction algorithms. This is mainly possible due to improved PET technology, TOF-PET, which allows improved localisation of PET activity. Both TOF-PET imaging and KEM algorithm reduce noise which can be hugely beneficial in reducing the injected radioactivity.

This chapter introduced and discussed the background of PET physics, MR

imaging modality, data acquisition, data correction methodology and the GE SIGNA PET/MR scanner and its image reconstruction software. This chapter also discusses TOF imaging, open-source software, STIR and clinical and novel image reconstruction algorithms.

Chapter 3

Methods

This chapter focuses on the methodology of reading TOF-PET data from GE SIGNA PET/MR with the STIR library. It also discusses the troubleshooting and validation testing required to incorporate the scanner acquired raw data formats into STIR's native histogram format. The implementation of the modelling of PET acquisition data within the STIR library was necessary to create the foundation for this study. Further, the implemented novel iterative reconstruction algorithm TOF-KEM has been described in this chapter. It presents the method of reconstructing the TOF-PET data with clinically-used and novel iterative reconstruction algorithms, using the open-source software, STIR, for the first time. It also summarises the phantom and clinical data used for demonstration and validation purposes. Finally, it introduces the statistical methods used to carry out region of interest (ROI) based image analysis.

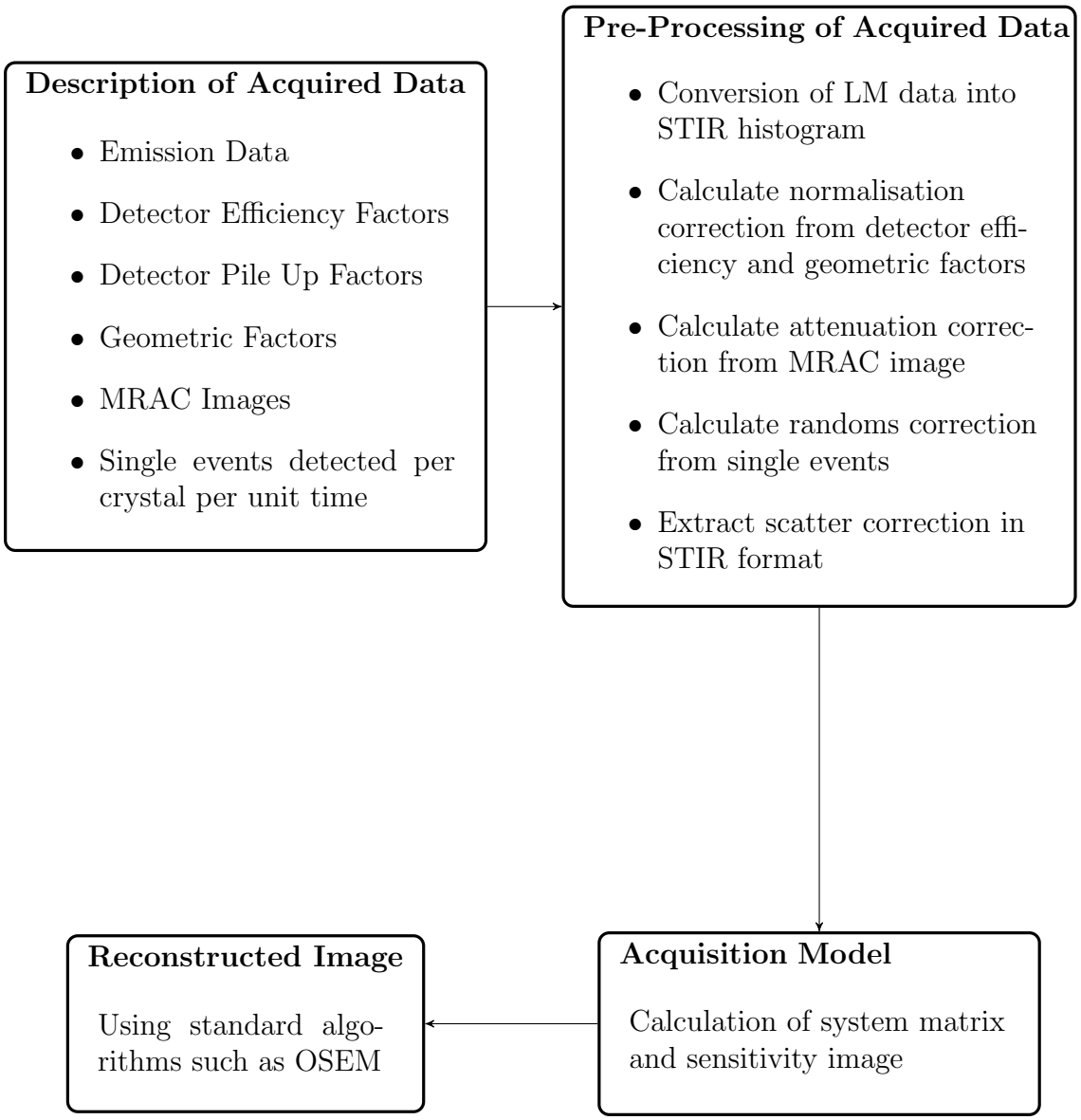

Figure 3.1: This figure shows the pipeline exhibiting the image reconstruction of raw data extracted from the scanner using STIR.

3.1 Description of Acquired Data

This section describes the acquired TOF-PET and MRAC (i.e. attenuation correction images extracted from MR scan using segmentation method) data that is extracted from the GE SIGNA PET/MR scanner at the end of a simultaneous PET/MR scan. It also describes the data format of the extracted raw data files for this scanner.

The output PET and MRAC files saved by the scanner console at the end of an acquisition include:

1. Compressed LM file: This file is saved with GE's proprietary compression algorithm and can be uncompressed by the scanner console after the scan.

2. Compressed histogram file: The scanner also saves a compressed emission data file which is saved as a Digital Imaging & COmmunication in Medicine (DICOM) file. The histogram array along with the header information is wrapped within the DICOM file and it stores all detected LOR's. The histogram array, along with the header information, is stored as a Hierarchical Data Format 5 (HDF5) file. The acquired histogram data is described in detail in the next section. The DICOM file can be uncompressed using the scanner console, and the GE-toolbox can be used to extract the HDF5 file that contains the histogram data.

3. Normalisation files: The scanner stores arrays of detector efficiency factors, geometric factors and well counter calibration as HDF5 files which are wrapped within DICOM files.

4. PET Image For Attenuation (PIFA) files: The MR images resulting from

Dixon and ZTE sequences are segmented and assigned with appropriate PET attenuation factors. The resulting images are called PIFA, which are stored by the scanner in its native PIFA file format.

5. PET reconstructed images: These are DICOM images that are reconstructed with particular reconstruction and image settings at the time of the scan.

The GE toolbox stores the acquired data in its proprietary file format, which is HDF5. The scanner saved normalisation and histogram DICOM files with '.RPDC' extension and MRAC images are stored in PIFA file format. The output LM compressed files are stored with an extension '.BLF'.

The HDF5 files are extracted from the above-mentioned output files using the GE-toolbox in order to use them as inputs for image reconstruction. The extracted HDF5 files are named as follows:

1. Histogram array is stored in a file called 'rdf.1.1'.

2. Detector efficiency and geometric correction factors array are stored in a file called 'norm3d'.

HDF5, PIFA and DICOM files are used as inputs to STIR and these files are further pre-processed to extract emission and data correction in file formats native to STIR software.

3.2 Pre-Processing of Acquired Data

As illustrated in Figure 3.1, the acquired data is pre-processed within STIR. This section describes the implementation that are made within STIR to pro-

cess the acquired emission data and data corrections to facilitate further image reconstruction.

3.2.1 Conversion of LM Data into STIR Histogram

The LM HDF5 file stores a stream of coincident events along with detection information, including arrival time differences and detector position for the pair of detectors. Each coincident event is stored as a 6 byte (or 48 bit) structure of fields describing the detection information. The 48 bits of the coincident event are organised as:

- The first 2 bits store the event type name, such as coincidence or single event.
- The next 1 bit stores the flag for coincidence.
- The next 6 bits store the axial crystal position for one coincident detector.
- The next 10 bits store the transaxial crystal position for one of the coincident detectors.
- The next 6 bits store the axial crystal position for the other coincident detector.
- The next 10 bits store the transaxial crystal position for the other coincident detector.
- The next 9 bits store the arrival time difference.
- The next 4 bits store a binary flag for detector recovery after an event is detected, i.e. the flag is 0 when the event is being processed by the detector

(within the detector's dead-time), and the flag is 1 when the detector is ready to detect the next event.

The required fields within this structure that are used in this study correspond to the axial and transaxial crystal (or detector) numbers of the crystal pairs that detected the events and the delta time (i.e. the difference between the arrival times of the two γ rays detected within a coincidence). This data is accessible by navigating to the field called '/ListData/ListData' (Bertolli et al. [2016], Wadhwa et al. [2018]) and can be accessed after skipping the first 3 bits.

The crystal identifiers (ID)'s and the TOF information are handled within STIR in 'CListModeData' base class. A derived class 'CListModeDataGESIGNA' was implemented to handle the transaxial and axial crystal coordinates for GE's extracted LM data as described above in STIR space. Pre-defined functions in STIR were used to convert the crystal pair coordinates into respective LOR's. The LOR coordinates are then converted into the bin of the histogram. Further, the arrival time differences are also handled here to calculate the TOF bin number.

3.2.2 Implementation of Normalisation Correction

The scanner stores the normalisation factors in the 'norm' HDF5 file (Wadhwa et al. [2018]). It stores crystal efficiency factors as an array of dimensions 448×45. This array is stored in the field called '/3DCrystalEfficiency/crystalEfficiency/'. It also stores 3-D geometric correction factors as a histogram but for only 16 views. This array is repeated to populate the entire histogram for this scanner having a dimension of $224 \times 1981 \times 357$. The projection data is stored in the field called '/SegmentData/Segment4/3D_Norm_Correction/slice#', where

slice# corresponds to view number 1 - 16.

To correct for the systematic variations between different detectors and geometric variations over the axial FOV, the detector efficiency correction and geometric correction factors are read for every LOR. The normalisation correction factors that counteracts the normalisation effects for each histogram bin (or LOR connecting two detectors) is calculated (Defrise et al. [1991a], Bailey et al. [1996]) as:

$$n_{XY} = \frac{g_{XY}}{\epsilon_X \epsilon_Y}, \tag{3.1}$$

where n_{XY} represents the normalisation correction factor for the detector pair comprised of detectors X and Y, ϵ_X and ϵ_Y represents the crystal efficiency factors and g_{XY} represents the geometric correction factors.

The efficiency factors for detector X and Y within the adjacent rings are combined together as:

$$\epsilon_{comb} = \epsilon_{Xf}\epsilon_{Yg} + \epsilon_{Xg}\epsilon_{Yf}, \tag{3.2}$$

where e_{comb} represents the efficiency of the combined LOR from adjacent crystal rows (as GE SIGNA PET/MR combines the adjacent ring as one single histogram bin and all LOR's detected between detectors of the two adjecent rings and direct ring are combined together), ϵ_{Xf} is the efficiency of the detector f placed on ring X, ϵ_{Yg} is the efficiency of the detector Y placed on ring g, ϵ_{Xg} is the efficiency of the detector X placed on ring g and ϵ_{Yf} is the efficiency of the detector Y placed on ring f.

The normalisation correction factors are inversely related to the efficiency

factors. Thus, equation 3.2 can be written as:

$$\epsilon_{comb} = \frac{1}{c_{Xf}c_{Yg}} + \frac{1}{c_{Xg}c_{Yf}} = \frac{c_{Xg}c_{Yf} + c_{Xf}c_{Yg}}{(c_{Xf}c_{Yg})(c_{Xg}c_{Yf})}, \tag{3.3}$$

where c_{Xf} is the correction factor for the efficiency of the detector X placed on ring f, c_{Yg} is the correction factor for the efficiency of the detector Y placed on ring g, c_{Xg} is the correction factor for the efficiency of the detector X placed on ring g and c_{Yf} is the correction factor for the efficiency of the detector Y placed on ring f.

Equation 3.3 can be re-written for c_{comb} as:

$$c_{comb} = \frac{(c_{Xf}c_{Yg})(c_{Xg}c_{Yf})}{c_{Xg}c_{Yf} + c_{Xf}c_{Yg}}. \tag{3.4}$$

Thus, for the combined LOR of adjacent rings f and g, the normalisation correction is calculated as:

$$n_{XY} = \frac{g_{XY}(c_{Xf}c_{Yg})(c_{Xg}c_{Yf})}{c_{Xg}c_{Yf} + c_{Xf}c_{Yg}} = \frac{g_{XY}}{\epsilon_{Xf}\epsilon_{Yg} + \epsilon_{Xg}\epsilon_{Yf}}. \tag{3.5}$$

For all other LOR's between detectors located at non-adjacent rings, equation 3.1 holds true and it is used to calculate the normalisation correction factors.

The dead-time correction has not been implemented in this study.

3.2.3 Calculation of Attenuation Correction from MRAC Image

The PIFA images are stored by the scanner, as described in this section. The scanner treats each acquisition differently to acquire their PIFA images due to

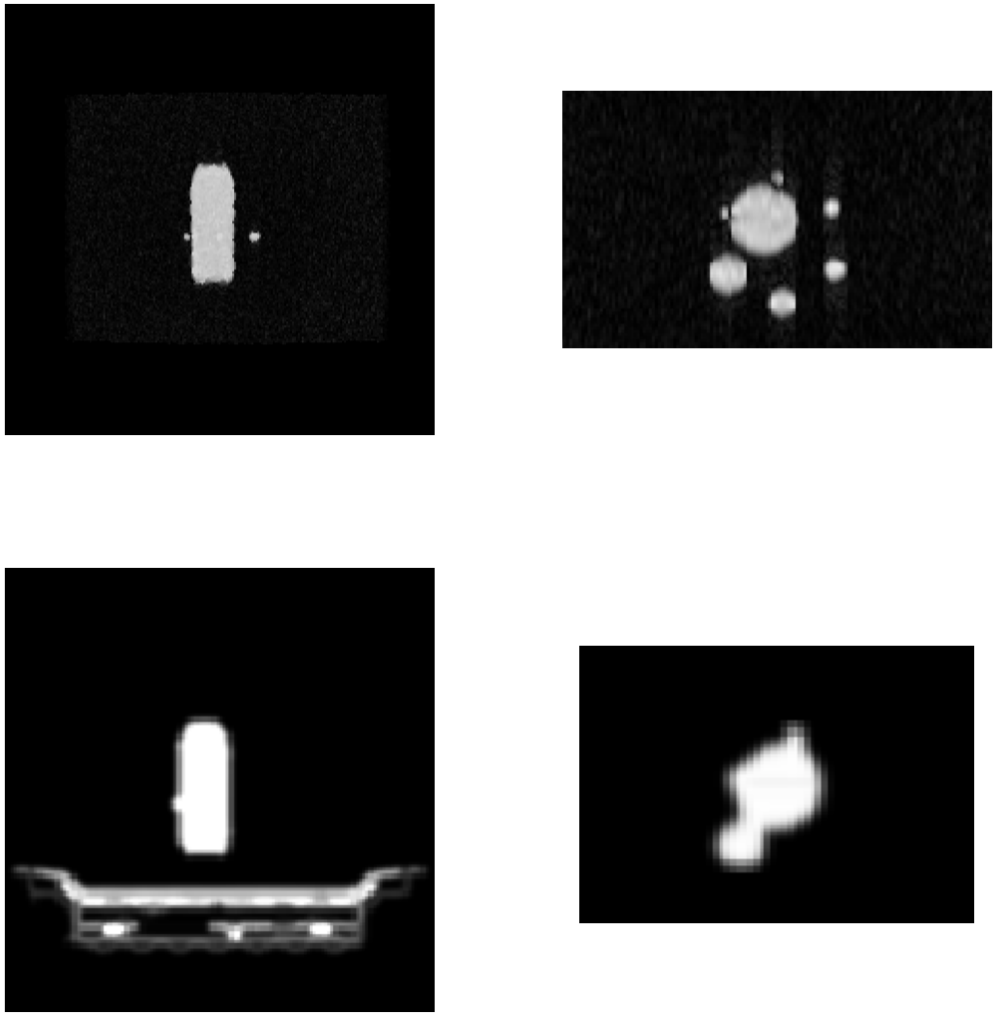

Figure 3.2: Bottle Phantom Dataset: Transverse and coronal slices of the exported and resampled PIFA image (bottom row) that are extracted using custom scripts from MRAC image (top row). MRAC image is also used as an anatomical prior for kernel matrix estimation for TOF-KEM image reconstructions. PIFA image is further used to correct for the AC after it is converted in STIR interfile format using custom scripts.

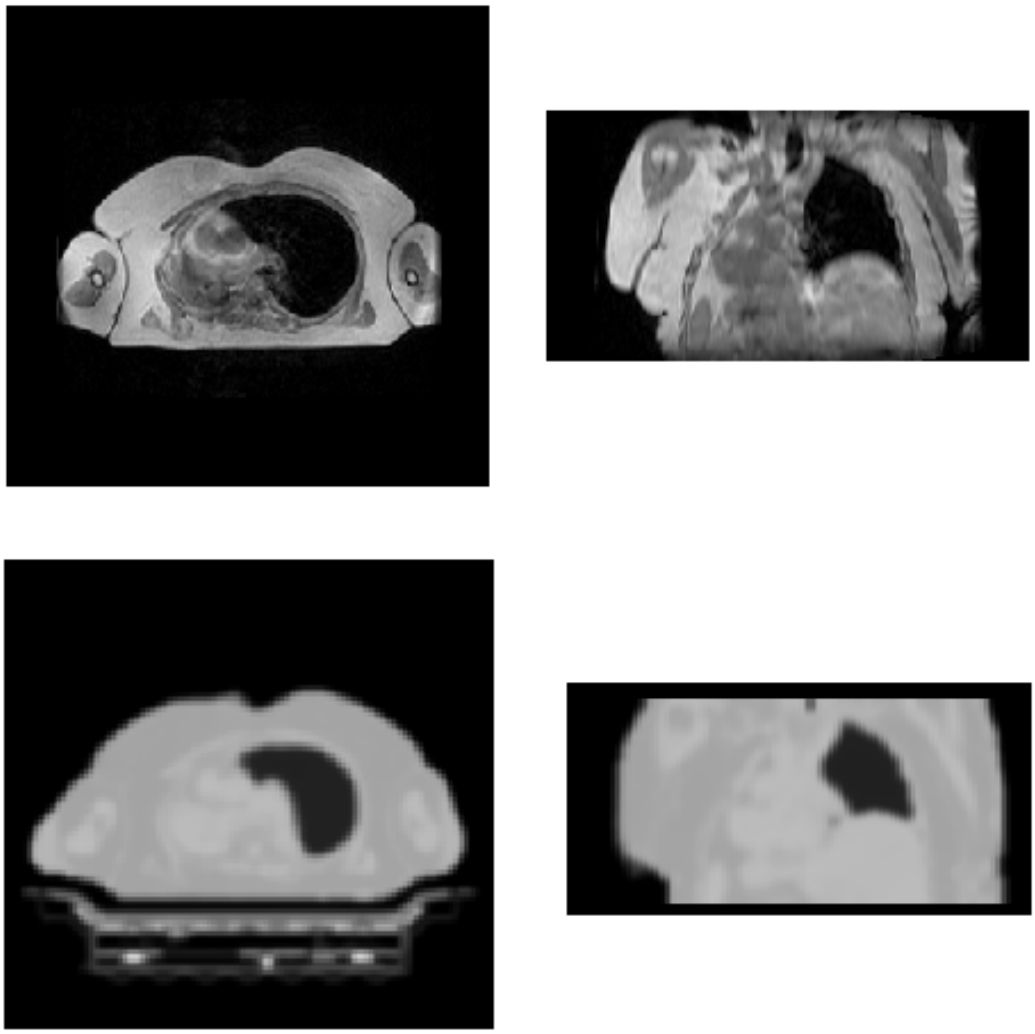

Figure 3.3: Patient Dataset: Transverse and coronal slices of the exported and resampled PIFA image (bottom row) that are extracted using custom scripts from MRAC image (top row). MRAC image is also used as an anatomical prior for kernel matrix estimation for TOF-KEM image reconstructions. PIFA image is further used to correct for the AC after it is converted in STIR interfile format using custom scripts. The patient has one lung. (Figure taken from the paper: Wadhwa *et. al.*, *PET image reconstruction using physical and mathematical modelling for time of flight PET-MR scanners in the STIR library*, Elsevier, 2020. Figure used under the terms of Creative Commons Attribution 4.0 International licence.)

its conventions.

For patient and customized phantoms such as bottle phantom (as described in section 3.6 later in this thesis), the scanner assigns the PET attenuation factors after segmenting the tissues imaged using MRAC sequences (Wadhwa et al. [2018]). The sequence that is used for acquiring MRAC image is Dixon.

For GE provided phantoms such as Hoffman (as described in section 3.6 later in this thesis), the scanner uses pre-defined templates which were implemented by taking the CT scan of the phantom assigned with PET attenuation factors. The scanner registers the templates to non-attenuation corrected PET reconstructions during the scan which accurately localises the phantom template to the position of the phantom on the gantry.

The scanner also stores PET attenuation templates for head coils, head and neck coil, breast coil and patient table. The coil used in the scan and the patient table template are added at the end of the scan to obtain the PIFA images that include non-patient objects.

Further, in the case of Volumetric Quality Control (VQC) phantom, PIFA images are not required as the phantom has negligible attenuation.

As discussed in 2.4.2, STIR utilities only accept input in its native interfile format. The PIFA file format is not a format implemented within STIR. Thus, customized MATLAB scripts were implemented and the PIFA images were converted into DICOM and further into STIR interfile file format.

3.2.4 Randoms Correction: Implementation of Randoms from Singles

LM HDF5 files store the singles rate for every second of the acquisition at the end of each scan. For an acquisition of time N seconds, there is a list of N+1 samples stored in the field called '/Singles/CrystalSingles/sample#', where every sample#[1] stores a singles rate. There are N+1 samples as the periodic data is asynchronous with the start of PET scan, which needs to be taken into account during data calculation by weighting the first and last samples of the periodic data appropriately.

The singles rate for each crystal is read and stored within a newly implemented STIR class called 'SinglesRatesFromGEHDF5'. This class reads the array with dimensions 45×448, that stores the rates of the singles. The above array that stores the singles rate per second is converted into a STIR-based histogram using a utility called 'construct_randoms_from_GESingles'.

The random events over the complete PET acquisition, T, are calculated in STIR as (Stearns et al. [2003], Oliver and Rafecas [2016]):

$$R_{XY} = 2\tau S_X S_Y / T, \tag{3.6}$$

where R_{XY} is the estimated number of random events (or counts) detected by the detector pair X and Y, τ represents the coincidence window of the scanner (the coincidence window is 4.57 ns for this scanner), T represents the total time of PET acquisition, S_X and S_Y represent the single events detected per crystals X and Y, respectively.

[1] # is replaced with the index having the units of 'seconds' starting at 1

The singles rate for each crystal are read from the LM HDF5 file to further calculate the random rates. The STIR utility 'construct_randoms_from_GEsingles' is implemented for this purpose during this work. In the current STIR implementation, dead-time and decay modelling are not considered within randoms correction.

3.2.5 Scatter Correction

Scatter correction is calculated for each dataset using already implemented single scatter simulation in STIR (Tsoumpas et al. [2004], Watson [2000], Watson et al. [1996]). The PIFA images are converted into STIR interfile image format using customised scripts. This image is used to calculate the attenuation correction factors. The emission sinogram is used along with the estimated attenuation correction to reconstruct the attenuation corrected image for a sub-sampled scanner template. This image is further used to simulate a series of random points (also called scatter points) to calculate the scattering probability for each of these points using the Klein-Nishina formula (Tsoumpas et al. [2004]). Single scatter probabilities are summed up for each scatter point in order to estimate the single scatter distribution. The single scatter distribution is estimated for each detector pair and scaled using tail-fitting to calculate the scatter correction histogram (Thielemans et al. [2007], Polycarpou et al. [2011]). The calculated scatter correction histogram is interpolated to get the scatter probability for the entire histogram for GE SIGNA PET/MR scanner.

3.3 Transformation of Histogram Data from GE Scanner to STIR Space

3.3.1 TOF Histogram Data Organisation

The calculated LOR and TOF bin numbers are converted into a complete TOF histogram using the pre-defined STIR utility 'lm_to_projdata'. This utility uses scanner template information to initialise the histogram and assign detected LOR's that are read in the class 'CListModeDataGESIGNA'.

The scanner stores each timing bin as a signed integer (i.e. numbered from -175 to +175 bins), which are 'mashed' together by combining every 13 timing bins together to produce a total of 27 histogram timing bins. The coincidence events are stored in a histogram of dimensions $224 \times 1981 \times 27 \times 357$, where 224 corresponds to the total number of views, 1981 corresponds to the total number of axial positions, 27 corresponds to the number of "mashed" timing bins and 357 corresponds to the number of tangential positions (Wadhwa et al. [2018]). The number of views, by convention, refers to half of the total number of detectors along the ring. There are 448 detectors in GE SIGNA PET/MR, resulting in 224 views. There are half the number of detectors that comprise the views as the other half of the detectors are accounted for in the part of the same histogram that stores negative segments.

3.3.2 Span 2 Implementation

The scanner stores the coincidence events as projection data with span 3 for segment 0 and span 1 for all other segments. Span 3 for segment 0 implies that

coincident events from rings having ring difference -1,0 and 1 are all combined together, resulting in 89 different axial positions. For all other segments +/- N, coincidences that correspond to rings having ring difference +/-2N and +/- (2N+1) are taken into account. This leads to 85 axial positions for segment number +/-1, 81 axial positions for segment number +/-2, and so on. When axial positions are added together for all 45 segments for this scanner, a total of 1981 axial positions are calculated. Thus, there are a total of 1981 2D sinograms within all 45 segments. This span is defined as span 2, and the data is read properly by initialising segment based sinograms accurately.

3.3.3 Transformation of LM Events from GE to STIR Space

The LM is converted to a histogram by reading the events and calculating the bin number where the event must have occurred. STIR has a fixed convention to read the detector positions in axial and transaxial directions and has a fixed projection data space with the fixed segment, axial, tangential and view convention. STIR assumes that all scanners have detector positions running in the clockwise direction along with the rings as can be seen from the back of the scanner and rings are numbered from front to back, i.e. the z-axis starts from the front of the scanner. Whereas, the scanner chooses to number its detectors along the counter-clockwise direction as seen from the back of the scanner, as demonstrated in Figure 3.5. The above mentioned conventional incongruity has been accounted for within STIR's class 'CListModeDataGESIGNA'.

The list of events stored in clinical data starts with the timestamp of 0. The scanner discards the first few recorded events during reconstruction and

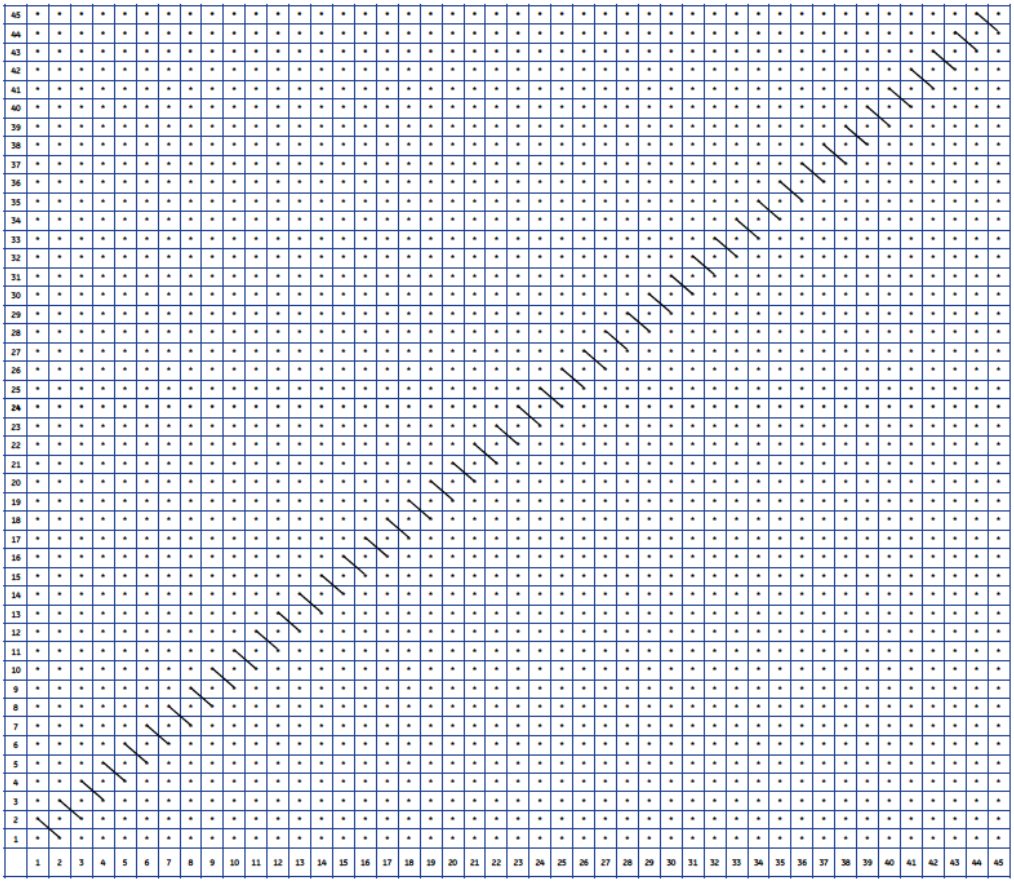

Figure 3.4: This figure presents the Michelogram for the scanner.

only use events recorded after the start of simultaneous acquisition scan. This asynchronicity in the LM file start time and acquisition start time is taken into account during the conversion of LM files into STIR histogram format using time frame definitions. The time frames are defined in seconds and are read from the header data of the HDF5 file. The acquisition start time is recorded under the field called '/HeaderData/ListHeader/firstTmAbsTimeStamp' and the acquisition time frame is recorded under the field called '/HeaderData/ListHeader/listAcqTime'.

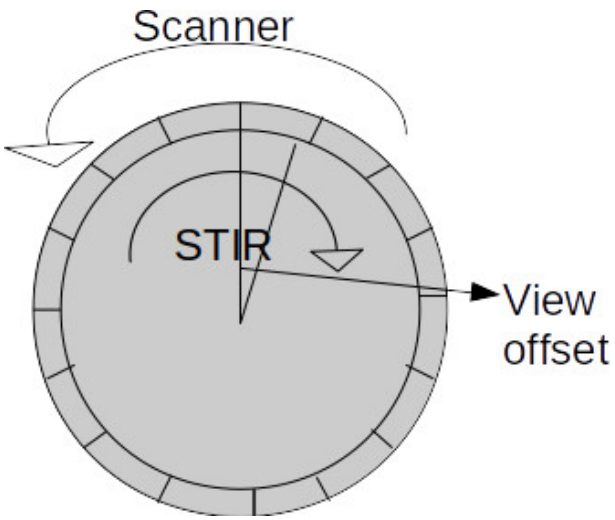

Figure 3.5: This figure represents the scanner and STIR incongruity in terms of the detector numbering. It demonstrates that the scanner reads the crystal in the counter-clockwise direction and the crystals are numbered from 0 to 447 as there are 448 crystals in total. The crystal 0 is positioned at an offset of $-5.23°$ from the $y = 0$ position as the module 0 is centered at $y = 0$. This offset for crystal 0 in the scanner is translated to be in the clockwise direction in STIR as demonstrated here.

3.3.4 Troubleshooting

The GE SIGNA PET/MR scanner has modules running in the counter-clockwise direction as seen from the back of the scanner. Module 0 of the scanner is centred at $y = 0$ and crystal 0 has a transaxial offset of $-5.23°$ (negative sign representing anti-clockwise direction). STIR adopts a different convention and initialises the scanner geometry with crystal 0 to always be located at $y = 0$. The STIR projection matrix was changed during this work to take the view offset into account. STIR stores projection data using a fixed segment sequence, which is different from the GE segment data format. The GE data organisation is presented in Figure 3.6 and it demonstrates that the projection data is organised by concatenating 2D segment based sinograms with the sequence: 0, 1, -1, 2 and so on.

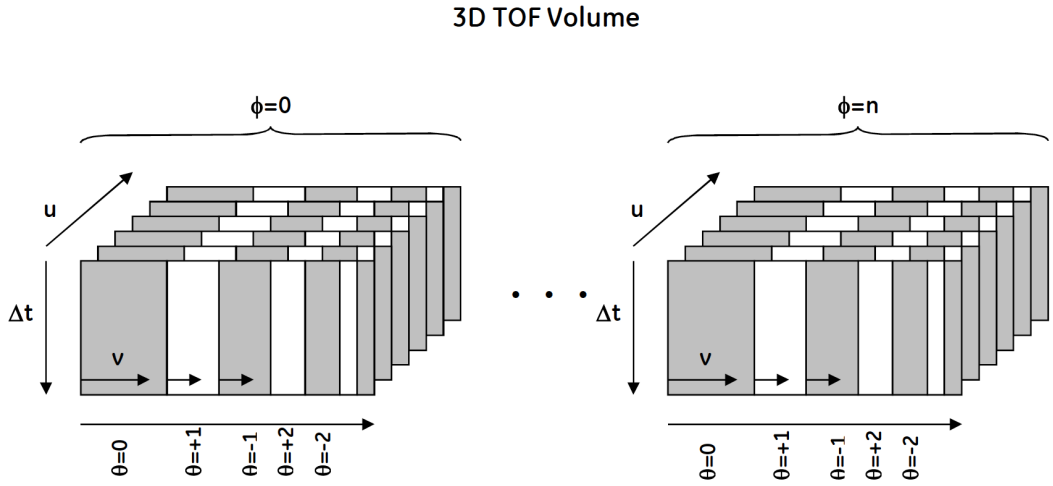

Figure 3.6: This figure demonstrates the TOF histogram data organisation as stored by the GE SIGNA PET/MR scanner. As shown in the figure, the scanner stores events in a series of 3-D TOF viewgrams for view numbers as represented by ϕ. The view numbers vary from 0 to 223 as the total number of views stored by GE SIGNA scanner are 224. The 3D TOF viewgrams are demonstrated to have a volume with dimensions of segment number as presented by θ, axial positions as presented by v, tangential positions as presented by u and TOF positions as presented by Δt. The segment numbers vary according to the segment sequence as: 0, 1, -1, 2, -2 and so on.

This is different to STIR's native projection data organisation as STIR organises its segment having sequence: 0, -1, 1, -2, and so on. This incompatibility is taken into account to read the GE data format by implementing GE based segment sequence in STIR. These are important as the lack of these implementations will lead to wrongly quantified PET images as the detected events will be assigned to the wrong bin number. Thus, it is essential to account for all the above incongruity between two data spaces in order to read the acquired data accurately within STIR space.

3.4 Acquisition Model

3.4.1 GE SIGNA PET/MR Acquisition Model in STIR

The data collected at the end of a scan with a GE SIGNA PET/MR scanner is a TOF projection data measurement, represented as y_{pt}. The sections below describe the implementation of non-TOF projection data based forward model, y, where, $y = \Sigma_t y_{pt}$ and TOF projection data based forward model, y_{pt} where t represents the TOF bins measured by the scanner.

Non-TOF Acquisition Model

For non-TOF acquired data, y_p (a vector of detected events stored for the detector pairs, p), the acquisition model for the scanner is defined as:

$$y_p = \Sigma_m a_{pm} x_m + b_p; \tag{3.7}$$

where $[a_{pm}]$ represents the system matrix, which models the probability of event emitted in voxel m to be detected by detector pair p, x_m represents the image vector with voxels m, and b_p represents the vector of background events detected along detector pair p. Background events represent the sum of non-TOF randoms and scattered events.

- The normalisation correction and attenuation correction factors are included in the system matrix $[a_{pm}]$. The system matrix is calculated by multiplying forward and back projectors using Hadamard or element-wise multiplication along with the normalisation and attenuation factors for each voxel and detector pair combination to calculate the corresponding

matrix element (Mehranian and Zaidi [2015]).

- The randoms and scatter correction histogram together form the background term, b_p.

TOF Acquisition Model

GE SIGNA TOF-PET measured projection data, y_{pt} is modelled within the acquisition model as:

$$y_{pt} = \Sigma_m a_{ptm} x_m + b_{pt}; \tag{3.8}$$

where $[a_{ptm}]$ represents the system matrix which models the probability of event emitted in voxel m to be detected by detector pair p within the signed TOF bin, t, x_m represents the image vector with voxels m, $[b_{pt}]$ represents the matrix of background events detected along the detector pair p and within TOF bin t.

- The TOF kernel is modelled within the system matrix a_{ptm} as (Efthimiou et al. [2019]):

$$a_{ptm} = a_{pm} T_{ptm}. \tag{3.9}$$

This equation models the time spread function as a matrix, T_{ptm} for each TOF bin t and separates it from the sensitivity information stored within the matrix, a_{pm}. The sensitivity information models the system effects such as scanner geometry, detector efficiency, geometric, attenuation effects and projection matrix.

The coincidence window width of the scanner is equally divided into t TOF bins with the bin boundary being $[k_t, k_{t+1}]$ as can be seen in Figure 3.7. The time spread function represents the system response to a point source

located at voxel m and TOF bin t having boundaries $[k_t, k_{t+1}]$. The time spread function is typically modelled as a Gaussian function with mean located at v'_{cm} and standard deviation, $\sigma = R_t(8ln2)^{-\frac{1}{2}}$, where R_t represents the timing resolution of the scanner Mehranian et al. [2016]. As can be seen in Figure 3.7, v'_{cm} is the orthogonal projection of the center c of the voxel m within timing bin t.

The probability that the event having projection v'_{cm}, is detected within the TOF bin t, having boundaries $[k_t, k_{t+1}]$ is computed as the *cdf* or the cumulative distribution function. Since time spread function is a Gaussian distribution, the $cdf(k_t - v'_{cm})$ is equivalent to the $\frac{1}{2}[1+(erf(\frac{k_t - v'_{cm}}{\sigma\sqrt{2}})]$, where erf represents the error function. Similarly, the $cdf(k_{t+1} - v'_{cm})$ is equivalent to the $\frac{1}{2}[1 + (erf(\frac{k_{t+1} - v'_{cm}}{\sigma\sqrt{2}})]$ (Efthimiou et al. [2019]).

Thus, the time spread function T_{ptm} is calculated as (Efthimiou et al. [2019]):

$$T_{ptm} = cdf(k_{t+1} - v'_{cm}) - cdf(k_t - v'_{cm}) = \frac{1}{2}(erf(\frac{k_{t+1} - v'_{cm}}{\sigma\sqrt{2}}) - erf(\frac{k_t - v'_{cm}}{\sigma\sqrt{2}})), \tag{3.10}$$

In the above equation 3.9, time spread function is calculated as equation 3.10 and multiplied together with a_{pm} to calculate the system matrix a_{ptm}.

- The scatter and randoms correction TOF histograms are added together to calculate the background term, b_t.

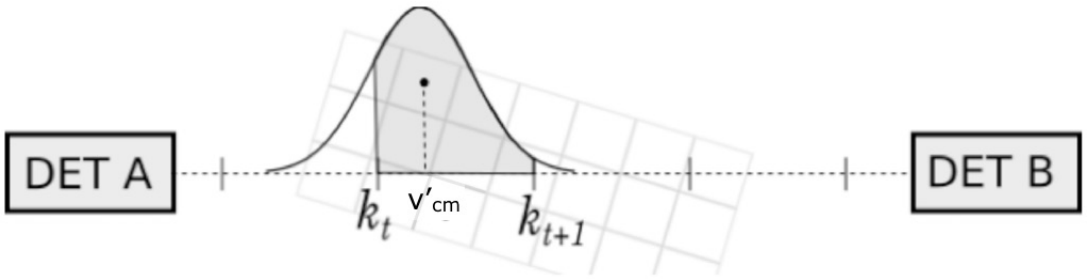

Figure 3.7: This figure shows the orthogonal projection of the event that is detected in voxel m with center c within the timing bin t as v'_{cm}. The event is detected within the TOF bin t having boundaries, k_t and k_{t+1}. This figure also illustrates the time spread function for TOF bin t as a Gaussian distribution. (Figure taken from the paper: Efthimiou *et. al.*, *Implementation and validation of time-of-flight PET image reconstruction module for listmode and sinogram projection data in the STIR library*, Institute of Physics and Engineering in Medicine, 2019. Figure used under the terms of Creative Commons Attribution 3.0 licence.)

3.4.2 Scanner Geometrical Modelling in STIR

Table 3.1: GE SIGNA PET/MR Scanner Specifications

Number of detectors per ring	448
Number of rings	45
Ring Spacing	$5.56mm$
Transaxial FOV	$600mm$
Depth of Interaction	$8.5mm$
Crystal Information	$5.3 \times 3.95 \times 25mm^3$
Number of non arc-corrected bins	357
Number of arc-corrected bins	331
Bin Size	$2.13mm$
Intrinsic Tilt Angle	$-5.23°$
View Number	224
Number of TOF bins	351
Timing Least Significant Bit	$13.02ps$
Timing Resolution	$390ps$

When a scanner is defined in STIR, it uses a pre-defined cylindrical geom-

etry (STIR currently supports only cylindrical PET scanners) and conventions to model parameters within the system matrix. STIR uses scanner parameters, such as the number of detectors per ring, number of rings, ring spacing, transaxial FOV, depth of interaction, blocks and crystal information to initialise the scanner geometry. The number of transaxial and axial blocks per module, number of crystals per block and the crystal layers information are defined within the scanner geometry information. The number of non arc-corrected and arc-corrected bins (i.e. tangential position numbers), bin size and the intrinsic tilt angle information are also stored to initialise the histogram. The number of detectors per ring is used to initialise the view numbers, which defines the projection data. Further to this, TOF information, including the number of TOF bins, timing least significant bit and timing resolution of the scanner are also initialised. The histogram array is initialised for the GE SIGNA PET/MR scanner within STIR according to the geometrical and hardware information as described in table 3.1.

3.5 TOF-KEM

The combination of previously implemented advanced reconstruction algorithms, TOF-OSEM and KEM, has been demonstrated in this work. This combination has given the foundation for novel reconstruction algorithm, TOF-KEM.

3.5.1 Theory

The statistical distribution of the measured noisy TOF PET data, y_{pt} that is extracted from the scanner can be mathematically modelled as:

$$y_{pt} \sim Poisson(\sum_{m \in M} a_{ptm} x_m + r_{pt} + s_{pt}) \tag{3.11}$$

Further, kernel based PET image model as described in equation 2.40 and a_{ptm} as described in equation 3.9 is substituted in equation 3.11 as:

$$y_{pt} \sim Poisson(\sum_{f} a_{pm} T_{ptm} k_{fm} \lambda_f + r_{pt} + s_{pt}) \tag{3.12}$$

The scanner stores the data in t TOF bins spaced over the entire coincidence window of 4.57 ns. There are 351 TOF bins over the total coincidence window which leads to each timing bin having a width of 13.02 ps.

The acquisition model as described in equation 2.1 is modified according to equation 3.12 as below:

$$y = ATK\lambda + b, \tag{3.13}$$

where $y = [y_{pt}]$ represents the measured TOF data, $T = [T_{ptm}]$ represents a TOF kernel matrix with each element representing the time spread function, $K = [k_{fm}]$ represents the kernel matrix constructed using MR feature vectors $\nu = 1, ..., N_m$ extracted from the MR anatomical image, where N_m represents the number of feature vectors, $\lambda = [\lambda_f]$ represents a vector of kernel weights and $b = [b_{pt}]$ represents the background term.

Thus, standard expectation maximization algorithm can be used to estimate

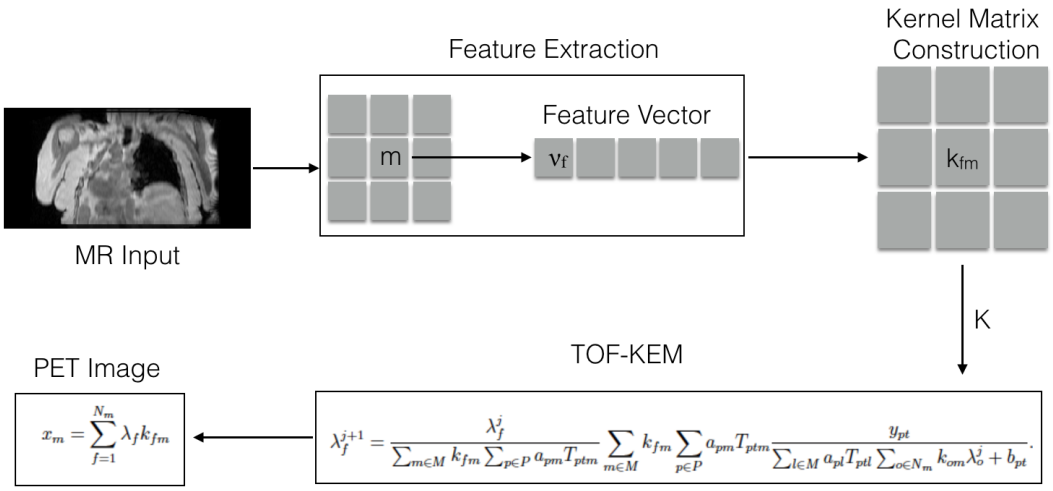

Figure 3.8: Schematic Representation of TOF-KEM algorithm.

the kernel weights, λ for TOF-PET data, y_{pt} as:

$$\lambda_f^{j+1} = \frac{\lambda_f^j}{\sum_{m\in M} k_{fm} \sum_{p\in P} a_{pm} T_{ptm}} \sum_{m\in M} k_{fm} \sum_{p\in P} a_{pm} T_{ptm} \frac{y_{pt}}{\sum_{l\in M} a_{pl} T_{ptl} \sum_{o\in N_m} k_{om} \lambda_o^j + b_{pt}}. \tag{3.14}$$

The final estimate of PET image, $\hat{x}$ reconstructed using TOF-KEM algorithm is obtained by substituting equation 3.14 in equation 2.40.

3.5.2 Kernel Matrix Construction

The kernel matrix comprises of basis functions that utilizes the spatial information from a MR image which is co-registered and resampled to match PET. The basis functions are basically constructed using the feature vectors, ν_m where each feature vector represents the voxel intensities within a patch extracted from MR image where the patch is basically a cubic array of voxels centered around voxel m.

Gaussian kernels are used to construct the kernel matrix and the elements of the kernel matrix K are defined as:

$$k_{fm} = exp\Big(- \frac{\|\nu_f - \nu_m\|^2}{2\sigma_m^2}\Big) exp\Big(- \frac{\|x_f - x_m\|^2}{2\sigma_{dm}^2}\Big), \tag{3.15}$$

where k_{fm} represents the $(fm)^{th}$ element of kernel matrix K, k_{fm} is basically a basis function comparing feature vector ν_f with the all other feature vectors ν_m, ν_f and ν_m represents the feature vector for voxel f and m respectively, σ_m represents a scaling parameter which is chosen to scale the distance between the feature vectors and it controls the edge sensitivity, x_f and x_m represents the position vector of voxel f and m respectively, σ_{dm} represents the scaling parameter chosen to scale the distance between the position vector of voxel.

3.6 Data Acquisition

The data used in this study is collected using the GE SIGNA TOF PET/MR scanner located at Invicro, Imperial College London, Hammersmith Hospital, London, UK. The study also uses the STIR and GE-toolbox to reconstruct the acquired phantom and clinical datasets as described below.

The study to collect the phantom data was designed by the candidate. The phantom data was collected by the candidate along with the assistance of GE engineer and collaborator at Invicro. Whereas, clinical dataset were given for this study by collaborators at Invicro.

MRAC images, PIFA images, uncompressed PET LM and RDF files were exported from the scanner for all phantom and clinical acquisitions.

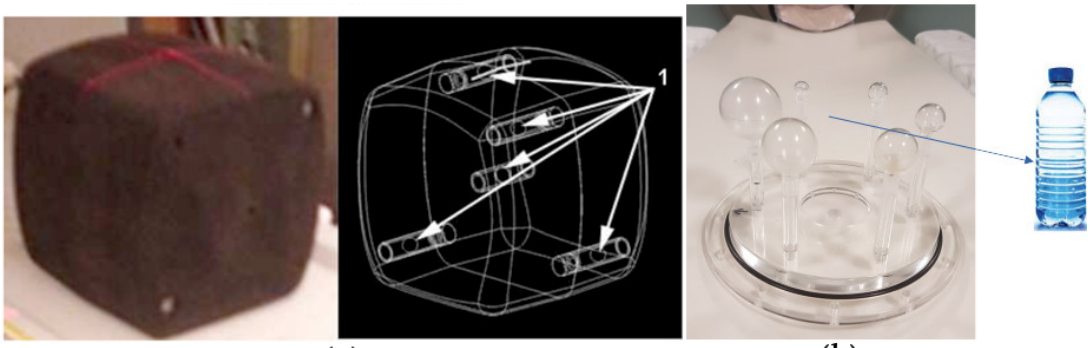

Figure 3.9: (a) VQC Phantom: Five ^{68}Ge spheres having an activity diameter of 19 mm and an activity diameter of 17 mm are combined to form the VQC phantom. These spheres are encased within the $NiCl_2$ tubes and are placed at the locations as can be seen in the figure. This configuration is then encased within the solid cube. (b) Bladder Mimicking Bottle Phantom consists of 6 radioactive spheres and a 500 ml radioactive bottle placed between smallest spheres (Wadhwa et al. [2018]).

3.6.1 Phantom Dataset

1. VQC Phantom: Five small ^{68}Ge spheres with a physical diameter of 19 mm but radioactivity diameter of 17 mm are placed in five different locations as can be seen in figure 3.9 (a). The radioactive spheres are embedded within MR-visible tubes made of $NiCl_2$. Originally this phantom was used to observe the misalignment between MR and PET gantries, whereas, in this study, it is used to validate the reconstructions. These are low radiation spheres with 0.7 MBq radioactivity in each sphere. The entire configuration is encased within the foam cube. The phantom was scanned for 10 minutes, and there were 5×10^6 prompts registered.

2. Bottle Phantom: National Electrical Manufacturers Association Image Quality (NEMA IQ) phantom is modified by removing the phantom wall

as can be seen in figure 3.9. The remaining phantom, that was used in this study, consists of 6 fillable spheres with diameters varying from 10 mm to 37 mm which were filled with 5.38 MBq of [^{18}F]-FDG (Boellaard et al. [2015]). A high activity bottle filled with 77.9 MBq of [^{18}F]-FDG was further added to the phantom. This bottle touches two of the smallest spheres. The phantom was scanned for 5 minutes, and there were 5×10^8 prompts registered at the end of the scan.

3. Hoffman Phantom (Hoffman et al. [1990]): The Hoffman phantom is injected with 22.9 MBq of 18F-FDG. The scan was conducted for 20 minutes resulting in 1.5×10^8 prompts.

3.6.2 Clinical Dataset

A patient with fibrosis of the lung was injected with 40.62 MBq of an experimental ^{18}F radiotracer, 90 minutes prior to the scan. The scan duration was 13 minutes, resulting in 3.8×10^7 prompts. The patient is missing one of his lungs.

3.7 Image Reconstruction

3.7.1 Image Reconstruction with STIR

The scanner acquired uncompressed LM data converted into TOF STIR histogram using the existing 'lm_to_projdata' utility.

Data correction histograms were calculated, using custom utilities and parameter classes within STIR, for this scanner. Normalisation corrections were

calculated using the 'correct_projdata' utility with parameters set to read data from the 'norm3d' file exported from the scanner. Attenuation correction was carried out using the exported PIFA images, as illustrated in Figure 3.2. An important point to note is that the VQC phantom had negligible attenuation and thus, attenuation correction was not needed. Randoms correction histogram was calculated using 'construct_randoms_from_GEsingles' utility. Scatter correction was done using the histogram extracted from the vendor's reconstruction toolbox. Since, VQC phantom had negligible attenuation, scatter correction was also not needed. For TOF image reconstruction, the TOF histogram data were calculated using the LM file. Randoms and scatter correction histograms were translated into TOF projection data by developing custom utilities and appropriate scaling of data. This was done by using non-TOF 4D histogram data repeated over all the TOF bins to form a 5D TOF data. Each bin value was scaled using appropriate scaling. The scaling parameter used to construct TOF randoms histogram was equal to total number of TOF bins. Whereas, to construct TOF scatter histogram varying scaling parameters were used to scale each bin proportional to the number of counts within respective bin. This is because, lower number of counts leads to lower scattered events (Watson [2007]). This is a very primitive modelling of scatter correction for TOF data and cannot be considered as a substitue for TOF scatter. The custom utilities were developed as TOF scatter correction is not implemented yet in STIR (Watson [2007]). Attenuation and normalisation histograms were uniform in timing bins and were multiplied with the background term to create an additive histogram for STIR implementations. Image reconstruction were carried out using TOF-OSEM algorithms with and without point spread function (PSF) modelling. The PSF modelling used here

is applied in image space and is already implemented in STIR. The image space modelling is carried out using the resolution values which are 4.2 mm in transaxial and 5.8 mm in axial directions respectively (Vandenberghe et al. [2016]).

Patient dataset was reconstructed using TOF-KEM algorithm as well. The images used as the input to construct the kernel matrix for TOF-KEM reconstructions were:

- Dixon 'in-phase' MR image as shown in Figure 3.3 (top row),
- TOF-OSEM PET image as shown in Figure 3.10 (a), and
- TOF-OSEM+G (TOF-OSEM image post-filtered with Gaussian filter having Full Width Half Maximum (FWHM) of 4 mm) PET image as shown in Figure 3.10 (b).

The Dixon 'in-phase' MR images were resampled and manually aligned to match PET FOV. The MR images were resampled to matrix of $256 \times 256 \times 89$ with voxel size of $2.3 \times 2.3 \times 2.8$. Further, TOF-OSEM and TOF-OSEM+G images were reconstructed using STIR with 28 subsets and 2 iterations. The reconstruction obtained at 2^{nd} iteration was chosen to reduce the noise in the input image.

Bladder phantom was also reconstructed with TOF-KEM algorithm by using Dixon 'in-phase' MR image as shown in Figure 3.2, as input to construct the kernel matrix.

VQC and Hoffman phantom does not have any appropriate MR images and thus, this thesis does not contain TOF-KEM reconstructions using VQC and Hoffman.

The standard number of subsets used for this scanner in the clinical scenario is 28 subsets. Thus, all reconstructions were carried out with 28 subsets.

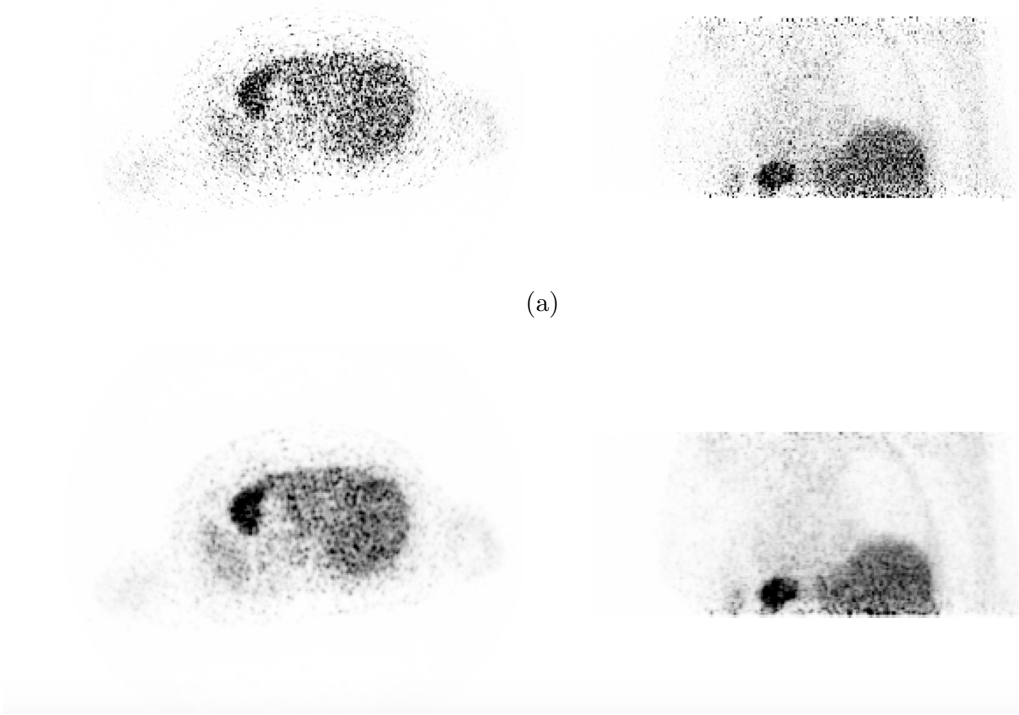

(a)

(b)

Figure 3.10: This figure shows the PET images that are used as inputs to construct the kernel matrix for TOF-KEM reconstruction: (a) TOF-OSEM (b) TOF-OSEM+G (TOF-OSEM image post-filtered with Gaussian filter having FWHM of 4 mm). The images were reconstructed with STIR using 28 subsets and 2 iterations.

3.7.2 Image Reconstruction with GE-Toolbox

GE proprietary reconstruction algorithms, including VUE Point FX (or fully 3D TOF iterative reconstruction which is further referred to TOF-OSEM-GE) and VUE point FX SharpIR (or PSF-TOF-OSEM-GE) (Ross and Stearns [2010], Vandendriessche et al. [2019]), were used to reconstruct VQC, Hoffman and patient datasets with 28 subsets.

3.8 Image Analysis

Emission and data correction histograms, exported from the scanner, are calculated using the implementations made in STIR and then compared using voxelwise subtraction to the GE extracted histogram. TOF-OSEM reconstructions with STIR and the GE-toolbox (or 'GE') for the VQC phantom were used to compare the FWHM (Delso et al. [2011b]). FWHM was calculated using a STIR utility called 'find_fwhm_in_image', for all five spheres for GE-toolbox and STIR based reconstruction. The FWHM for all spheres in all three dimensions were averaged and the standard error was calculated as the tolerance window as defined in equation 3.16.

$$FWHM = \sum_{i=1}^{n=5} \frac{FWHM_i}{n} \pm \sqrt{\frac{(FWHM_i - (\sum_{i=1}^{n=5} FWHM_i/n))^2}{n}}. \quad (3.16)$$

In the equation 3.16, $FWHM_i$ represents the calculated FWHM for sphere i, where i varies from 1 to $n = 5$.

Images obtained with TOF-OSEM reconstructions with STIR and vendor's reconstruction toolbox for the patient dataset were compared using Standardised Uptake Value Ratio (SUVR) and coefficient of variation (CoV). SUVR is calculated as the ratio of the SUV of target and reference regions as defined in equation 3.17

$$SUVR = \frac{SUV_{target}}{SUV_{lung}}. \quad (3.17)$$

In this study, regions of interest (ROI), drawn within the liver and spleen, were used as the target, and another ROI of the same volume, within the lung, was used as the reference as illustrated in Figure 3.11.

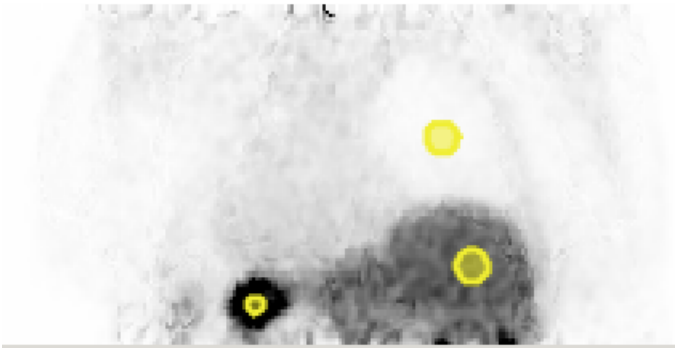

Figure 3.11: The ROIs placed in target regions: liver and spleen, and reference region: lung.

CoV is calculated as the standard deviation over the mean, as a percentage, as defined in equation 3.18

$$CoV = \frac{StandardDeviation}{Mean} * 100. \tag{3.18}$$

STIR images reconstructed with and without TOF were compared using CoV for bottle and Hoffman phantom. This was done to study the performance of TOF reconstruction over the iterations.

STIR images were also compared with the GE-toolbox images using the Structural Similarity Index Measure (SSIM) as described in (Wang et al. [2004]). The global SSIM values are reported as the similarity measure between STIR and GE reconstructed images and is calculated as:

$$SSIM(x, y) = [l(x, y)][c(x, y)][s(x, y)], \tag{3.19}$$

where $l(x, y)$ is the luminance term, $c(x, y)$ is the contrast term and $s(x, y)$ is the structural term. In the above equation, x and y represents a pair of images to be compared.

In equation 3.19 (Wang et al. [2004]),

$$l(x,y) = \frac{2\mu_x\mu_y + C_1}{\mu_x^2 + \mu_y^2 + C_1}, \tag{3.20}$$

where $\mu_x = \frac{1}{N}\sum_{i=1}^{N} x_i$ and $\mu_y = \frac{1}{N}\sum_{i=1}^{N} y_i$ represents the local mean for images x and y respectively with voxels $i = 1, 2, 3, ..., N$. $C_1 = KL$ represents a constant that prevents the denominator in equation 3.20 from going to zero, where $K << 1$ and $L = 255$ (Wang et al. [2004]).

$$c(x,y) = \frac{2\sigma_x\sigma_y + C_2}{\sigma_x^2 + \sigma_y^2 + C_2} \tag{3.21}$$

where $\sigma_x = \sqrt{\frac{1}{N-1}\sum_{i=1}^{N}(x_i - \mu_x)^2}$ and $\sigma_y\sqrt{\frac{1}{N-1}\sum_{i=1}^{N}(y_i - \mu_y)^2}$ represents the standard deviation for images x and y respectively with voxels $i = 1, 2, 3, ..., N$, $C_2 = K'L$ represents a constant that prevents the denominator in equation 3.21 from going to zero, where $K' << 1$ and $L = 255$ (Wang et al. [2004]).

$$s(x,y) = \frac{\sigma_{xy} + C_3}{\sigma_x\sigma_y + C_3} \tag{3.22}$$

where $\sigma_{xy} = \frac{1}{N-1}\sum_{i=1}^{N}(x_i - \mu_x)(y_i - \mu_y)$ represents the cross-covariance of the images x and y, σ_x and σ_y represents the standard deviation for images x and y respectively and $C_3 = \frac{C_2}{2}$ (Wang et al. [2004]).

The similarity measure evaluates the image quality of the calculated image with respect to the reference in order to check the level of distortion in the calculated image. This metrics is highly applicable for the comparisons demonstrated in this study as the reconstructed images using novel iterative algorithms are compared to their clinical counterparts. Particularly, TOF-KEM reconstruction

algorithm utilises the anatomical information from MR to guide PET reconstruction which could lead to introduction of bias in PET reconstructed images. The SSIM comparison metrics can indicate the structural distortion due to MR anatomical information over PET reconstructions. Further, this metrics is also helpful to indicate if the acquisition model implemented in STIR yields images close to the GE-toolbox. The closer the value of SSIM is to 1 for a pair of images, the more similar the images are.

The global SSIM values are calculated for TOF-OSEM-STIR versus TOF-OSEM-GE, TOF-KEM-STIR versus TOF-OSEM-GE, PSF-TOF-OSEM-STIR versus PSF-TOF-OSEM-GE and PSF-TOF-KEM-STIR versus PSF-TOF-OSEM-GE, where STIR images are considered as distorted images, and GE images are considered as reference images. The comparisons are carried out for reconstructed images over the first six iterations.

3.9 Summary

This chapter describes in detail the major software developments required to read and reconstruct TOF-PET data from the GE SIGNA PET/MR scanner. This chapter also describes the implementations needed to allow data correction for this scanner with STIR. Finally, this chapter theoretically describes the novel TOF-KEM algorithm, which has been implemented during this work in STIR to demonstrate quantitative improvements with PET data. It describes the acquisition data, image reconstruction settings and the analysis conducted to compare different iterative reconstruction algorithms. The next chapter presents the results that were produced and compares the different reconstruction algorithms

and software, as defined above.

Chapter 4

Results

This chapter presents the results that illustrate the developments described in previous chapters. The results presented in this chapter demonstrate the calculation of emission and data correction histograms and PET reconstruction conducted with already available and newly implemented novel reconstruction algorithms. Here, PET histograms and reconstructed images using STIR and GE-toolbox are compared. The histogram-based comparisons are made for both non-TOF and TOF PET data using voxel-wise subtraction. The reconstructions are compared for OSEM, TOF-OSEM and TOF-KEM algorithms using SUVR, FWHM, CoV and SSIM metrics.

4.1 Histogram Comparisons

4.1.1 Non-TOF

Figure 4.1 compares the non-TOF emission, normalisation and randoms correction histograms calculated from GE-toolbox and STIR for the VQC phantom

dataset. This figure also shows the voxel-wise subtracted histograms, which compares the calculated histograms extracted from STIR and GE-toolbox. The top, middle and the bottom rows of the figure displays the emission, normalisation and randoms histogram for segment 0 and axial position 45, respectively along with the estimated difference histogram. The comparisons displayed here are for display purposes only and the choice of segment and axial position does not affect the results. If any other segment or axial position is chosen, the comparisons would still demonstrate the same results, i.e. the emission histogram are identical, whereas, normalisation correction histogram have negligible differences and small differences are observed in randoms correction histogram.

The comparisons were made after pre-processing the STIR histograms back into GE space. This was done by inverting the view and tangential positions of histograms calculated with STIR. Histograms stored in GE space (i.e. read by GE-toolbox) have view numbers and tangential positions running in opposite directions as compared to STIR space (i.e. read by STIR). This is a native conventional choice of each software. In order to compare the histograms calculated by each software, the conventional asymmetry must be resolved. Thus, the pre-processing of STIR histogram here and later is required to translate it into GE space and compare the histograms in same space.

4.1.2 TOF

TOF emission histograms extracted using the STIR and GE-toolbox for the VQC phantom were compared for every TOF bin, segment number, axial position, view number and tangential position. Figure 4.2 demonstrates the TOF emission histogram for only TOF bins 0 and 5. The histogram are displayed for

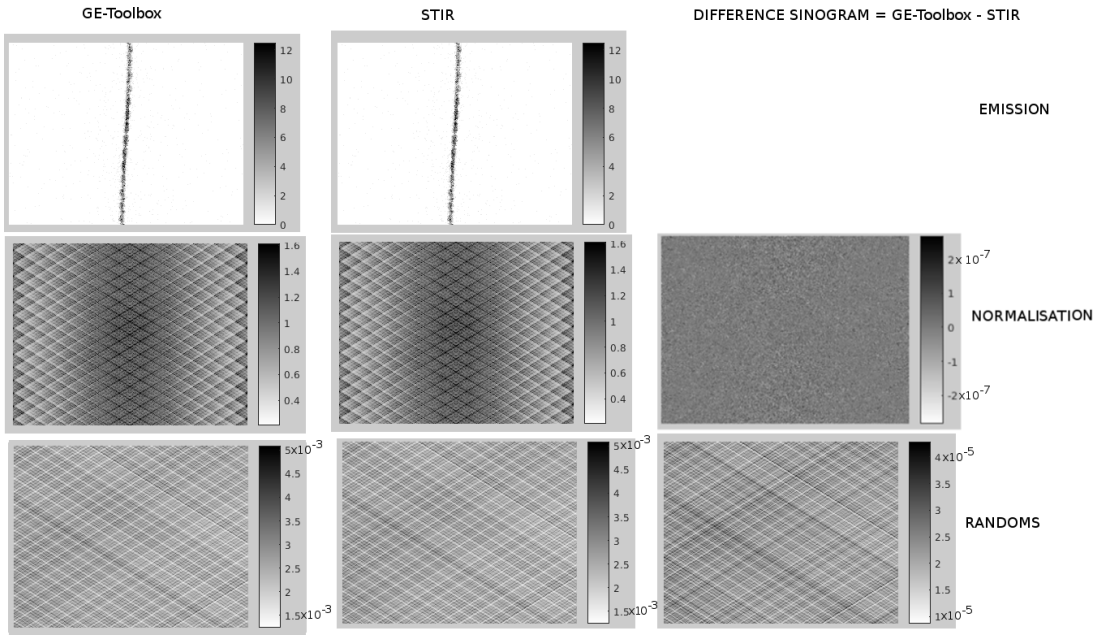

Figure 4.1: Non-TOF emission, normalisation and randoms histograms for VQC phantom datasets exported from GE-toolbox and STIR along with the difference. (Figure taken from the paper: Wadhwa *et. al.*, *PET image reconstruction using physical and mathematical modelling for time of flight PET-MR scanners in the STIR library*, Elsevier, 2020. Figure used under the terms of Creative Commons Attribution 4.0 International licence.)

segment number 0 and axial position 18. The TOF bin numbers, segment number and axial position are chosen in an arbitrary manner and are only for display purposes. The choice of segment number and axial position here and later does not affect the result and the TOF emission histograms are completely identical regardless of the segment number, TOF bin number, axial position, tangential position or view number.

TOF emission histograms extracted using the STIR and GE-toolbox for the Hoffmann phantom were compared for every TOF bin, segment number, axial position, view number and tangential position. Figure 4.3 compares the TOF emission histograms for only TOF bins 0 and 2. The histograms are displayed

for segment number 0 and axial position 46. The TOF bin numbers, segment number and axial position are chosen in an arbitrary manner and are only for display purposes.

All comparisons were made after pre-processing the STIR histograms to convert them back into GE space.

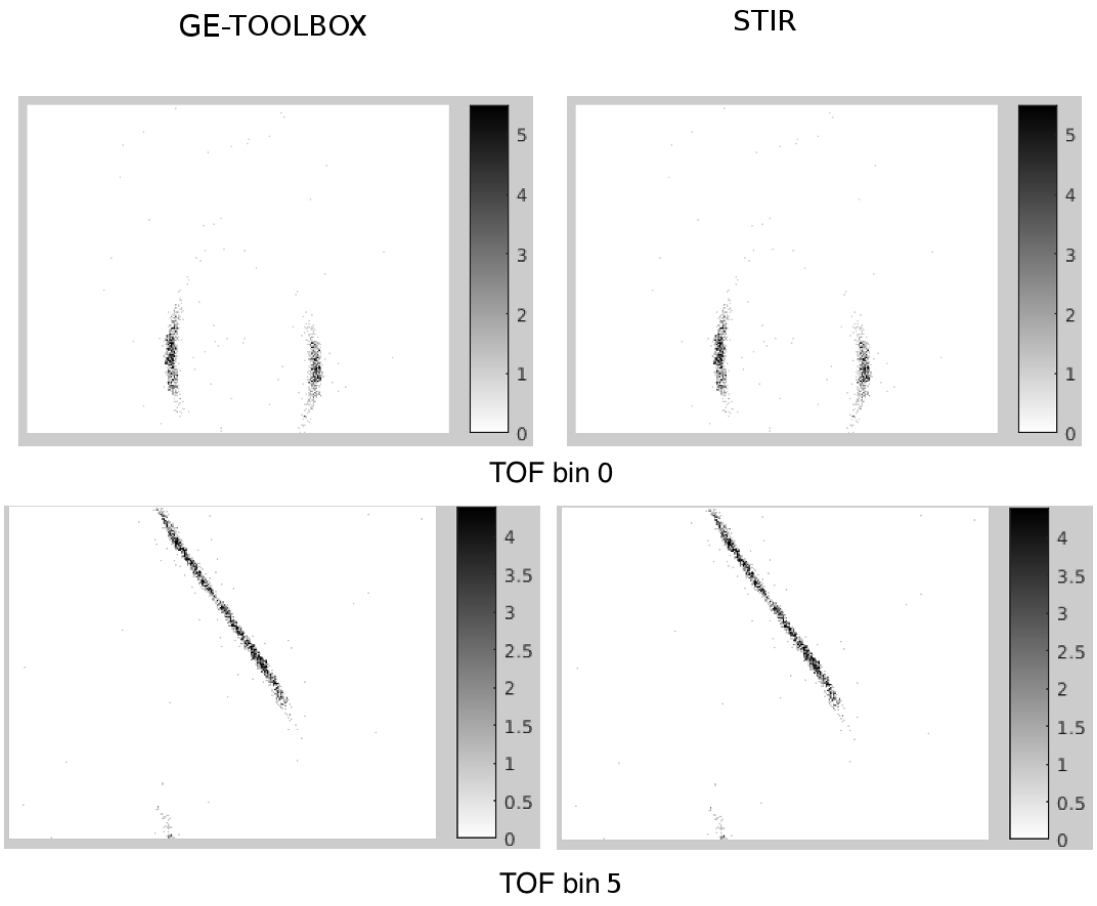

Figure 4.2: TOF histograms for TOF bin 0 (top row) and 5 (bottom row) exported from GE-toolbox and STIR for the VQC phantom dataset. All histograms are for segment 0 and axial position 18. (Figure taken from the paper: Wadhwa *et. al.*, *PET image reconstruction using physical and mathematical modelling for time of flight PET-MR scanners in the STIR library*, Elsevier, 2020. Figure used under the terms of Creative Commons Attribution 4.0 International licence.)

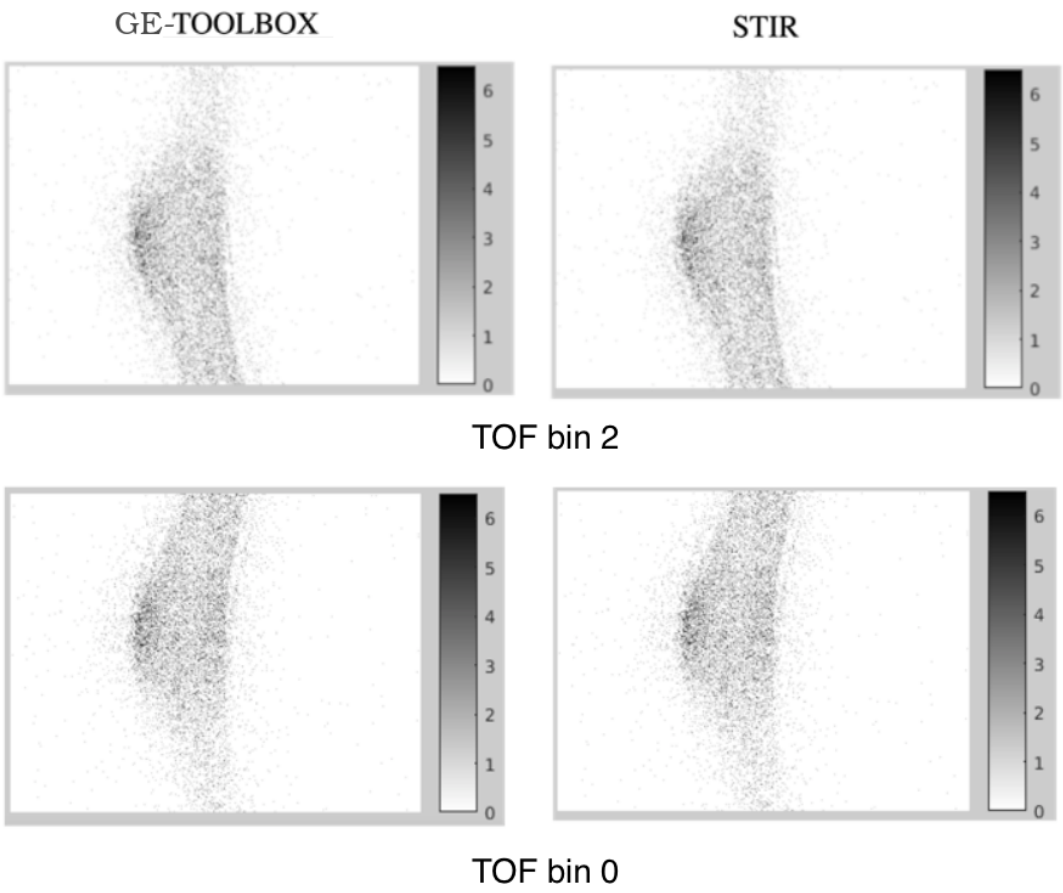

Figure 4.3: TOF histograms for TOF bin 2 (top row) and 0 (bottom row) exported from GE-toolbox and STIR for the Hoffman phantom dataset. All histograms are for segment 0 and axial position 46.

4.2 Comparison of Reconstructions

For comparing image reconstructions visually, 2 or 3 iterations have been used as per standard clinical protocol. Particularly, for TOF-OSEM and TOF-KEM reconstructions, 2^{nd} iteration is used as they are visually the best images in terms of image noise. Further, 6 iterations have been used to compare the reconstructions quantitatively using the CoV and SSIM. The behaviour of different

algorithms is observed over the iterations using CoV and SSIM. 6^{th} iteration has been used to demonstrate the SUVR comparisons as the SUVR value was found to be nearly constant over the iterations and thus, later iteration was chosen due to convergence of algorithm at later iterations.

4.2.1 Non-TOF

All the examples mentioned in this section compare the images reconstructed with STIR and GE-toolbox visually. All the images in this section were reconstructed using 28 subsets and 3 iterations. The images used for demonstration purpose in this section are reconstructions with 3 iterations as in clinical scenario reconstructions are stopped after 2 or 3 iterations. Further, 3 iterations demonstrate the less bias for OSEM reconstruction as compared to 2 iterations.

Figure 4.4 shows the reconstructed images using non-TOF histograms calculated using the STIR implementation. The figure has four rows and two columns where each row contains four different datasets: VQC, bottle, Hoffman and clinical dataset respectively; and two columns represent STIR and GE-toolbox comparisons for the same dataset. The images were reconstructed using the OSEM algorithm (STIR) and VUE-point HD algorithm (GE-toolbox). The images were reconstructed as a $305 \times 305 \times 89$ array with a voxel size of $2.02 \times 2.02 \times 2.78$ mm^3.

Figure 4.5 shows the transverse and coronal slices of the reconstructed images for bottle phantom. The images shown were reconstructed with OSEM-STIR (OSEM algorithm with STIR) and OSEM-GE (VUE-point HD algorithm with GE-toolbox) in $256 \times 256 \times 89$ array with the voxel size of $2.34 \times 2.34 \times 2.78$ mm^3.

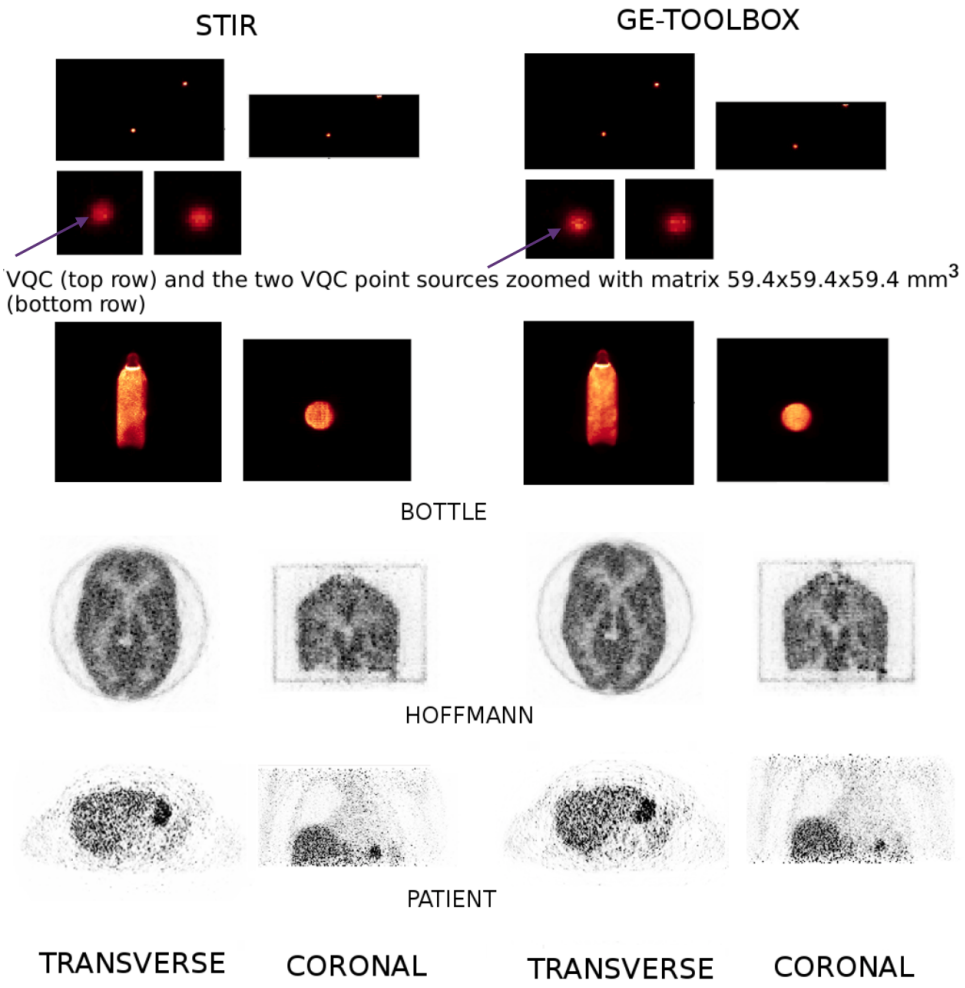

Figure 4.4: Image Comparison: STIR and GE-Toolbox. Offset between reconstructed images using GE and STIR are pointed out using purple arrows in the image (Wadhwa et al. [2018]).

Figure 4.6 shows the transverse and coronal slices of the reconstructed images for the Hoffman phantom. The view offset correction is applied to the STIR reconstructions. The images are also aligned manually to GE-toolbox for optimal comparisons. The alignment between STIR and GE-toolbox is necessary as the PET images extracted from STIR are reconstructed in PET space of the scanner whereas GE-toolbox conventionally registers the PET image with MR

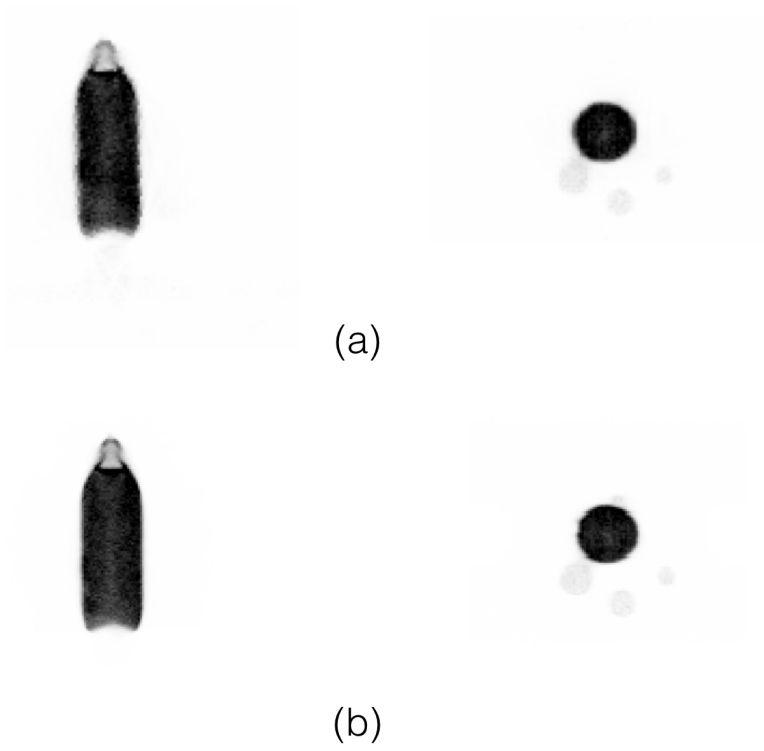

Figure 4.5: Bottle Phantom: Transverse and coronal slice comparisons for (a) OSEM-STIR (OSEM algorithm with STIR) (b) OSEM-GE (VUE-point HD algorithm with GE-toolbox) . Comparisons are made for images reconstructed with 28 subsets and 3 iterations.

and translate the PET images into MR space. This implies that PET images reconstructed using STIR and GE-toolbox are not in the same space and cannot be compared unless the STIR image is aligned with MR space.

The reconstructions are conducted using OSEM-STIR (OSEM algorithm with STIR) and OSEM-GE (VUE-point HD algorithm with GE-toolbox). The images were reconstructed as a $256 \times 256 \times 89$ array with the voxel size of $2.34 \times 2.34 \times 2.78$ mm^3.

Figure 4.7 shows the transverse and coronal slices of the reconstructed images for the Hoffman phantom. The reconstructions shown in this figure were

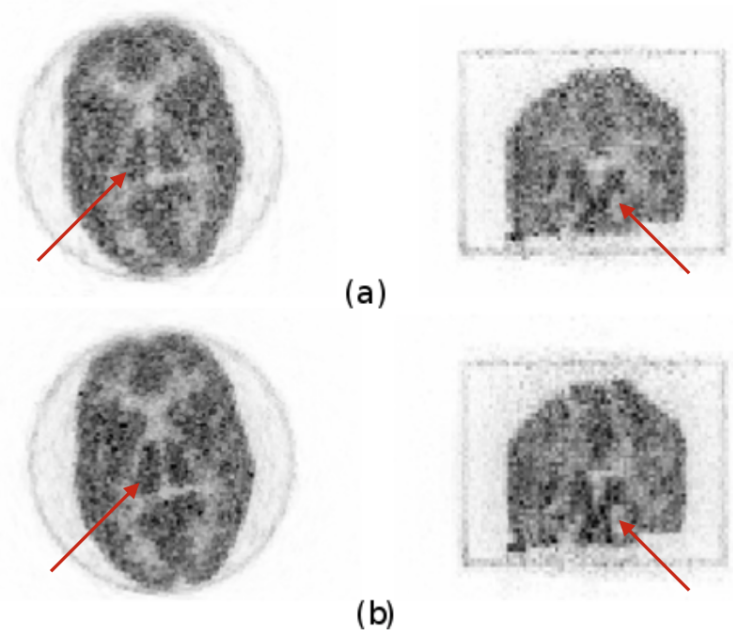

Figure 4.6: Hoffman Phantom: Transverse and coronal slice comparisons for (a) OSEM-STIR (OSEM algorithm with STIR) and (b) OSEM-GE (VUE-point HD algorithm with GE-toolbox). Comparisons are made for images reconstructed with 28 subsets and 3 iterations. Structural differences between reconstructed images using GE and STIR are pointed out using red arrows in the image (Wadhwa et al. [2020]).

conducted using PSF-OSEM-STIR (PSF-OSEM algorithm with STIR) and PSF-OSEM-GE (VUE-point HD SharpIR algorithm with GE-toolbox). The images were reconstructed in $256 \times 256 \times 89$ array with the voxel size of $2.34 \times 2.34 \times 2.78$ mm^3.

Figure 4.8 shows the transverse and coronal slices of the reconstructed images for clinical dataset. The images shown were reconstructed with OSEM-STIR (OSEM algorithm with STIR) and OSEM-GE (VUE-point HD algorithm with GE-toolbox) in $256 \times 256 \times 89$ array with the voxel size of $2.34 \times 2.34 \times 2.78$ mm^3.

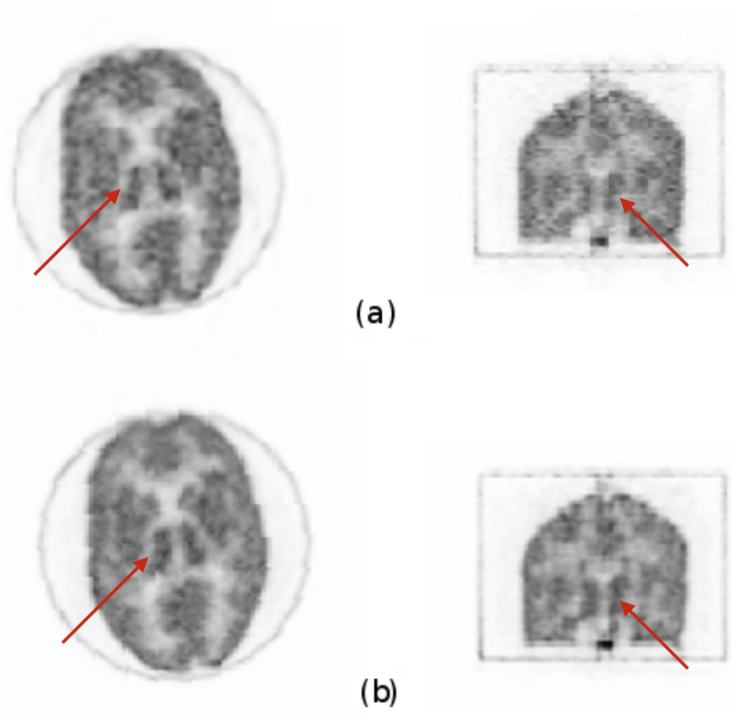

Figure 4.7: Hoffman Phantom: Transverse and coronal slice comparisons for (a) PSF-OSEM-STIR (PSF-OSEM algorithm with STIR) and (b) PSF-OSEM-GE (VUE-point HD SharpIR algorithm with GE-toolbox). Comparisons are made for images reconstructed with 28 subsets and 3 iterations. Structural differences between reconstructed images using GE and STIR are pointed out using red arrows in the image (Wadhwa et al. [2020]).

Figure 4.9 shows the transverse and coronal slices of the reconstructed images for the clinical dataset. The images were reconstructed with PSF-OSEM-STIR (PSF-OSEM algorithm with STIR) and PSF-OSEM-GE (VUE-point HD SharpIR algorithm with GE-toolbox). The images were reconstructed in $256 \times 256 \times 89$ matrix with the voxel size of $2.34 \times 2.34 \times 2.78\ mm^3$.

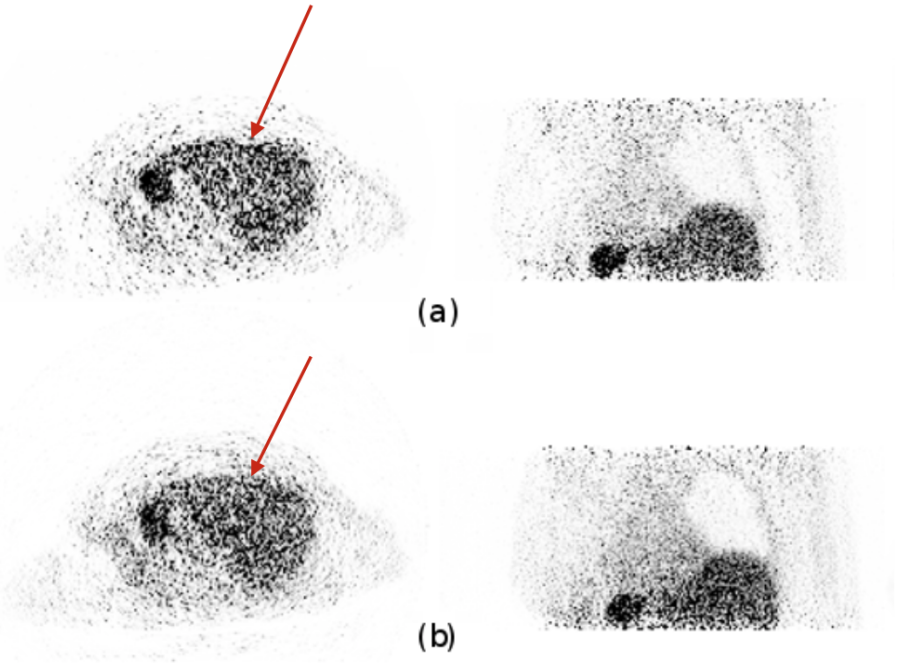

Figure 4.8: Patient Dataset: Transverse and coronal slice comparisons for (a) OSEM-STIR (OSEM algorithm with STIR) and (b) OSEM-GE (VUE-point HD algorithm with GE-toolbox). Comparisons are made for images reconstructed with 28 subsets and 3 iterations. Structural differences between reconstructed images using GE and STIR are pointed out using red arrows in the image (Wadhwa et al. [2020]).

4.2.2 TOF

All the images in this section were reconstructed using 28 subsets and 2 iterations. The images were reconstructed in $256 \times 256 \times 89$ matrix with the voxel size of $2.34 \times 2.34 \times 2.78\ mm^3$. The image reconstructions over 2 iterations are used in this section as this is consistent with the clinical scenario. Further, the reconstructions demonstrated here have been chosen to reduce the noise characteristics introduced due to iterative reconstructions.

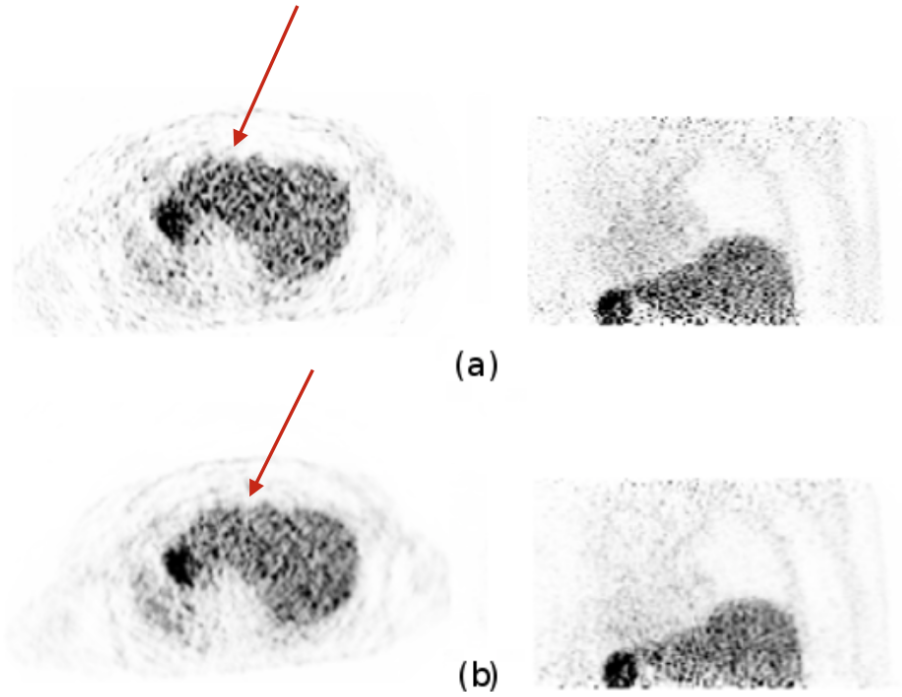

Figure 4.9: Patient Dataset: Transverse and coronal slice comparisons for (a) PSF-OSEM-STIR (PSF-OSEM algorithm with STIR) and (b) PSF-OSEM-GE (VUE-point HD SharpIR algorithm with GE-toolbox). Comparisons are made for images reconstructed with 28 subsets and 3 iterations. Structural differences between reconstructed images using GE and STIR are pointed out using red arrows in the image (Wadhwa et al. [2020]).

Figure 4.10 shows the transverse and coronal slices of the reconstructed images for the bottle phantom. This figure has three sub-parts: (a) TOF-OSEM-GE (VUE-point FX algorithm with GE-toolbox) post-filtered with Gaussian filter having the FWHM of 4 mm; (b) TOF-OSEM-STIR (TOF-OSEM algorithm with STIR) post-filtered with Gaussian filter having the FWHM of 4 mm; (c) TOF-KEM-STIR (TOF-KEM algorithm with STIR).

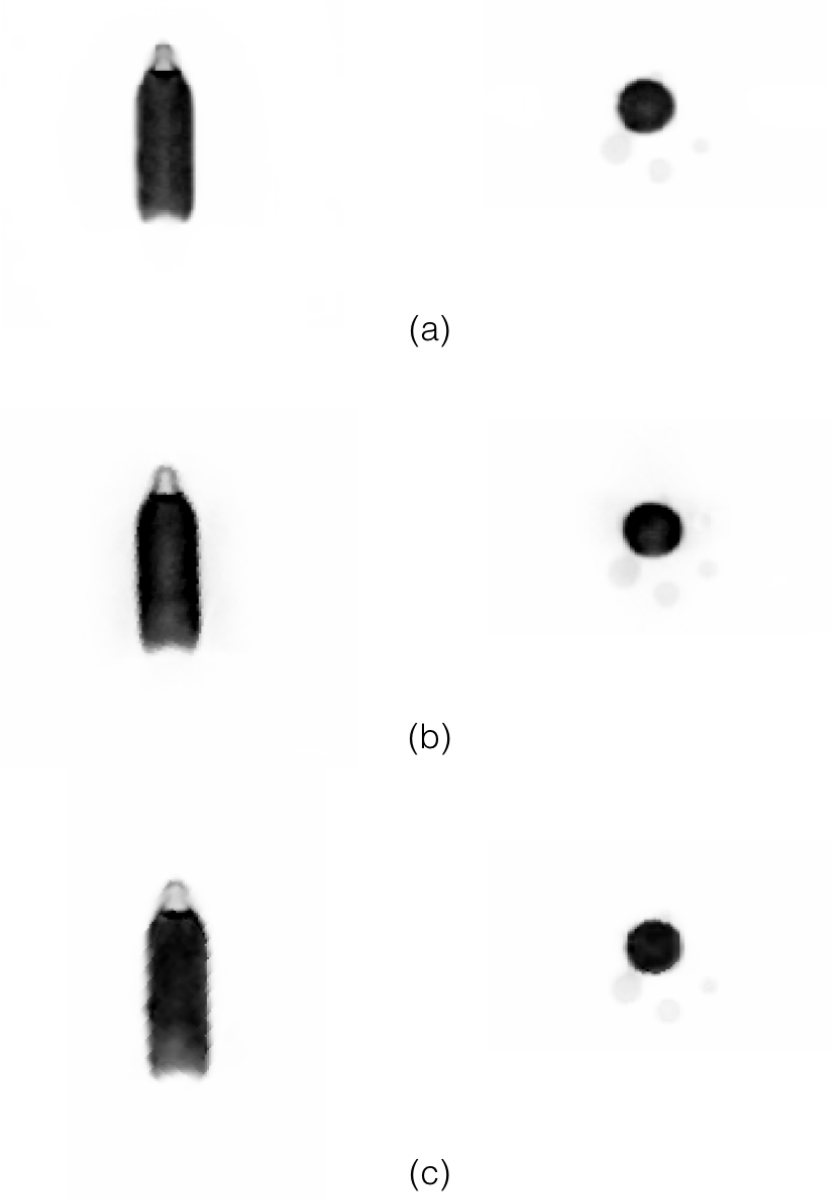

Figure 4.10: Bottle Phantom: Transverse and coronal slice comparisons for (a) TOF-OSEM-GE (VUE-point FX algorithm with GE-toolbox) (b) TOF-OSEM-STIR (TOF-OSEM algorithm with STIR) and (c) TOF-KEM-STIR (TOF-KEM algorithm with STIR). Comparisons are made for images reconstructed with 28 subsets and 2 iterations. Gaussian post-filtering with FWHM of 4mm was applied to TOF-OSEM images.

(a)

(b)

Figure 4.11: Hoffman Phantom: Transverse and coronal slice comparisons for (a) TOF-OSEM-STIR (TOF-OSEM algorithm with STIR) and (b)TOF-OSEM-GE (VUE-point FX algorithm with GE-toolbox). Comparisons are made for images reconstructed with 28 subsets and 2 iterations. Gaussian post-filtering with FWHM of 4mm was applied to TOF-OSEM images.

Figure 4.11 shows the transverse and coronal slices of the reconstructed images for the Hoffman phantom. The images shown were reconstructed with TOF-OSEM-STIR (TOF-OSEM algorithm with STIR) and TOF-OSEM-GE (VUE-point FX algorithm with GE-toolbox). The reconstructions were post-filtered with Gaussian filter having the FWHM of 4 mm.

Figure 4.12 shows the transverse and coronal slices of the reconstructed im-

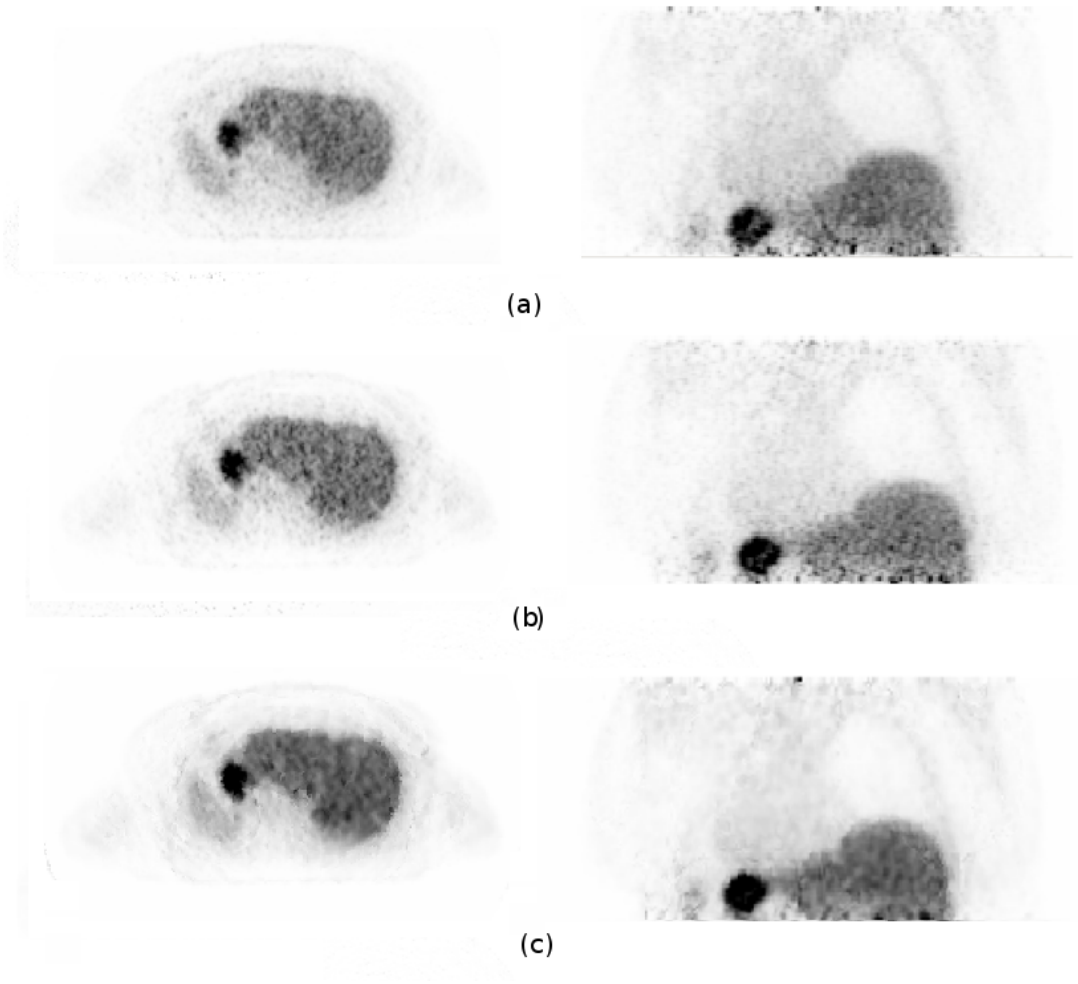

Figure 4.12: Patient Dataset: Transverse and coronal slice comparisons for (a) TOF-OSEM-GE (VUE-point FX algorithm with GE-toolbox), (b) TOF-OSEM-STIR (TOF-OSEM algorithm with STIR) and (c) TOF-KEM-STIR (TOF-KEM algorithm with STIR). Comparisons are made for images reconstructed with 28 subsets and 2 iterations. Gaussian post-filtering with FWHM of 4mm was applied to TOF-OSEM images. (Figure taken from the paper: Wadhwa *et. al.*, *PET image reconstruction using physical and mathematical modelling for time of flight PET-MR scanners in the STIR library*, Elsevier, 2020. Figure used under the terms of Creative Commons Attribution 4.0 International licence.)

ages for the clinical dataset. This figure has three sub-parts: (a) TOF-OSEM-GE reconstructions (VUE-point FX algorithm with GE-toolbox) post-filtered

with Gaussian filter having the FWHM of 4 mm; (b) TOF-OSEM-STIR reconstructions (TOF-OSEM algorithm with STIR) post-filtered with Gaussian filter having the FWHM of 4 mm; (c) TOF-KEM-STIR reconstructions (TOF-KEM algorithm with STIR).

Figure 4.13 shows the transverse and coronal slices of the reconstructed images for the clinical dataset. This figure has three sub-parts: (a) PSF-TOF-OSEM-GE reconstructions (VUE-point FX SharpIR algorithm with GE-toolbox) post-filtered with Gaussian filter having the FWHM of 4 mm. (b) PSF-TOF-OSEM-STIR reconstructions (PSF-TOF-OSEM algorithm with STIR) post-filtered with Gaussian filter having the FWHM of 4 mm. (c) PSF-TOF-KEM-STIR reconstructions (PSF-TOF-KEM algorithm with STIR).

4.3 FWHM Comparisons

4.3.1 Non-TOF

Table 4.1: FWHM Comparisons: VQC Phantom

Algorithm	Iteration	GE	STIR
OSEM	1	14.1±0.4	13.5±0.4
	2	14.4±0.3	13.6±0.4
	3	14.3±0.3	13.4±0.4
PSF-OSEM	1	13.1±0.5	13.6±0.4
	2	13.1±0.4	13.1±0.4
	3	14.3±0.3	12.3±0.5

Table 4.1 shows the FWHM comparison of reconstructions conducted using GE-toolbox and STIR. The reconstructed images with 28 subsets for the first 3

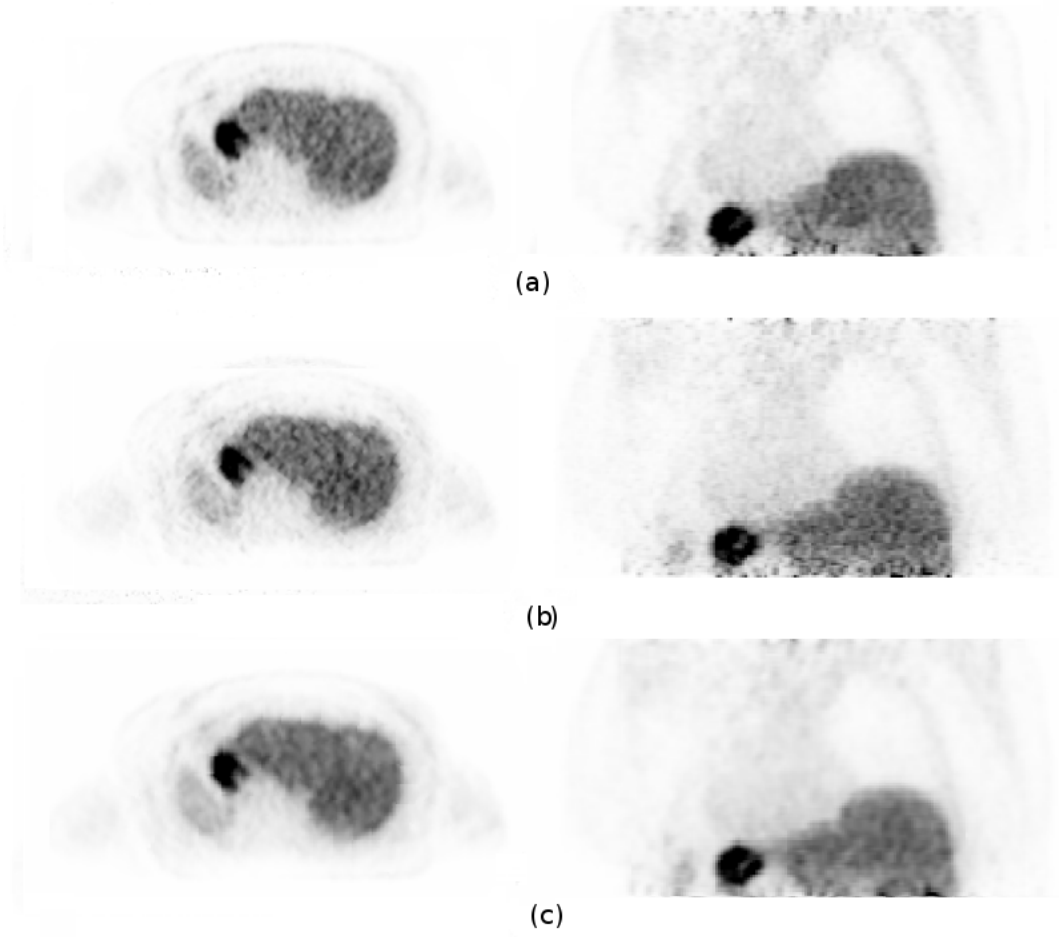

Figure 4.13: Patient Dataset: Transverse and coronal slice comparisons for (a) PSF-TOF-OSEM-GE (VUE-point FX SharpIR algorithm with GE-toolbox), (b) PSF-TOF-OSEM-STIR (PSF-TOF-OSEM algorithm with STIR) and (c) PSF-TOF-KEM-STIR (PSF-TOF-KEM algorithm with STIR). Comparisons are made for images reconstructed with 28 subsets and 2 iterations. Gaussian post-filtering with FWHM of 4mm was applied to PSF-TOF-OSEM images. (Figure taken from the paper: Wadhwa *et. al.*, *PET image reconstruction using physical and mathematical modelling for time of flight PET-MR scanners in the STIR library*, Elsevier, 2020. Figure used under the terms of Creative Commons Attribution 4.0 International licence.)

iterations were used to calculate the FWHM values. The comparisons are shown as an average of the FWHM of all the five ^{68}Ge spheres of the VQC phantom

along all three spatial dimensions. The table presents the results with OSEM-STIR (OSEM algorithm with STIR) or OSEM-GE (VUE-point HD algorithm with GE-toolbox) and PSF-OSEM-STIR (PSF-OSEM algorithm with STIR) or PSF-OSEM-GE (VUE-point HD SharpIR with GE-toolbox) algorithms. These results give a comparison of the resolution achieved by the reconstructed images for a three-dimensional sphere.

4.3.2 TOF

Table 4.2: FWHM Comparisons: VQC Phantom

Algorithm	Iteration	GE	STIR
TOF-OSEM	1	14.7±0.2	13.9±0.4
	2	14.5±0.2	13.9±0.4
	3	14.4±0.2	13.6±0.3
PSF-TOF-OSEM	1	13.0±0.5	13.6±0.4
	2	13.1±0.4	13.7±0.4
	3	12.7±0.5	13.9±0.4

Table 4.2 shows the FWHM comparisons for reconstructions conducted using GE-toolbox and STIR. The reconstructed images with 28 subsets and up to 3 iterations were used to calculate the FWHM values. The table presents the results with TOF-OSEM-STIR (TOF-OSEM algorithm with STIR) or TOF-OSEM-GE (VUE-point FX with GE-toolbox) and PSF-TOF-OSEM-STIR (PSF-TOF-OSEM with STIR) or PSF-TOF-OSEM-GE (VUE-point FX SharpIR with GE) algorithms.

4.4 SUVR Comparisons

4.4.1 Non-TOF

Table 4.3: SUVR(liver/lung) Comparisons: Patient Dataset

Algorithm	GE	STIR
OSEM	21.8	21.8
PSF-OSEM	22.6	20.5

Table 4.4: SUVR(spleen/lung) Comparisons: Patient Dataset

Algorithm	GE	STIR
OSEM	28.0	34.0
PSF-OSEM	28.9	28.9

Tables 4.3 and 4.4 show the SUVR comparisons for liver and spleen with respect to lungs for the clinical dataset. The comparisons are made for a ROI selected in all three regions of the reconstructed images and presented here for the 6^{th} iteration. The comparisons are made between OSEM-STIR (OSEM algorithm with STIR) and OSEM-GE (VUE-point HD with GE-toolbox) as well as PSF-OSEM-STIR (PSF-OSEM with STIR) and PSF-OSEM-GE (VUE-point HD SharpIR with GE-toolbox) algorithms.

The SUVR comparison is a quantitative comparison and the PET reconstruction have less bias at greater iterations. Thus, 6^{th} iterations is used here as the comparisons are based on comparing the images quantitatively.

4.4.2 TOF

Tables 4.5 and 4.6 show the SUVR comparisons for liver and spleen with respect to lungs for the clinical dataset. The comparisons are made between

TOF-OSEM-STIR (TOF-OSEM with STIR) and TOF-OSEM-GE (VUE-point FX with GE-toolbox) as well as TOF-PSF-OSEM-STIR (TOF-PSF-OSEM with STIR) and TOF-PSF-OSEM-GE (VUE-point FX SharpIR with GE-toolbox) algorithms. The table also shows the SUVR values for images reconstructed with TOF-KEM-STIR (TOF-KEM with STIR) and PSF-TOF-KEM-STIR (PSF-TOF-KEM with STIR) algorithms. All comparisons are made for reconstructions obtained with 28 subsets and 6 iteration.

Table 4.5: SUVR(liver/lung) Comparisons: Patient Dataset

Algorithm	GE	STIR
TOF-OSEM	25.5	18.5
PSF-TOF-OSEM	25.7	17.1
TOF-KEM-STIR	-	18.8
PSF-TOF-KEM-STIR	-	17.3

Table 4.6: SUVR(spleen/lung) Comparisons: Patient Dataset

Algorithm	GE	STIR
TOF-OSEM	34.0	29.3
PSF-TOF-OSEM	35.0	25.5
TOF-KEM-STIR	-	29.4
PSF-TOF-KEM-STIR	-	25.4

4.5 Coefficient of Variation (CoV)

4.5.1 Non-TOF vs. TOF:STIR

Figure 4.14 shows CoV comparisons for a ROI placed within the white matter (ROI is displayed in the top left corner of the figure). Graph compares the CoV for OSEM and TOF-OSEM algorithms with STIR for Hoffman phantom.

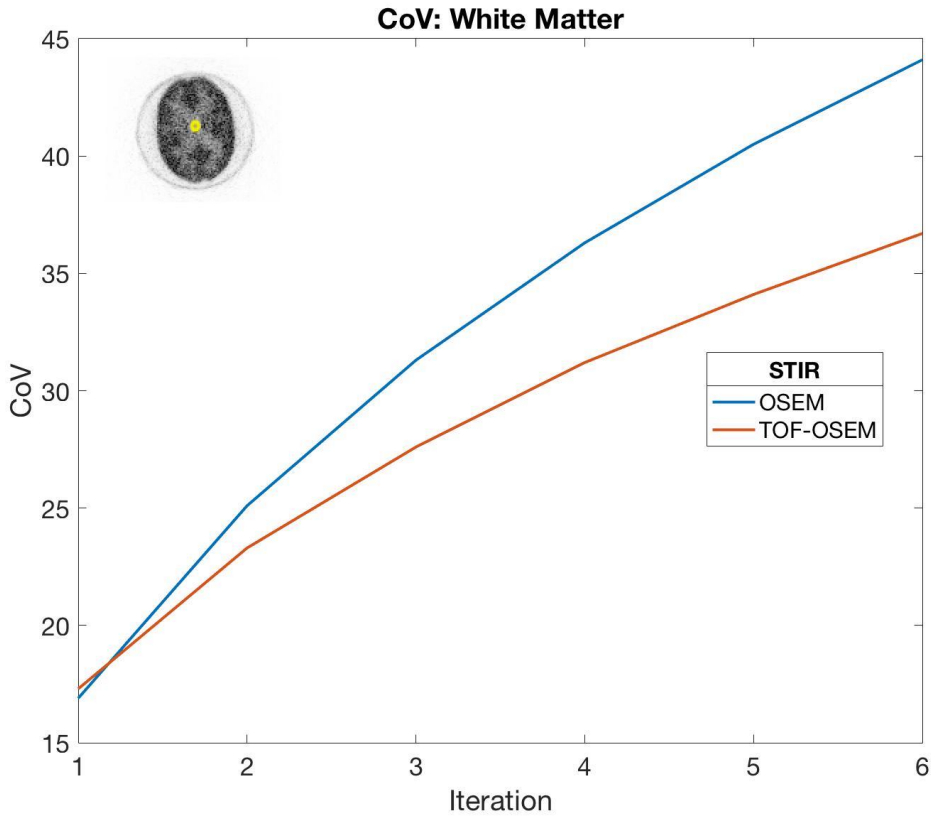

Figure 4.14: Hoffman Phantom: CoV comparisons for OSEM and TOF-OSEM with STIR for ROI placed within the White Matter as shown in the top left corner of the image.

Figure 4.15 shows CoV comparisons for a ROI placed within the gray matter (ROI is displayed in the top left corner of the figure). Graph compares the CoV for OSEM and TOF-OSEM algorithms with STIR for Hoffman phantom.

Figure 4.16 shows CoV comparisons for a ROI placed within the bottle (ROI is displayed in the top left corner of the figure). Graph compares the CoV for OSEM, TOF-OSEM and TOF-KEM algorithms with STIR for bottle phantom.

Figure 4.17 shows CoV comparisons for a ROI placed within the sphere (ROI is displayed in the top left corner of the figure). Graph compares the CoV for

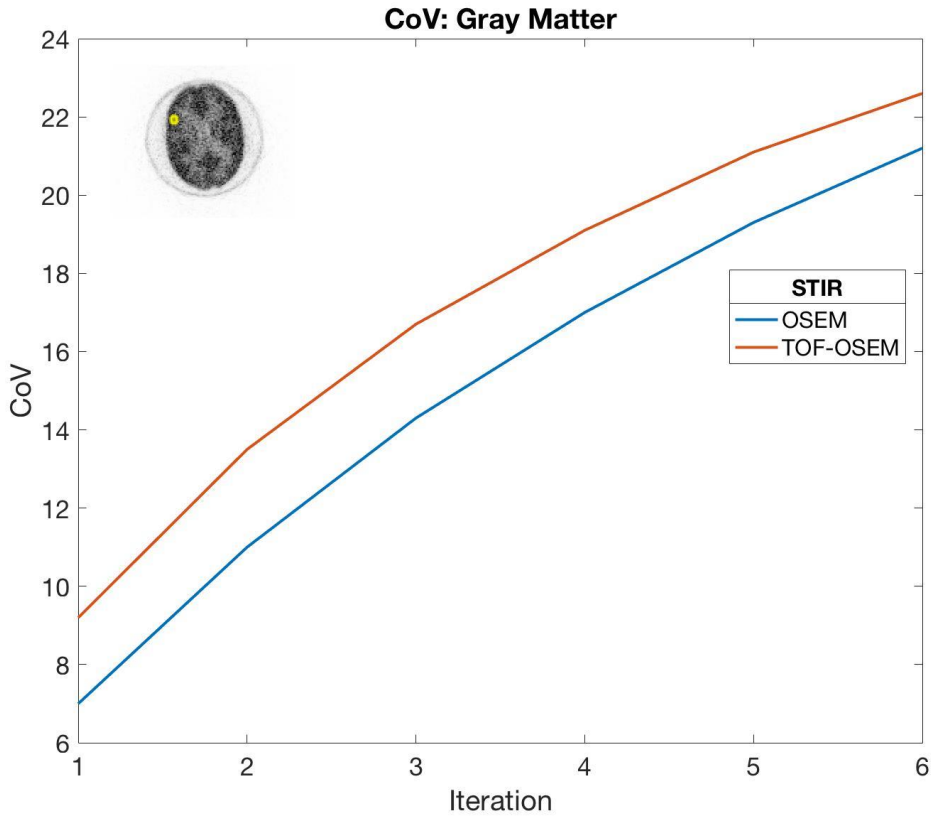

Figure 4.15: Hoffman Phantom: CoV comparisons for OSEM and TOF-OSEM with STIR for ROI placed within the Gray Matter as shown in the top left corner of the image.

OSEM, TOF-OSEM and TOF-KEM algorithms with STIR for bottle phantom.

4.5.2 STIR vs. GE

Figure 4.18 shows CoV comparisons for a ROI placed within the spleen and liver of the patient dataset. Graphs (a) and (b) compare the CoV in ROI placed within spleen and liver respectively, for TOF-OSEM-STIR (TOF-OSEM with STIR), TOF-KEM-STIR (TOF-KEM with GE-toolbox) and TOF-OSEM-GE (VUE-point FX with GE-toolbox) algorithms. Graphs (c) and (d) compare the CoV

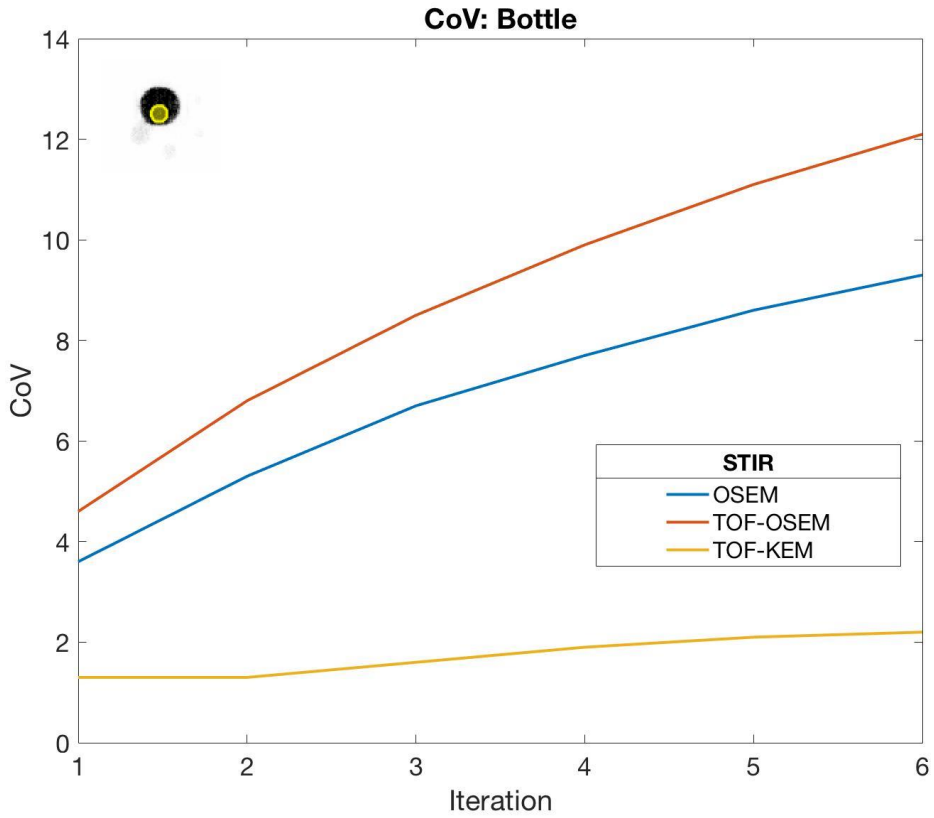

Figure 4.16: Bottle Phantom: CoV comparisons for OSEM, TOF-OSEM and TOF-KEM with STIR for ROI placed within the bottle as shown in the top left corner of the image.

in ROI placed within spleen and liver respectively, for PSF-TOF-OSEM-STIR (PSF-TOF-OSEM with STIR), PSF-TOF-KEM-STIR (PSF-TOF-KEM with STIR) and PSF-TOF-OSEM-GE (VUE-point FX SharpIR with GE-toolbox) algorithms.

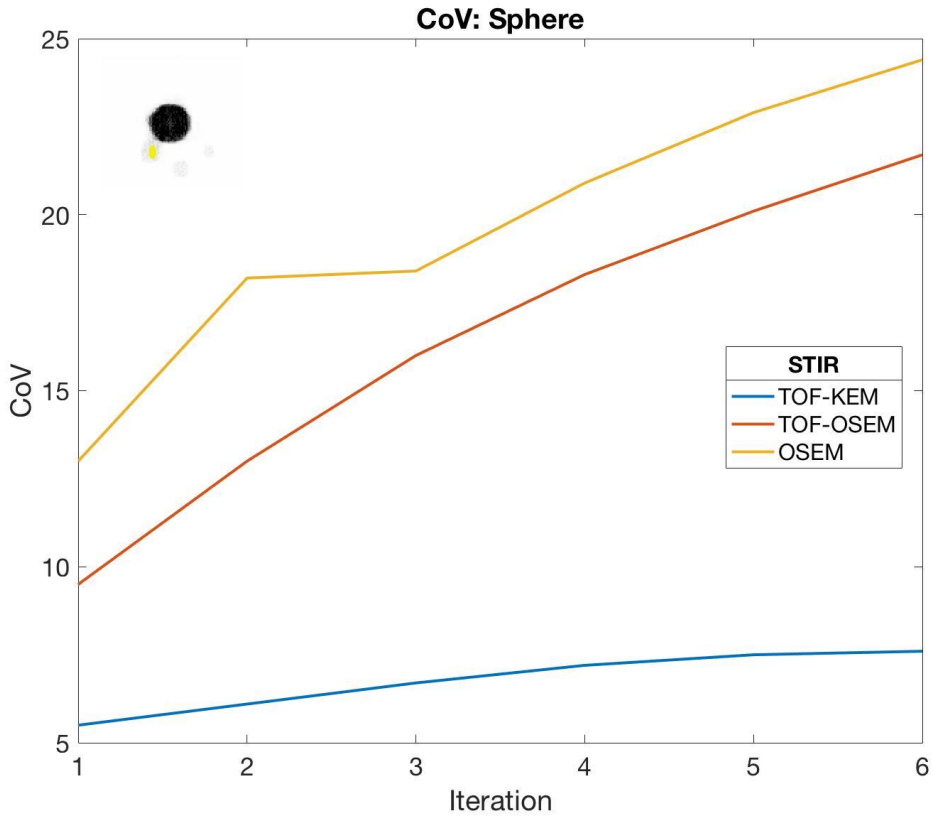

Figure 4.17: Bottle Phantom: CoV comparisons for OSEM, TOF-OSEM and TOF-KEM with STIR for ROI placed within the sphere as shown in the top left corner of the image.

4.6 Structural Similarity Index Measure (SSIM)

Table 4.7 compares the SSIM of the reconstructions that are obtained with the GE-toolbox (reference images) with the reconstructions that are obtained with STIR (distorted images). The reconstruction algorithms that are compared are: (a) TOF-OSEM-STIR (TOF-OSEM with STIR) and TOF-OSEM-GE (VUE-point FX with GE-toolbox) (b) TOF-KEM-STIR (TOF-KEM with STIR) and TOF-OSEM-GE (VUE-point FX with GE-toolbox) (c) PSF-TOF-OSEM-

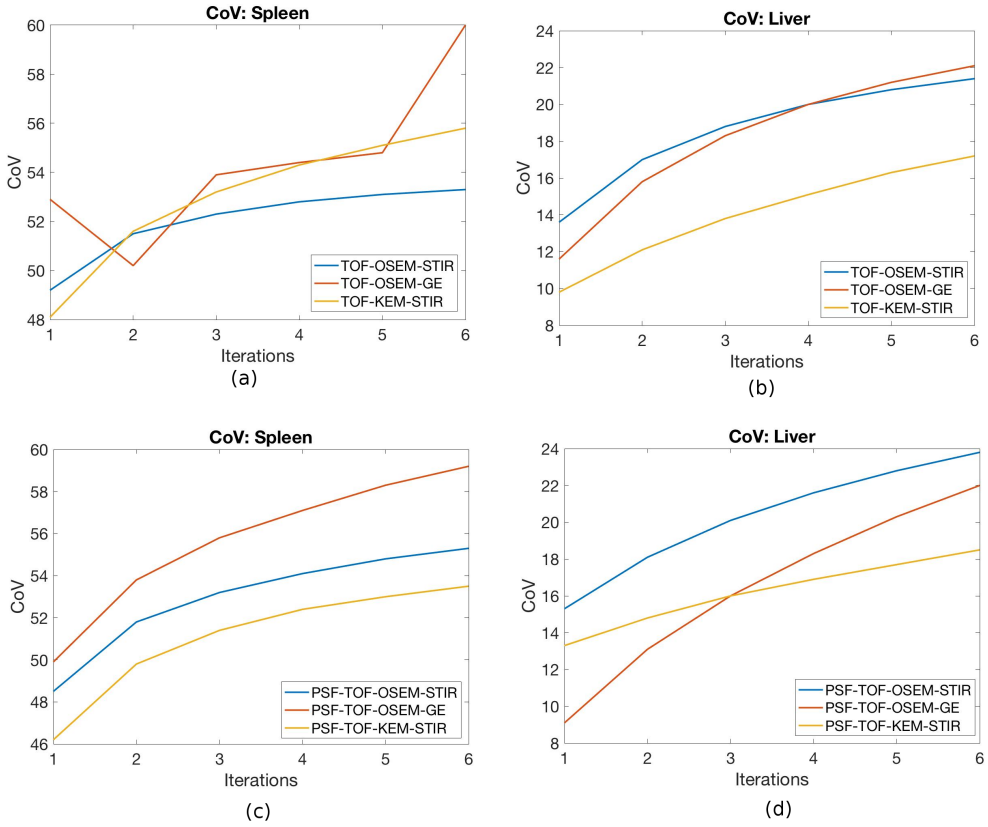

Figure 4.18: Patient Dataset: TOF-OSEM-STIR (TOF-OSEM with STIR), TOF-OSEM-GE (VUE-point FX with GE-toolbox) and TOF-KEM-STIR (TOF-KEM with STIR) comparisons for (a) CoV: Spleen; (b) CoV: Liver; PSF-TOF-OSEM-STIR (PSF-TOF-OSEM with STIR), PSF-TOF-OSEM-GE (VUE-point FX SharpIR with GE-toolbox) and PSF-TOF-KEM-STIR (PSF-TOF-KEM with STIR) comparisons for (c) CoV: Spleen; (d) CoV: Liver.

STIR (PSF-TOF-OSEM with STIR) and PSF-TOF-OSEM-GE (VUE-point FX SharpIR with GE-toolbox) (d) PSF-TOF-KEM-STIR (PSF-TOF-KEM with STIR) and PSF-TOF-OSEM-GE (VUE-point FX SharpIR with GE-toolbox). All these reconstructions are compared over first six iterations to observe the effect of iterations over distortions and thus, understand the effect of the increase

Table 4.7: SSIM Index

Compared Images	Iteration	Global SSIM value
TOF-OSEM-STIR	1	0.61
vs	2	0.85
TOF-OSEM-GE	3	0.85
	4	0.85
	5	0.84
	6	0.84
TOF-KEM-STIR	1	0.57
vs	2	0.85
TOF-OSEM-GE	3	0.84
	4	0.84
	5	0.84
	6	0.84
PSF-TOF-OSEM-STIR	1	0.84
vs	2	0.85
PSF-TOF-OSEM-GE	3	0.85
	4	0.85
	5	0.85
	6	0.84
PSF-TOF-KEM-STIR	1	0.83
vs	2	0.84
PSF-TOF-OSEM-GE	3	0.84
	4	0.84
	5	0.84
	6	0.84

of the statistical noise on the structure with the increase in iterations.

4.7 TOF-KEM: MR vs PET

This section compares the TOF-KEM reconstructions for patient dataset where kernel matrix is constructed with MR or PET images used as inputs.

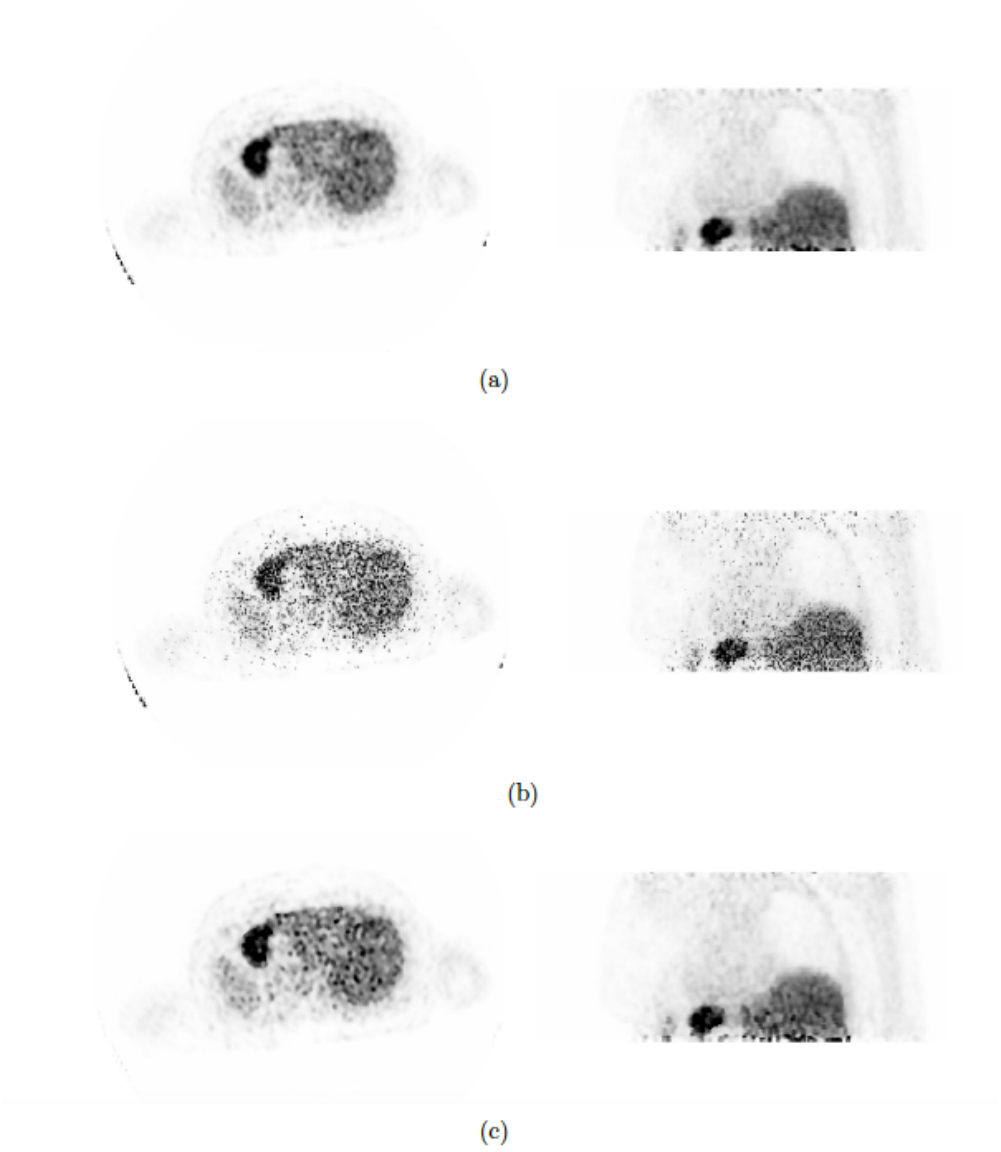

Figure 4.19: Patient Dataset: Transverse and coronal slice comparisons for (a) TOF-KEM-MR: TOF-KEM algorithm using MR as the input to construct kernel matrix. (b) TOF-KEM-PET (TOF-OSEM): TOF-KEM algorithm using TOF-OSEM (as shown in Figure 3.10 (a)) as the input to construct kernel matrix. (c) TOF-KEM-PET (TOF-OSEM+G): TOF-KEM algorithm using TOF-OSEM+G (as shown in Figure 3.10 (b)) as the input to construct kernel matrix. Comparisons are made for images reconstructed using STIR with 28 subsets and 2 iterations.

4.7.1 Comparison of Reconstructions

All the images in this section were reconstructed using STIR and with 28 subsets and 2 iterations. The images were reconstructed in $256 \times 256 \times 89$ matrix with the voxel size of $2.34 \times 2.34 \times 2.78\ mm^3$.

Figure 4.19 shows the transverse and coronal slices of the reconstructed images for the clinical datasetwith STIR. This figure has three sub-parts: (a) TOF-KEM-MR: TOF-KEM algorithm using MR as the input to construct kernel matrix. (b) TOF-KEM-PET (TOF-OSEM): TOF-KEM algorithm using TOF-OSEM (as shown in Figure 3.10 (a)) as the input to construct kernel matrix. (c) TOF-KEM-PET (TOF-OSEM+G): TOF-KEM algorithm using TOF-OSEM+G (as shown in Figure 3.10 (b)) as the input to construct kernel matrix.

TOF-OSEM and TOF-OSEM+G were used as PET inputs to construct kernel matrix and to compare the effect of noisy and noise filtered PET images on the reconstructed TOF-KEM images.

4.7.2 SUVR

Tables 4.8 and 4.9 show the SUVR comparisons for liver and spleen with respect to lungs for the clinical dataset reconstructed with STIR. The comparisons are made between:

1. TOF-KEM-MR: TOF-KEM algorithm using MR as the input to construct kernel matrix,

2. TOF-KEM-PET (TOF-OSEM): TOF-KEM algorithm using TOF-OSEM (as shown in Figure 3.10 (a)) as the input to construct kernel matrix,

3. TOF-KEM-PET (TOF-OSEM+G): TOF-KEM algorithm using TOF-OSEM+G (as shown in Figure 3.10 (b)) as the input to construct kernel matrix,
4. TOF-OSEM and
5. TOF-OSEM+G: TOF-OSEM post-filtered with Gaussian filter having the FWHM of 4mm.

All comparisons are made for reconstructions obtained with 28 subsets and 6 iteration.

Table 4.8: SUVR(liver/lung) Comparisons: Patient Dataset

Algorithm:STIR	SUVR
TOF-KEM-MR	21.3
TOF-KEM-PET (TOF-OSEM)	21.4
TOF-KEM-PET (TOF-OSEM+G)	21.3
TOF-OSEM	20.9
TOF-OSEM+G	20.9

Table 4.9: SUVR(spleen/lung) Comparisons: Patient Dataset

Algorithm:STIR	SUVR
TOF-KEM-MR	38.7
TOF-KEM-PET (TOF-OSEM)	39
TOF-KEM-PET (TOF-OSEM+G)	38.8
TOF-OSEM	38.2
TOF-OSEM+G	37.6

4.7.3 CoV

Figure 4.20 shows CoV comparisons for a ROI placed within the spleen and liver of the patient dataset. Graphs (a) and (b) compares following iterative algorithms for spleen and liver respectively:

1. TOF-KEM-MR: TOF-KEM algorithm using MR as the input to construct kernel matrix,

2. TOF-KEM-PET (TOF-OSEM): TOF-KEM algorithm using TOF-OSEM (as shown in Figure 3.10 (a)) as the input to construct kernel matrix,

3. TOF-KEM-PET (TOF-OSEM+G): TOF-KEM algorithm using TOF-OSEM+G (as shown in Figure 3.10 (b)) as the input to construct kernel matrix,

4. TOF-OSEM and

5. TOF-OSEM+G: TOF-OSEM post-filtered with Gaussian filter having the FWHM of 4mm.

4.8 TOF-KEM PET/MR

This section highlights the reconstructed images using novel iterative algorithm, TOF-KEM with GE SIGNA PET/MR scanner using MR Dixon 'in-phase' images as input to construct kernel matrix. The superimposed/fused image using TOF-KEM PET reconstruction and MR have been displayed in this section.

4.8.1 Bottle Phantom

Figure 4.21 shows (a) Transverse slice and (b) Coronal slice of MR Dixon 'in-phase' image (left column), Fused PET/MR image (middle column) and TOF-KEM PET reconstructed image (right column) for bottle phantom. TOF-KEM images were reconstructed using 28 subsets and 2 iterations and using STIR.

4.8.2 Patient Dataset

Figure 4.22 shows (a) Transverse slice and (b) Coronal slice of MR Dixon 'in-phase' image (left column), Fused PET/MR image (middle column) and TOF-KEM PET reconstructed image (right column) for patient dataset, respectively. TOF-KEM images were reconstructed using 28 subsets and 2 iterations and using STIR.

4.9 Summary

This chapter presents the results and comparisons of the image reconstruction conducted with STIR and GE-toolbox for clinical and advanced reconstruction algorithms. The next chapter discusses the results presented in this chapter.

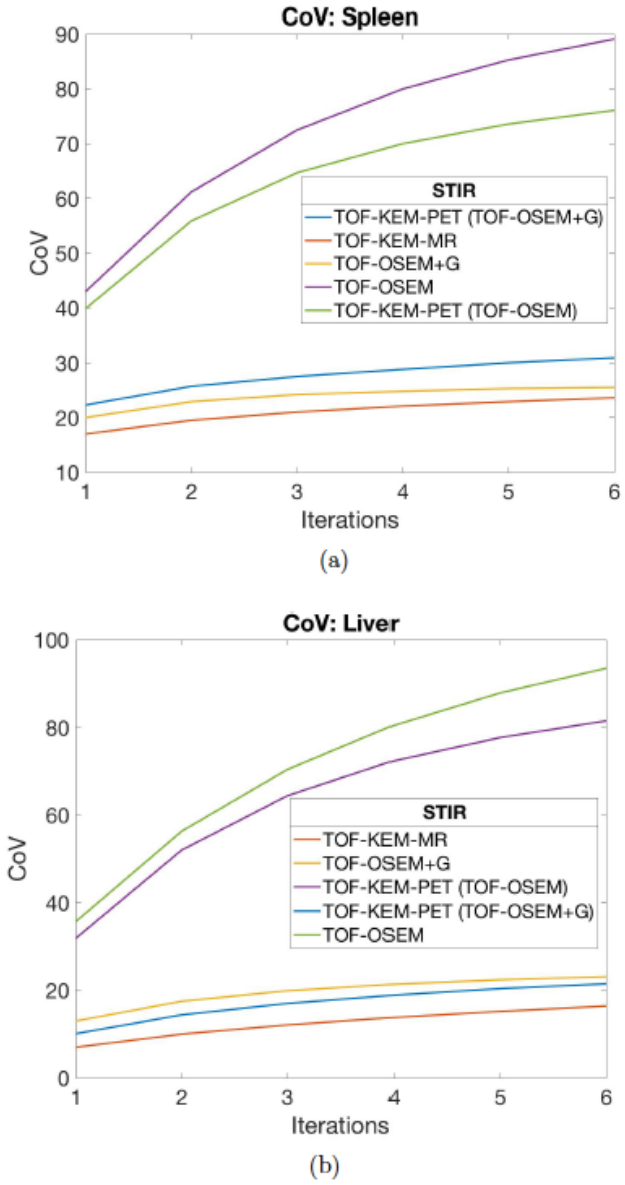

Figure 4.20: Patient Dataset: TOF-KEM-MR: TOF-KEM algorithm using MR as the input to construct kernel matrix; TOF-KEM-PET (TOF-OSEM): TOF-KEM algorithm using TOF-OSEM (as shown in Figure 3.10 (a)) as the input to construct kernel matrix; TOF-KEM-PET (TOF-OSEM+G): TOF-KEM algorithm using TOF-OSEM+G (as shown in Figure 3.10 (b)) as the input to construct kernel matrix; TOF-OSEM; and TOF-OSEM+G: TOF-OSEM post-filtered with Gaussian filter having the FWHM of 4mm with STIR comparisons for (a) CoV: Spleen; (b) CoV: Liver.

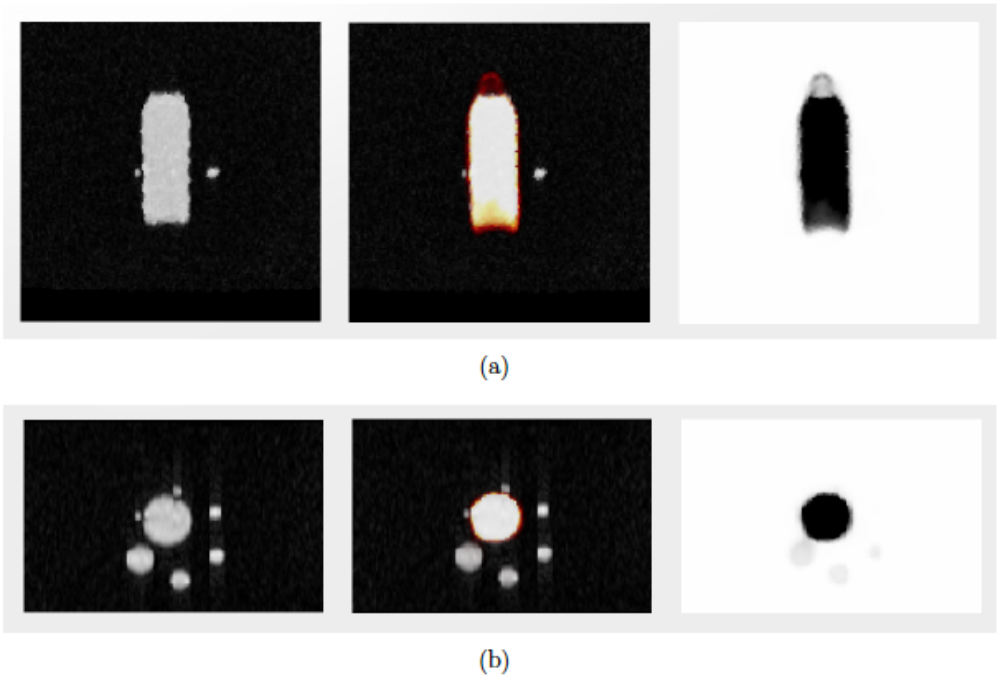

Figure 4.21: Bottle Phantom: (a) Transverse Slice and Coronal Slice of MR (left column), Fused PET/MR (middle column) and PET reconstruction (right column). The PET image displayed here is reconstructed using TOF-KEM-STIR (TOF-KEM algorithm with STIR) with 28 subsets and 2 iterations.

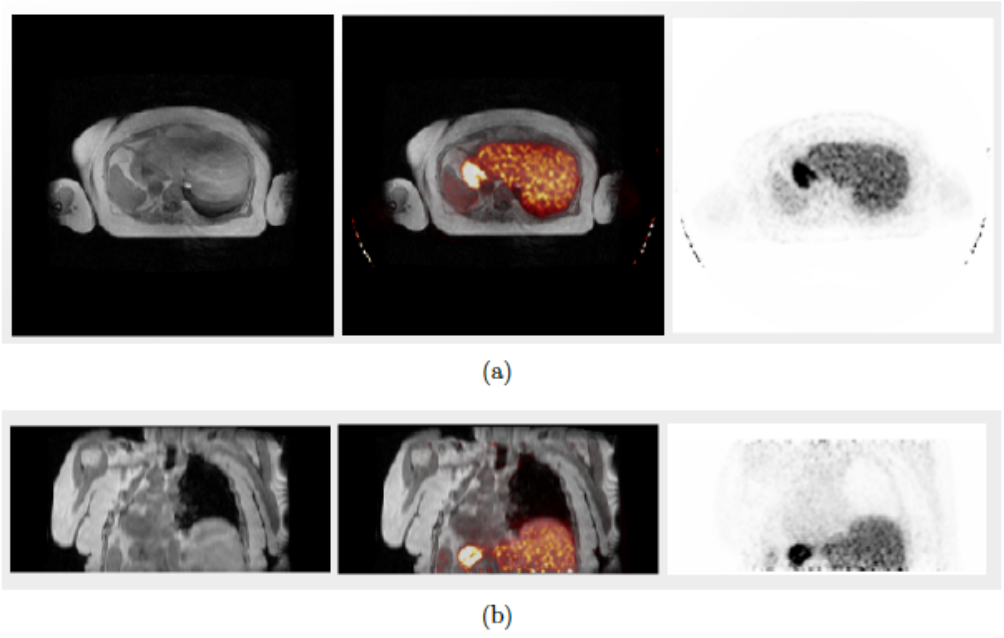

Figure 4.22: Patient Dataset: (a) Transverse Slice and Coronal Slice of MR (left column), Fused PET/MR (middle column) and PET reconstruction (right column). The PET image displayed here is reconstructed using TOF-KEM-STIR (TOF-KEM algorithm with STIR) with 28 subsets and 2 iterations.

Chapter 5

Discussion

This chapter focuses on discussing the results presented in the previous chapter. It indicates the achievements obtained during this thesis. It also contains the issues that are still unresolved despite the developments.

5.1 Histogram Comparisons

5.1.1 Non-TOF

The non-TOF histograms shown in Figure 4.1 illustrate the developments made in STIR for calculating emission, normalisation correction and randoms correction histograms. The top row shows the accurate binning of the LM data extracted from GE SIGNA PET/MR into the emission histogram in STIR space, as the histograms are identical. This demonstrates the accurate assignment of the detector pairs to the individual bins with the correctly calculated segment, axial, tangential and view positions in STIR.

The middle row of Figure 4.1 shows that the normalisation correction his-

tograms extracted from STIR and GE-toolbox are approximately equal as the range of differences is very small by a factor of $\pm 1.6 \times 10^{-7}$. This indicates that the normalisation factors calculated for each bin are accurate and are in correspondence with GE-toolbox calculations. Since the GE SIGNA PET/MR histogram has span 2, the LORs combined in a single bin due to compression is accurately estimated with the implementations described in Chapter 3, section 3.2.2. The difference between histograms extracted from STIR and GE-toolbox is due to the precision error (or errors arising due to rounding off huge numbers when stored in computer memory as different storage sizes which depend on the data type that is used to handle the numbers within the code).

The last row of the Figure 4.1 displays a difference of 0.6% to 1.1% in randoms histogram calculated with STIR and GE-toolbox. STIR calculates the randoms correction histogram using RFS method as described in Chapter 3, section 3.2.4. The differences observed in randoms correction histogram are due to the differences within randoms correction modelling between GE and STIR. GE models decay and dead-time correction within their randoms correction as can be seen in equation 2.31, whereas, this is ignored in STIR (Stearns et al. [2003], Stearns and Lonn [2011]). The randoms modelling implementation in STIR is not identical to the GE SIGNA PET/MR due to proprietary issues. Although the randoms correction modelling implemented in this thesis is not identical to GE-toolbox, the results demonstrate that the randoms calculations are not principally different. This is because the difference in modelling randoms correction within STIR and GE-toolbox lies at the lack of decay and dead-time correction within STIR, which is not of much relevance in clinical situations as those included within this thesis. Since, the scans included within this thesis are acquired for short time

and the decay of the injected activity is much below the half-life of the radioactive isotope, the decay correction factor is quite small as discussed by Stearns and Lonn (2011). Further, clinical scans do not have a high injected activity which can lead to high count rates and thus, the dead-time is also small (Stearns and Lonn [2011]).

5.1.2 TOF

As demonstrated in Figures 4.2 and 4.3, the TOF emission sinograms extracted with STIR and GE-toolbox are identical. This show that the sinograms are not only identical for different timing bin values but also across different datasets.

The identical results demonstrate that the timing information extracted from TOF-PET LM file with implementations made in this thesis is accurate. Thus, the functions implemented in STIR calculate the histogram dimensions (TOF bin value, segment number, axial position, tangential and view number) accurately using the LM measured data as input. These functions were modified iteratively during this study to calculate the correct map from LM event to STIR bin. Sections 3.3.2 to 3.3.4 describe the modifications that were required to achieve accurate mapping.

Also, it is seen that the number of LM events histogrammed in each bin of the histogram is equal to the GE-toolbox bin values. Thus, STIR reads all the LM events of the entire scan duration.

5.2 Comparison of Reconstructions: STIR and GE-toolbox

5.2.1 Non-TOF

The VQC phantom reconstruction as shown in Figure 4.4, the translation offsets between STIR and GE-toolbox. The GE-toolbox registers the PET image onto MR space automatically after reconstruction, whereas STIR does not follow this step, which implies images are in PET space. These offsets are also defined in the header of the LM file and are fixed manually. Apart from the translational offset, there is also rotation between the PET and MR gantries which is visible in the top row. The MRAC images used to correct for attenuation are in MR space whereas all reconstructions in STIR takes place in PET space. These alignment issues affect the attenuation correction as well in STIR, and its degrading effects are evident in the bottle phantom reconstructions with STIR.

The Hoffman and patient datasets reconstructed with OSEM with STIR and the GE-toolbox, as shown in Figures 4.6 to 4.9, show structural differences (as pointed in figures using red arrows). The figures also show noise differences. It is followed from discussion in Section 5.1 that the emission histograms are identical and normalisation histograms are almost identical with negligible differences with the two softwares, GE-toolbox and STIR. The inputs given to reconstruct image using OSEM algorithm as defined in equation 2.25 are measured projection data, system matrix and background correction data. This implies that the visible noise and structural differences as seen in Figures 4.6 to 4.9 result from differences in either of these given inputs. There are obvious differences in system matrix model between GE-toolbox and STIR, which particularly include

the lack of detector gap modelling within STIR and the different forward and back projectors in the two softwares. These detector gaps are not accounted for within the system matrix of STIR, as STIR considered only cylindrical geometries till recently (Khateri et al. [2019]). Further, as observed in Section 5.1, the randoms correction histograms has an observed small difference between STIR and GE-toolbox. These differences within system matrix modelling influence the final estimated image heavily, whereas, the differences within randoms correction are bound to produce smaller noise-based differences. Further, the reconstructed images are also influenced by the offset between MR and PET gantry which is not accounted for in this thesis. These visual comparisons set the initial scene for further quantitative comparisons and also allow to choose the metrics to be used for further investigation. Such as the noise based differences seen in the reconstructions are investigated further using the SUVR and CoV and the structural differences seen visually have been investigated using SUVR and SSIM.

There are further differences in the image reconstructions using point spread function (PSF). These differences are due to different PSF modelling between GE-toolbox and STIR. GE-toolbox applies a PSF kernel matrix in sinogram-space whereas STIR accounts for PSF correction by applying the PSF kernel matrix in image space (Thielemans et al. [2010]). Although there are visible differences in reconstructions, STIR is in good agreement with the GE-toolbox within the limitations mentioned earlier including lack of dead-time and detector gap modelling.

5.2.2 TOF

The bottle, Hoffman phantom and patient dataset as shown in Figures 4.10, 4.11 and 4.12, respectively, and reconstructed with the TOF-OSEM algorithm using STIR and GE-toolbox show differences in noise property of the images. The inputs given to reconstruct image using TOF-OSEM algorithm are measured TOF projection data, system matrix which includes TOF kernel and TOF background correction data. Since, TOF projection data is identical as can be seen in Figures 4.2 and 4.3, the differences in the images arise either from TOF kernel, system matrix or TOF background correction data. The TOF kernel was implemented and validated using simulated data by Efthimiou et. al. (2019). Thus, the differences in STIR reconstruction arise from lack of modelling of the detector gaps in STIR, differences in projectors between the two softwares and differences in the background correction term. Further with TOF-OSEM reconstruction, GE-toolbox uses TOF-scatter correction within the background correction term (Watson [2007]). Whereas, this correction is not applied within STIR and a primitive approximation using non-TOF scatter is used within background correction term in STIR.

The TOF-KEM-STIR (Figure 4.12 (c)) images demonstrate reduction in the background noise and visual improvement.

5.3 FWHM Comparisons

5.3.1 Non-TOF

Table 4.1 shows a the FWHM comparisons made between STIR and GE-toolbox. STIR and GE-toolbox reconstructions have a relative difference of 6.3% and 14%

for OSEM and PSF-OSEM reconstructions respectively. The FWHM comparisons show a more significant difference for PSF reconstructions between STIR and GE-toolbox because of different PSF implementations. Also, the kernel used in the STIR reconstructions is based on the resolution of the scanner calculated with GE-toolbox. The resolution achieved here is the best that could be achieved for this scanner in STIR due to the limitations including lack of detector gap modelling, different forward and back projectors and the lack of dead-time modelling. The lack of detector gap is due to the lack of STIR's ability to account for non-cylindrical geometries at the instance this work is produced. The differences in forward and back projectors occurs due to the reason that the GE-toolbox is a black-box and so the projectors used there are not known. The lack of dead-time modelling in STIR is due to the lack of proprietary information available.

5.3.2 TOF

Table 4.2 shows a relative difference of 5.6% and 9.5% for TOF-OSEM and PSF-TOF-OSEM between STIR and GE-toolbox. The reconstructions demonstrate similar resolution and good agreement for TOF reconstructions as well. The GE reconstructions demonstrate better resolution for TOF-OSEM, whereas STIR demonstrates better resolution for PSF-TOF-OSEM.

5.4 SUVR Comparisons

5.4.1 Non-TOF

Table 4.3 displays SUVR comparison for the reconstructions with OSEM and PSF-OSEM between GE-toolbox and STIR for ROI drawn within the liver. The

SUVR calculated for OSEM is identical with STIR and GE-toolbox. Whereas, SUVR calculated for PSF-OSEM shows a relative difference of 9.3% between STIR and GE-toolbox.

Table 4.4 displays SUVR comparisons for the reconstructions with OSEM and PSF-OSEM between GE-toolbox and STIR for ROI drawn within the spleen. The SUVR calculated for OSEM shows a much greater relative difference of 21.4% between STIR and GE-toolbox. Whereas, PSF-OSEM algorithm shows a good agreement and the calculated SUVR value is identical.

The much greater relative difference of 21.4% are due to the major differences in system matrix modelling, whereas, as small proportion of this relative difference is contributed by the difference in background correction data between two softwares.

The above comparisons show that STIR reconstructions demonstrate relatively accurate quantification assuming GE-toolbox is the ground truth. The residual differences are perhaps due to differences in system matrix, scatter and random modelling.

5.4.2 TOF

Tables 4.5 and 4.6 demonstrate that SUVR comparisons between GE-toolbox and STIR for TOF reconstructions have greater relative differences. SUVR comparisons for liver/lung, demonstrate a relative difference of 27.5% for TOF-OSEM and 33.5% for PSF-TOF-OSEM algorithms. For spleen/lung comparisons, there is a relative difference of 13% and 27% for TOF-OSEM and PSF-TOF-OSEM algorithms, respectively.

SUVR comparisons for TOF reconstructions further shows that the lack of

TOF scatter implementation in STIR has a detrimental effect on the quantification Watson [2007].

TOF-KEM reconstructions display a very slight improvement in terms of the quantification from TOF-OSEM algorithm with STIR. Although TOF-KEM shows slight quantitative improvement compared to TOF-OSEM-STIR, the lack of TOF scatter degrade its overall quantification as compared to TOF-OSEM-GE.

5.5 CoV

5.5.1 Non-TOF vs. TOF

Figure 4.14 shows that TOF-OSEM demonstrate less CoV over OSEM for ROI placed within the white matter of the Hoffman phantom.

Figure 4.15 shows that OSEM demonstrate less CoV over TOF-OSEM for ROI placed within the gray matter of the Hoffman phantom.

Figures 4.16 and 4.17 show that TOF-KEM demonstrates better performance over TOF-OSEM and OSEM as it has the lowest CoV over iterations. It can also be seen from Figure 4.17 that TOF-OSEM perform better by improving image uniformity over OSEM. Although, this is not true for the ROI placed in the bottle and the Figure 4.16 shows that OSEM has better uniformity over TOF-OSEM.

The TOF-OSEM conclusively demonstrates better performance in regions of lower activity as compared to OSEM, whereas, OSEM tend to perform better in higher activity regions.

5.5.2 STIR vs. GE

Figure 4.18 (a) shows the behaviour of TOF-OSEM algorithm with STIR and GE-toolbox and TOF-KEM algorithm with STIR over iterations using CoV. The figure demonstrates that for higher iterations, TOF-OSEM-STIR has the least value for CoV and thus, has the maximum uniformity. Whereas, TOF-KEM-STIR has maximum uniformity for iterations 1 and 2. The figure also shows that STIR reconstructions show less CoV over GE reconstruction when the ROI is within the spleen.

Figure 4.18 (b) shows that the TOF-KEM algorithm has the maximum uniformity as compared to TOF-OSEM algorithms. The graph also shows that TOF-OSEM-GE demonstrates the most deviation from the mean activity for higher iterations.

Figure 4.18 (c) demonstrates that with the application of the PSF kernel, all three reconstructions show similar behaviour over iterations. The graph also shows that PSF-TOF-KEM-STIR demonstrates maximum uniformity.

Figure 4.18 (d) shows that PSF-TOF-KEM-STIR demonstrates maximum uniformity for higher iterations.

Toolbox reconstructions show the maximum increase in CoV over iterations. There is an increase of 58.6% in the CoV over the iterations for PSF-TOF-OSEM-GE algorithm, which implies the toolbox reconstructions have the least uniformity. Overall there is a good agreement between TOF-OSEM-STIR and TOF-OSEM-GE with and without PSF. Kernel method shows an overall decrease in CoV. The KEM has maximum uniformity which perhaps could be because of prior anatomical information which distributes the activity uniformly in the region of interest.

5.6 SSIM

In order to investigate the visible structural differences, global SSIM values were calculated. The global SSIM value is between 0.84-0.85 for most comparisons performed on reconstructed images over six iterations. The values of global SSIM mentioned above shows a high structural similarity between STIR and GE reconstructed images for TOF imaging. The difference between the pairs of images is due to the intensity difference between the two images.

This study does not take into account TOF scatter correction, which gives rise to differences in noise properties (as observed in) between STIR and GE reconstructions. The randoms correction modelling implemented in STIR is not identical to that in GE toolbox. Global scaling of 10^6 and well counter calibration factor (section 2.1.10) are applied at the end of reconstruction and to the reconstructed activity image by GE-toolbox. This multiplicative factor is not automated within STIR reconstructions for GE SIGNA PET/MR. The lack of a complete account of this multiplicative factor manifests as the residual difference in image intensities. There is a relative difference of 12% to 35% between STIR and GE-toolbox image intensities at the sixth iteration.

Table 4.7 also demonstrates an improvement in structural similarity with an increase in iterations. Whereas, the results demonstrate lower SSIM value, and thus a greater structural distortion, for the first iteration. This indicates that STIR and GE-toolbox reconstruction perform differently to each other at the first iteration.

Table 4.7 also indicates that the TOF-KEM algorithms do not show any improvement in structural similarity as compared to TOF-OSEM algorithms.

5.7 TOF-KEM: MR vs. PET

Figure 4.19 shows the visual comparison of TOF-KEM reconstructions with kernel matrix constructed using MR and PET images. The effect of noisy PET image used as an input to construct kernel matrix can be seen in Figure 4.19 (b). It can be pointed out that the noise properties of the kernel matrix input image is directly reflected in the TOF-KEM reconstructions.

Table 4.8 shows an increase in quantification with TOF-KEM over TOF-OSEM by 1.8%, irrespective of the input image.

Table 4.9 shows a slightly greater increase in the quantification with TOF-KEM-PET (TOF-OSEM) over TOF-OSEM by 2.09% as compared to an increase of 1.5% for TOF-KEM-MR.

Figure 4.20 shows that the TOF-OSEM image is the least uniform, whereas, TOF-KEM-MR is the most uniform image. The figure also shows that TOF-OSEM+G performs better that TOF-KEM-PET (TOF-OSEM). The graph shows that for second iteration, TOF-KEM-MR improves the unifromity by 45% as compared to TOF-OSEM. This reflects the nature of TOF-KEM-MR algorithm which reduces the noise within PET reconstructions by including anatomical prior information from MR images.

The thesis demonstrates that lower noise images can be obtained using TOF-KEM-MR images over TOF-KEM-PET. Although, TOF-KEM-MR reduces the noise substantially within the reconstructions as compared to TOF-KEM-PET, the SUVR values are not much different.

Further, using PET as input image to construct kernel defeats the purpose to introduce anatomical prior information as not much prior anatomical information is introduced by using PET input image. The effect of noisy PET images as

inputs within TOF-KEM algorithm also demonstrate higher CoV over TOF-OSEM+G.

5.8 Summary

This chapter discusses the results of the investigations and explains the findings in detail. The next chapter presents an overall summary of the thesis and proposes future research.

Chapter 6

General Conclusion and Future Work

6.1 Summary

This thesis describes the physical and mathematical modelling of the acquisition process for the GE SIGNA PET/MR and demonstrates reconstruction with anatomically informed algorithms for TOF-PET data. The contributions made in this thesis demonstrate the first instance of TOF-PET reconstruction for real data with the STIR library. The thesis also presents the first instance of reconstruction with the TOF-KEM algorithm. Before the work presented in this thesis, reconstructions of the raw data extracted from GE SIGNA PET/MR was solely possible with the vendor's proprietary reconstruction software. With the developments presented here, the data extracted from the scanner can be reconstructed with open-source software which allows the validation of novel iterative reconstruction algorithms implemented in STIR with clinical datasets. It also

demonstrates the complexity of the implementations. It also presents the comparison of these developments with its counterparts extracted using the vendor's closed-source software (GE-toolbox).

Validation is made by comparing images reconstructed with iterative reconstruction algorithms available in the STIR library for acquired phantom and clinical datasets. Reconstructed images appear to be at a comparable level with the ones provided by the manufacturer. The reconstructed images also demonstrate comparable resolution to the reconstructions extracted from GE-toolbox. Dead-time correction, absence of detector gap modelling, differences in randoms modelling and lack of TOF scatter implementations may account for the observed discrepancies. This thesis demonstrates and compares reconstruction with TOF-KEM algorithms. It can be concluded that there is a slight improvement in quantification with the TOF-KEM algorithm as compared to TOF-OSEM algorithm with STIR. It can also be concluded that the TOF-KEM reconstructions do not distort the PET images (GE-toolbox reconstructions is used as reference) and hence, the anatomical kernels do not introduce structural bias. It can be finally concluded from the study, that TOF-KEM algorithm using MR anatomical image as kernel matrix input increases image uniformity substantially over TOF-OSEM with STIR. The modelling of the acquisition process in open-source software for a state-of-the-art scanner is beneficial for the scientific community to allow further research with the flexibility to manipulate data (Wadhwa et al. [2020]). This can help the researchers to implement new algorithms and test them using clinical dataset extracted from the GE scanner. These implementations can also pave the way for harmonisation of methodology across various PET scanners used in the clinic.

Overall, the purpose of this thesis, to reconstruct TOF-PET with anatomically informed reconstruction algorithms with open-source software, STIR is served. The developments made to expand STIR to reconstruct non-TOF and TOF PET data from the clinical GE SIGNA PET/MR scanner are demonstrated and validated.

6.2 Future Work

A natural extension of the work presented in this thesis is the incorporation of TOF scatter (Watson [2007]), modelling of the detector gaps (Khateri et al. [2019]) and implementation of dead-time modelling within random correction calculations. These implementations may show further improvement in image quantification with STIR. Further, the performance of TOF-KEM can be studied in a 10 clinical datasets that were collected as a part of the study carried out at Invicro. This extension of the current work will allow to validate the robustness and reproducibility of the results presented in this thesis. A more robust PET/MR motion correction method can also be investigated using these developments (Dikaios and Fryer [2009]).

With the implementation of the TOF-KEM algorithm and demonstration of clinical reconstruction for TOF-PET data from GE SIGNA PET/MR, there is a possibility of reducing the injected dose. TOF-KEM algorithm reduces image noise which increases its applicability for low dose clinical analysis. One of the significant clinical challenges with PET is lack of radiotracer availibility as compared to the patients required to be scan per day due to limited number of cyclotrons. The TOF-KEM algorithm reduces image noise and can be used to

reduce the injected dose by a factor of 10, which can increase patient throughput without adding more cyclotrons. The natural progression of this thesis can be an investigation which studies the effects of anatomical and TOF-PET information by reducing the injected dose.

The application of the TOF-KEM algorithm can be beneficial for kinetic analysis where short time frames are studied. In current scenario, dynamic images having time frame of $5 - 10$ s are used to study the tracer kinetics as the reconstructions are inadequate with less than 5 s time frames (Wang [2018]). Wang (2018) has demonstrated that using the PET image reconstructed for the complete long acquisition as the input to construct kernel matrix can improve reconstructions for short time frames. This study can be extended using the outputs of this thesis and long acquisitions can be used to reconstruct short time frames using TOF-KEM algorithm. TOF-KEM algorithm can be further extended to combine more that two modalities or multiple MR sequences so that maximum anatomical information can be used to reconstruct PET data (Deidda et al. [2018a]). The kernel method is also used to reconstruct PET data with direct parametric reconstruction (Tsoumpas and Thielemans [2009]).

6.3 Conclusion

The thesis concludes that the implementations made to expand STIR to read GE data from the scanner is accurate. It can be concluded that emission and data corrections calculated using the STIR library are in good agreement with the scanner even though the randoms modelling implemented within STIR is primitive. This study reports the modifications needed to read data from the GE

SIGNA PET/MR data directly into STIR and demonstrates successful reconstructions within the given limitations. It can also be concluded that the novel iterative reconstruction algorithm, TOF-KEM, demonstrates improved quantification and substantially improved uniformity within reconstructed images as compared to clinically-used algorithm, TOF-OSEM. The work conducted during the study presented in this thesis shows reconstructed images using real TOF-PET data extracted from GE SIGNA PET/MR scanner within open source library, STIR for the first time. The developments presented here will finally allow future investigations with TOF-PET data from any scanner and will also provide a platform to study novel iterative algorithms such as TOF-KEM with TOF-PET data.

Bibliography

S. Ahn, S. G. Ross, E. Asma, J. Miao, X. Jin, L. Cheng, S. D. Wollenweber, and R. M. Manjeshwar. Quantitative Comparison of OSEM and Penalized Likelihood Image Reconstruction Using Relative Difference Penalties for Clinical PET. *Physics in Medicine and Biology*, 60:5733–5751, 2015.

M. Akerele, P. Wadhwa, S. Vandenberghe, and C. Tsoumpas. Comparison of Partial Volume Correction Techniques for Lesions Near High Activity Regions. In *2017 IEEE Nuclear Science Symposium and Medical Imaging Conference (NSS/MIC)*, pages 1–7. IEEE, 2017.

E. A. Akin and D. A. Torigian. Considerations Regarding Radiation Exposure in Performing FDG-PET-CT. *Image Wisely*, 2012.

N. Alie, M. Eldib, Z. A. Fayad, and V. Mani. Inflammation, Atherosclerosis, and Coronary Artery Disease: PET/CT For the Evaluation of Atherosclerosis and Inflammation. *Clinical Medicine Insights: Cardiology*, 8:CMC–S17063, 2014.

G. Antoch and A. Bockisch. Combined PET/MRI: A New Dimension in Whole-body Oncology Imaging? *European Journal of Nuclear Medicine and Molecular Imaging*, 36(1):113–120, 2009.

E. Asma, S. Ahn, S. G. Ross, A. Chen, and R. M. Manjeshwar. Accurate and Consistent Lesion Quantitation with Clinically Acceptable Penalized Likelihood Images. In *IEEE Nuclear Science Symposium and Medical Imaging Conference Record Conference*, pages 4062–4066. IEEE, 2012.

D. L. Bailey, D. W. Townsend, P. E. Kinahan, S. Grootoonk, and T. Jones. An Investigation of Factors Affecting Detector and Geometric Correction in Normalization of 3-D PET Data. *IEEE Transactions on Nuclear Science*, 43: 3300 – 3307, 1996.

H. H. Barrett, D. W. Wilson, and B. M. W. Tsui. Noise Properties of the EM Algorithm. I. Theory. *Physics in Medicine and Biology*, 39(5):833, 1994.

H. H. Barrett, T. White, and L. C. Parra. List-mode Likelihood. *Journal of the Optical Society of America. A, Optics, Image Science, and Vision*, 14(11): 2914–2923, 1997.

E. Bastiaannet, H. Groen, P. L. Jager, D. C. P. Cobben, W. T. A. Van Der Graaf, W. Vaalburg, and H. J. Hoekstra. The Value of FDG-PET in the Detection, Grading and Response to Therapy of Soft Tissue and Bone Sarcomas; A Systematic Review and Meta-analysis. *Cancer Treatment Reviews*, 30(1):83–101, 2004.

T. Beisel, S. Lietsch, and K. Thielemans. A Method for OSEM PET Reconstruction on Parallel Architectures Using STIR. In *2008 IEEE Nuclear Science Symposium Conference Record*, pages 4161–4168. IEEE, 2008.

O. Bertolli, S. Arridge, C. W. Stearns, S. D. Wollenweber, B. F. Hutton, and K. Thielemans. Data Driven Respiratory Signal Detection in PET Taking

Advantage of Time-of-Flight Data. In *2016 IEEE Nuclear Science Symposium, Medical Imaging Conference and Room-Temperature Semiconductor Detector Workshop (NSS/MIC/RTSD)*, pages 1–3. IEEE, October 2016. Event-place: Strasbourg, France.

N. Bissantz, B. A. Mair, and A. Munk. A Multi-scale Stopping Criterion for MLEM Reconstructions in PET. In *IEEE Nuclear Science Symposium and Medical Imaging Conference Record*, volume 6, pages 3376–3379. IEEE, 2006.

T. M. Blodgett, C. C. Meltzer, and D. W. Townsend. PET/CT: Form and Function. *Radiology*, 242(2):360–385, 2007.

M. Blume. Expectation Maximization for Emission Tomography. Technical University of Munich, 2008. URL `Accessedat:http://campar.in.tum.de/twiki/pub/Main/MoritzBlume/EMPET.pdf`.

R. Boellaard, M. J. O'Doherty, W. A. Weber, F. M. Mottaghy, M. N. Lonsdale, S. G. Stroobants, W. J. G. Oyen, J. Kotzerke, O. S. Hoekstra, J. Pruim, P. K. Marsden, K. Tatsch, C. J. Hoekstra, E. P. Visser, B. Arends, F. J. Verzijlbergen, J. M. Zijlstra, E. F. I. Comans, A. A. Lammertsma, A. M. Paans, A. T. Willemsen, T. Beyer, A. Bockisch, C. Schaefer-Prokop, D. Delbeke, R. P. Baum, A. Chiti, and B. J. Krause. FDG PET and PET/CT: EANM Procedure Guidelines for Tumour PET Imaging: Version 1.0. *European Journal of Nuclear Medicine and Molecular Imaging*, 37(1):181, 2010.

R. Boellaard, I. Rausch, T. Beyer, G. Delso, M. Yaqub, and H. H. Quick. Quality Control for Quantitative Multicenter Whole-body PET/MR Studies: A

NEMA Image Quality Phantom Study with Three Current PET/MR Systems. *Medical Physics*, 42:5961–5969, 2015.

N. E. Bolus, R. George, and B. R. Newcomer. PET/MRI: The Blended-modality Choice of the Future? *Journal of Nuclear Medicine Technology*, 37(2):63–71, 2009.

S. L. Bowen, N. Fuin, M. A. Levine, and C. Catana. Transmission Imaging for Integrated PET-MR Systems. *Physics in Medicine and Biology*, 61(15):5547, 2016.

R. Brown, S. Ellis, E. Pasca, E. Ovtchinnikov, A. Gillman, C. Munoz, J. Bland, A. Mehranian, C. Prieto, A. J. Reader, and K. Thielemans. SIRF: A Research Tool for Rapid Prototyping of PET-MR Reconstruction. In *Abstracts of PSMR2019*, Munich, Germany, April 2019.

R. R. Buechel, P. A. Kaufmann, and O. Gaemperli. Single-photon emission computed tomography. *Advanced Cardiac Imaging*, pages 47–69, 2015.

M. E. Casey and E. J. Hoffman. Quantitation in Positron Emission Computed Tomography: 7. A Technique to Reduce Noise in Accidental Coincidence Measurements and Coincidence Efficiency Calibration. *Journal of Computer Assisted Tomography*, 10(5):845–850, 1986.

C. Catana. Motion Correction Options in PET/MRI. In *Seminars in Nuclear Medicine*, volume 45, pages 212–223. Elsevier, 2015.

Y. Chen and H. An. Attenuation Correction of PET/MR Imaging. *Magnetic Resonance Imaging Clinics*, 25(2):245–255, 2017.

M. Conti. Why is TOF PET Reconstruction a More Robust Method in the Presence of Inconsistent Data? *Physics in Medicine and Biology*, 56(1):155, 2010.

M. Conti. Focus on Time-Of-Flight PET: The Benefits of Improved Time Resolution. *European Journal of Nuclear Medicine and Molecular Imaging*, 38(6): 1147–1157, 2011.

B. D. Coombs, J. Szumowski, and W. Coshow. Two-point Dixon Technique for Water-fat Signal Decomposition with B0 Inhomogeneity Correction. *Magnetic Resonance in Medicine*, 38(6):884–889, 1997.

J. Czernin and H. Schelbert. PET/CT Imaging: Facts, Opinions, Hopes, and Questions. *The Journal of Nuclear Medicine*, 45:1S, 2004.

M. Defrise, D. E. Townsend, D. Bailey, A. Geissbuhler, C. Michel, and T. Jones. A Normalization Technique for 3D PET Data. *Physics in Medicine and Biology*, 36:939 – 952, 1991a.

M. Defrise, D. W. Townsend, D. Bailey, A. M. C. Geissbuhler, and T. Jones. A Normalization Technique for 3D PET Data. *Physics in Medicine and Biology*, 36(7):939, 1991b.

M. Defrise, P. E. Kinahan, and C. J. Michel. Image Reconstruction Algorithms in PET. In *Positron Emission Tomography*, pages 63–91. Springer, 2005.

D. Deidda, R. G. Aykroyd, and C. Tsoumpas. Multiplexing Kernelized Expectation Maximization Reconstruction for PET-MR. In *2018 IEEE Nuclear Science Symposium and Medical Imaging Conference Proceedings (NSS/MIC)*, pages 1–4. IEEE, 2018a.

D. Deidda, N. Karakatsanis, P. M. Robson, N. Efthimiou, Z. A. Fayad, R. G. Aykroyd, and C. Tsoumpas. Effect of PET-MR Inconsistency in the Kernel Image Reconstruction Method. *IEEE Transactions on Radiation and Plasma Medical Sciences*, 3:400–409, 2018b.

D. Deidda, N. A. Karakatsanis, P. M. Robson, Y. Tsai, N. Efthimiou, K. Thielemans, Z. A. Fayad, R. G. Aykroyd, and C. Tsoumpas. Hybrid PET-MR List-mode Kernelized Expectation Maximization Reconstruction. *Inverse Problems*, 35(4):044001, 2019.

G. Delso, S. Fürst, B. Jakoby, R. Ladebeck, C. Ganter, S. G. Nekolla, M. Schwaiger, and S. I. Ziegler. Performance Measurements of the Siemens mMR Integrated Whole-body PET/MR Scanner. *Journal of Nuclear Medicine*, 52(12):1914–1922, 2011a.

G. Delso, S. Fürst, B. Jakoby, R. Ladebeck, C. Ganter, S. G. Nekolla, M. Schwaiger, and S. I. Ziegler. Performance Measurements of the Siemens mMR Integrated Whole-body PET/MR Scanner. *Journal of Nuclear Medicine*, 52:1914 – 1922, 2011b.

A. P. Dempster, N. M. Laird, and D. B. Rubin. Maximum Likelihood from Incomplete Data via the EM Algorithm. *Journal of the Royal Statistical Society: Series B (Methodological)*, 39(1):1–22, 1977.

N. Dikaios and T. D. Fryer. Respiratory Motion Correction of PET Using Motion Parameters from MR. In *2009 IEEE Nuclear Science Symposium Conference Record (NSS/MIC)*, pages 2806–2808. IEEE, 2009.

N. Efthimiou, E. Emond, P. Wadhwa, C. Cawthorne, C. Tsoumpas, and

K. Thielemans. Implementation and Validation of Time-of-Flight PET Image Reconstruction Module for Listmode and Sinogram Projection Data in the STIR Library. *Physics in Medicine and Biology*, 64(3):035004, 2019.

E. C. Ehman, G. B. Johnson, J. E. Villanueva-Meyer, S. Cha, A. P. Leynes, P. E. Z. Larson, and T. A. Hope. PET/MRI: Where might it replace PET/CT? *Journal of Magnetic Resonance Imaging*, 46(5):1247–1262, 2017.

F. H. Fahey. Data Acquisition in PET Imaging. *Journal of Nuclear Medicine and Technology*, 30:39–49, 2002.

J. A. Fessler. ASPIRE 3.0 user's guide: A Sparse Iterative Reconstruction Library. Technical report, Citeseer, 1995.

J. A. Fessler. Michigan Image Reconstruction Toolbox, 2018.

A. Gaitanis, G. Kontaxakis, G. Spyrou, G. Panayiotakis, and G. Tzanakos. PET Image Reconstruction: A Stopping Rule for the MLEM Algorithm Based on Properties of the Updating Coefficients. *Computerized Medical Imaging and Graphics*, 34(2):131–141, 2010.

N. Gillings. Radiotracers for Positron Emission Tomography Imaging. *Nuclear Magnetic Resonance Material Physics*, 26:149–158, 2013.

S. E. Goelz, B. Vogelstein, and A. P. Feinberg. Hypomethylation of DNA from Benign and Malignant Human Colon Neoplasms. *Science*, 228(4696):187–190, 1985.

A. M. Grant, T. W. Deller, M. M. Khalighi, S. H. Maramraju, G. Delso, and C. S. Levin. NEMA NU 2-2012 Performance Studies for the SiPM-based ToF-

PET Component of the GE SIGNA PET/MR System: PET Performance Measurements of the GE SIGNA PET/MR. *Medical Physics*, 43(5):2334–2343, 2016.

R. N. Gunn, M. Slifstein, G. E. Searle, and J. C. Price. Quantitative Imaging of Protein Targets in the Human Brain with PET. *Physics in Medicine and Biology*, 60(22):R363, 2015.

J. Hamill and T. Bruckbauer. Iterative Reconstruction Methods for High-throughput PET Tomographs. *Physics in Medicine and Biology*, 47(15):2627, 2002.

B. E. Hammer, N. L. Christensen, and B. G. Heil. Use of a Magnetic Field to Increase the Spatial Resolution of Positron Emission Tomography. *Medical Physics*, 21(12):1917–1920, 1994.

K. Herholz and W-D. Heiss. Positron Emission Tomography in Clinical Neurology. *Molecular Imaging and Biology*, 6(4):239–269, 2004.

E. J. Hoffman, P. D. Cutler, W. M. Digby, and J. C. Mazziotta. 3-D Phantom to Simulate Cerebral Blood Flow and Metabolic Images for PET. *IEEE Transactions on Nuclear Science*, 37:616 – 620, 1990.

D. F. C. Hsu, E. Ilan, W. T. Peterson, J. Uribe, M. Lubberink, and C. S. Levin. Studies of a Next-generation Silicon-Photomultiplier–based Time-Of-Flight PET/CT System. *Journal of Nuclear Medicine*, 58(9):1511–1518, 2017.

H. M. Hudson and R. S. Larkin. Accelerated Image Reconstruction Using Ordered Subsets of Projection Data. *IEEE Transactions on Medical Imaging*, 13 (4):601–609, 1994.

T. Ido, C. N. Wan, V. Casella, J. S. Fowler, A.P. Wolf, M. Reivich, and D.E. Kuhl. Labeled 2-deoxy-d-glucose Analogs. 18F-labeled 2-deoxy-2-fluoro-d-glucose, 2-deoxy-2-fluoro-d-mannose and 14C–2-deoxy-2-fluoro-d-glucose. *Journal of Labelled Compounds and Radiopharmaceuticals*, 14(2):175–183, 1978.

T. Ishikita, N. Oriuchi, T. Higuchi, G. Miyashita, Y. Arisaka, B. Paudyal, P. Paudyal, H. Hanaoka, M. Miyakubo, Y. Nakasone, A. Negishi, S. Yokoo, and K. Endo. Additional Value of Integrated PET/CT Over PET Alone in the Initial Staging and Follow up of Head and Neck Malignancy. *Annals of Nuclear Medicine*, 24(2):77–82, 2010.

C. J. Jaskowiak, J. A. Bianco, S. B. Perlman, and J. P. Fine. Influence of Reconstruction Iterations on 18F-FDG PET/CT Standardized Uptake Values. *Journal of Nuclear Medicine*, 46(3):424–428, 2005.

M. Jennings, L. G. Marcu, and E. Bezak. PET-specific Parameters and Radiotracers in Theoretical Tumour Modelling. *Computational and Mathematical Methods in Medicine*, 2015.

L. Jødal, C. Le Loirec, and C. Champion. Positron Range in PET Imaging: An Alternative Approach for Assessing and Correcting the Blurring. *Physics in Medicine and Biology*, 57(12):3931, 2012.

T. Jones. The Role of Positron Emission Tomography Within the Spectrum of Medical Imaging. *European Journal of Nuclear Medicine and Molecular Imaging*, 23(7):807–813, 1996.

T. Jones and D. W. Townsend. History and Future Technical Innovation in

Positron Emission Tomography. *Journal of Medical Imaging*, 4(1):011013, 2017.

M. S. Judenhofer, H. F. Wehrl, D. F. Newport, C. Catana, S. B. Siegel, M. Becker, A. Thielscher, M. Kneilling, M. P. Lichy, M. Eichner, K. Klingel, G. Reischl, S. Widmaier, M. Röcken, R. E. Nutt, H-J. Machulla, K. Uludag, S. R. Cherry, C. S. Claussen, and B. J. Pichler. Simultaneous PET-MRI: A New Approach for Functional and Morphological Imaging. *Nature Medicine*, 14(4):459–465, 2008.

S. I. Kabanikhin. Definitions and Examples of Inverse and Ill-posed Problems. *Journal of Inverse and Ill-Posed Problems*, 16(4):317–357, 2008.

G. J. Kelloff, J. M. Hoffman, B. Johnson, H. I. Scher, B. A. Siegel, E. Y. Cheng, B. D. Cheson, J. O'Shaughnessy, K. Z. Guyton, D. A. Mankoff, L. Shankar, S. M. Larson, C. C. Sigman, R. L. Schilsky, and D. C. Sullivan. Progress and Promise of FDG-PET Imaging for Cancer Patient Management and Oncologic Drug Development. *Clinical Cancer Research*, 11(8):2785–2808, 2005.

P. Khateri, J. Fischer, W. Lustermann, C. Tsoumpas, and G. Dissertori. Implementation of Cylindrical PET Scanners with Block Detector Geometry in STIR. *European Journal of Nuclear Medicine and Molecular Imaging Physics*, 6(1):15, 2019.

J. H. Kim, J. S. Lee, I-C. Song, and D. S. Lee. Comparison of Segmentation-Based Attenuation Correction Methods for PET/MRI: Evaluation of Bone and Liver Standardized Uptake Value with Oncologic PET/CT Data. *Journal of Nuclear Medicine*, 53(12):1878–1882, 2012.

O. Klein and Y. Nishina. Über die Streuung von Strahlung durch freie Elektronen nach der neuen relativistischen Quantendynamik von Dirac. *Zeitschrift für Physik*, 52(11-12):853–868, 1929.

A. Kolb, A. W. Sauter, L. Eriksson, A. Vandenbrouke, C. C. Liu, C. Levin, B. J. Pichler, and M. Rafecas. Shine-through in PET/MR Imaging: Effects of the Magnetic Field on Positron Range and Subsequent Image Artifacts. *Journal of Nuclear Medicine*, 56(6):951–954, 2015.

C. Kolbitsch, C. Prieto, C. Tsoumpas, and T. Schaeffter. A 3D MR-acquisition Scheme for Nonrigid Bulk Motion Correction in Simultaneous PET-MR. *Medical Physics*, 41(8Part1):082304, 2014.

G. Kontaxakis and G. Tzanakos. Study of the Convergence Properties of the EM Algorithm-A New Stopping Rule. In *IEEE Conference on Nuclear Science Symposium and Medical Imaging*, 1992.

J. Kwiecinski, D. Dey, S. Cadet, S-E. Lee, B. Tamarappoo, Y. Otaki, P. T. Huynh, J. D. Friedman, M. R. Dweck, D. E. Newby, M. Yun, H-J. Chang, P.J. Slomka, and D. S. Berman. Predictors of 18F-Sodium Fluoride Uptake in Patients with Stable Coronary Artery Disease and Adverse Plaque Features on Computed Tomography Angiography. *European Heart Journal-Cardiovascular Imaging*, 21(1):58–66, 2020.

A. A. Lammertsma. Forward to the Past: The Case for Quantitative PET Imaging. *Journal of Nuclear Medicine*, 58(7):1019–1024, 2017.

K. Lange and R. Carson. EM Reconstruction Algorithms for Emission and Trans-

mission Tomography. *Journal of Computer Assisted Tomography*, 8:306–316, 1984.

A. Lasocki and R. J. Hicks. How we read: The Combined Use of MRI and Novel PET Tracers for the Characterisation and Treatment Planning of Masses in Neuro-oncology. *Cancer Imaging*, 19(1):57, 2019.

R. M. Leahy and J. Qi. Statistical Approaches in Quantitative Positron Emission Tomography. *Statistics and Computing*, 10(2):147–165, 2000.

R. Levkovilz, D. Falikman, M. Zibulevsky, A. Ben-Tal, and A. Nemirovski. The Design and Implementation of COSEN, An Iterative Algorithm for Fully 3-D Listmode Data. *IEEE Transactions on Medical Imaging*, 20(7):633–642, 2001.

J. J. D. Lima. *Nuclear Medicine Physics Series in Medical Physics and Biomedical Engineering*. CRC Press, illustrated edition, 2016.

J. R. Lindner and A. Sinusas. Molecular Imaging in Cardiovascular Disease: Which methods, which diseases? *Journal of Nuclear Cardiology*, 20(6):990–1001, 2013.

J. S. Liow and S. C. Strother. Practical Tradeoffs Between Noise, Quantitation, and Number of Iterations for Maximum Likelihood-based Reconstructions. *IEEE Transactions on Medical Imaging*, 10:563–571, 1991.

Jorge Llacer and John D Meng. Matrix-based Image Reconstruction Methods for Tomography. *IEEE Transactions on Nuclear Science*, 32(1):855–864, 1985.

M. A. Lodge, D. P. Holt, P. E. Kinahan, D. F. Wong, and R. L. Wahl. Performance Assessment of a NaI (Tl) Gamma Counter for PET Applications with

Methods for Improved Quantitative Accuracy and Greater Standardization. *European Journal of Nuclear Medicine and Molecular Imaging Physics*, 2(1): 11, 2015.

C. Lois, H. Sari, A. B. Sidwell, and J. C. Price. PET and PET/MRI Methods. In *Neuroimaging in Schizophrenia*, pages 125–143. Springer, 2020.

P. M. Matthews, E. A. Rabiner, J. Passchier, and R. N. Gunn. Positron Emission Tomography Molecular Imaging for Drug Development. *British Journal of Clinical Pharmacology*, 73(2):175–186, 2012.

M. E. Mayerhoefer, H. Prosch, L. Beer, D. Tamandl, T. Beyer, C. Hoeller, D. Berzaczy, M. Raderer, M. Preusser, M. Hochmair, B. Kiesewetter, C. Scheuba, A. Ba-Ssalamah, G. Karanikas, J. Kesselbacher, G. Prager, K. Dieckmann, S. Polterauer, M. Weber, I. Rausch, B. Brauner, H. Eidherr, W. Wadsak, and A. R. Haug. PET/MRI versus PET/CT in Oncology: A Prospective Single-center Study of 330 Examinations Focusing on Implications for Patient Management and Cost Considerations. *European Journal of Nuclear Medicine and Molecular Imaging*, 47(1):51–60, 2020.

A. Mehranian and H. Zaidi. Impact of Time-of-Flight PET on Quantification Errors in MR Imaging–based Attenuation Correction. *Journal of Nuclear Medicine*, 56(4):635–641, 2015.

A. Mehranian, F. Kotasidis, and H. Zaidi. Accelerated Time-Of-Flight (TOF) PET Image Reconstruction Using TOF Bin Subsetization and TOF Weighting Matrix Pre-computation. *Physics in Medicine and Biology*, 61(3):1309, 2016.

S. R. Meikle, B. F. Hutton, D. L. Bailey, P. K. Hooper, and M. J. Fulham.

Accelerated EM Reconstruction in Total-body PET: Potential for Improving Tumour Detectability. *Physics in Medicine and Biology*, 39:1689–1704, 1994.

C. L. Melcher. Scintillation Crystals for PET. *Journal of Nuclear Medicine*, 41 (6):1051–1055, 2000.

W. W. Moses. Trends in PET Imaging. *Nuclear Instruments and Methods in Physics Research Section A: Accelerators, Spectrometers, Detectors and Associated Equipment*, 471(1-2):209–214, 2001.

W. W. Moses. Time of Flight in PET Revisited. *IEEE Transactions on Nuclear Science*, 50(5):1325–1330, 2003.

H. Motara, T. Olusoga, G. Russell, S. Jamieson, S. Ahmed, N. Brindle, A. Pillai, A. F. Scarsbrook, C. N. Patel, and F. U. Chowdhury. Clinical Impact and Diagnostic Accuracy of 2-[18F]-fluoro-2-deoxy-d-glucose Positron-Emission Tomography/Computed Tomography (PET/CT) Brain Imaging in Patients with Cognitive Impairment: A Tertiary Centre Experience in the UK. *Clinical Radiology*, 72(1):63–73, 2017.

J. F. Oliver and M. Rafecas. Modelling Random Coincidences in Positron Emission Tomography by Using Singles and Prompts: A Comparison Study. *PloS one*, 11:e0162096, 2016.

E. Ovtchinnikov, R. Brown, C. Kolbitsch, E. Pasca, C. da Costa-Luis, A. G. Gillman, B. A. Thomas, N. Efthimiou, J. Mayer, P. Wadhwa, M. J. Ehrhardt, S. Ellis, J. S. Jørgensen, J. Matthews, C. Prieto, A. J. Reader, C. Tsoumpas, M. Turner, D. Atkinson, and K. Thielemans. SIRF: Synergistic Image Reconstruction Framework. *Computer Physics Communications*, 249:107087, 2020.

L. Parra and H. H. Barrett. Maximum-likelihood Image Reconstruction from List-mode Data. *Journal of Nuclear Medicine*, 37:486, 1996.

L. Parra and H. H. Barrett. List-mode Likelihood: EM Algorithm and Image Quality Estimation Demonstrated on 2-D PET. *IEEE Transactions on Medical Imaging*, 17(2):228–235, 1998.

M. Pennant, Y. Takwoingi, L. Pennant, C. Davenport, A. Fry-Smith, A. Eisinga, L. Andronis, T. Arvanitis, J. Deeks, and C. Hyde. A Systematic Review of Positron Emission Tomography (PET) and Positron Emission Tomography/-Computed Tomography (PET/CT) for the Diagnosis of Breast Cancer Recurrence. *NIHR Health Technology Assessment Programme*, 14(50), 2010.

I. Polycarpou, K. Thielemans, R. Manjeshwar, P. Aguiar, P. K. Marsden, and C. Tsoumpas. Comparative Evaluation of Scatter Correction in 3D PET Using Different Scatter-level Approximations. *Annals of Nuclear Medicine*, 25(9): 643–649, 2011.

P. M. Price and M. M. Green. Positron Emission Tomography Imaging Approaches for External Beam Radiation Therapies: Current Status and Future Developments. *The British Journal of Radiology*, 84(Special Issue 1):S19–S34, 2011.

A. J. Reader and H. Zaidi. Advances in PET Image Reconstruction. *PET clinics*, 2(2):173–190, 2007.

A. J. Reader, K. Erlandsson, M. A. Flower, and R. J. Ott. Fast Accurate Iterative Reconstruction for Low-statistics Positron Volume Imaging. *Physics in Medicine and Biology*, 43(4):835–846, 1998a.

A. J. Reader, K. Erlandsson, M. A. Flower, and R. J. Ott. Fast Accurate Iterative Three-dimensional Bayesian Reconstruction for Low-statistics Positron Volume Imaging. *IEEE Transactions on Nuclear Science*, 45(3):1090–1095, 1998b.

P. M. Robson, D. Dey, D. E. Newby, D. Berman, D. Li, Z. A. Fayad, and M. R. Dweck. MR/PET Imaging of the Cardiovascular System. *JACC: Cardiovascular Imaging*, 10(10 Part A):1165–1179, 2017a.

P. M. Robson, M. R. Dweck, M. G. Trivieri, R. Abgral, N. A. Karakatsanis, J. Contreras, U. Gidwani, J. P. Narula, V. Fuster, J. C. Kovacic, and Z. A. Fayad. Coronary Artery PET/MR Imaging. *JACC: Cardiovascular Imaging*, 10(10 Part A):1103–1112, 2017b.

S. Ross and C. Stearns. SharpIR. *White papers, GE Healthcare*, pages 1 – 8, 2010.

M. S. Rzeszotarski. The AAPM/RSNA Physics Tutorial for Residents 1: Counting Statistics. *Radiographics*, 19(3):765–782, 1999.

S. Sachs and T. V. Bilfinger. The Impact of Positron Emission Tomography on Clinical Decision Making in a University-based Multidisciplinary Lung Cancer Practice. *Chest*, 128(2):698–703, 2005.

J. J. Scheins and H. Herzog. PET Reconstruction Software Toolkit-PRESTO A Novel, Universal C++ Library for Fast, Iterative, Fully 3D PET Image Reconstruction using Highly Compressed, Memory-Resident System Matrices. In *2008 IEEE Nuclear Science Symposium Conference Record*, pages 4147–4150. IEEE, 2008.

C. Schiepers, F. Penninckx, N. De Vadder, E. Merckx, L. Mortelmans, G. Bormans, G. Marchal, L. Filez, and R. Aerts. Contribution of PET in the Diagnosis of Recurrent Colorectal Cancer: Comparison with Conventional Imaging. *European Journal of Surgical Oncology (EJSO)*, 21(5):517–522, 1995.

L. A. Shepp and Y. Vardi. Maximum Likelihood Reconstruction for Emission Tomography. *IEEE Transactions on Medical Imaging*, 1:113 – 122, 1982.

D. L. Snyder and M. I. Miller. The Use of Sieves to Stabilize Images Produced with the EM Algorithm for Emission Tomography. *IEEE Transactions on Nuclear Science*, 32(5):3864–3872, 1985.

D. L. Snyder and D. G. Politte. Image Reconstruction from List-mode Data in an Emission Tomography System Having Time-of-Flight Measurements. *IEEE Transactions on Nuclear Science*, 30(3):1843–1849, 1983.

D. L. Snyder, M. I. Miller, L. J. Thomas, and D. G. Politte. Noise and Edge Artifacts in Maximum-likelihood Reconstructions for Emission Tomography. *IEEE Transactions on Medical Imaging*, 6(3):228–238, 1987.

J. Stasa and M. Rajer. The Role of PET-CT in Radiotherapy Planning of Solid Tumors. *Radiology and Oncology*, 49(1):1–9, 2015.

C. W. Stearns and A. H. R. Lonn. Randoms From Singles Estimation for Long PET Scans. In *2011 IEEE Nuclear Science Symposium Conference Record*, pages 3739–3741. IEEE, 2011.

C. W. Stearns, D. L. McDaniel, S. G. Kohlmyer, P. R. Arul, B. P. Geiser, and V. Shanmugam. Random Coincidence Estimation from Single Event Rates on

the Discovery ST PET/CT Scanner. In *IEEE Nuclear Science Symposium and Medical Imaging Conference*, volume 5, page 3067–3069, 2003.

S. Surti. Update on Time-of-Flight PET Imaging. *Journal of Nuclear Medicine*, 56(1):98–105, 2015.

M. Tarokh. Solving a Class of Nonlinear Inverse Problems Using a Feedback Control Approach. *Mathematical Problems in Engineering*, 2017.

L. Theodorakis, G. Loudos, V. Prassopoulos, C. Kappas, I. Tsougos, and P. Georgoulias. A Review of PET Normalization: Striving for Count Rate Uniformity. *Nuclear Medicine Communications*, 34(11):1033–1045, 2013.

K. Thielemans, R. M. Manjeshwar, C. Tsoumpas, and F. P. Jansen. A New Algorithm for Scaling of PET Scatter Estimates Using All Coincidence Events. In *2007 IEEE Nuclear Science Symposium Conference Record*, volume 5, pages 3586–3590. IEEE, 2007.

K. Thielemans, E. Asma, S. Ahn, R. M. Manjeshwar, T. Deller, S. G. Ross, C. W. Stearns, and A. Ganin. Impact of PSF Modelling on the Convergence Rate and Edge Behaviour of EM Images in PET. In *IEEE Nuclear Science Symposuim and Medical Imaging Conference*, pages 3267–3272. IEEE, 2010.

K. Thielemans, C. Tsoumpas, S. Mustafovic, T. Beisel, P. Aguiar, N. Dikaios, and M. W. Jacobson. STIR: Software for Tomographic Image Reconstruction Release 2. *Physics in Medicine and Biology*, 57:867–883, 2012.

D. W. Townsend, T. Beyer, and T. M. Blodgett. PET/CT Scanners: A Hardware Approach to Image Fusion. In *Seminars in Nuclear Medicine*, volume 33, pages 193–204. Elsevier, 2003.

Y-J. Tsai, G. Schramm, J. Nuyts, S. Ahn, C. W. Stearns, A. Bousse, S. Arridge, and K. Thielemans. Spatially-variant Strength for Anatomical Priors in PET Reconstruction. In *2017 IEEE Nuclear Science Symposium and Medical Imaging Conference (NSS/MIC)*, pages 1–4. IEEE, 2017.

C. Tsoumpas and K. Thielemans. Direct Parametric Reconstruction From Dynamic Projection Data in Emission Tomography Including Prior Estimation of the Blood Volume Component. *Nuclear medicine communications*, 30(7): 490–493, 2009.

C. Tsoumpas, P. Aguiar, K. S. Nikita, D. Ros, and K. Thielemans. Evaluation of the Single Scatter Simulation Algorithm Implemented in the STIR Library. In *IEEE Symposium Conference Record Nuclear Science 2004.*, volume 6, pages 3361–3365. IEEE, 2004.

C. Tsoumpas, P. Aguiar, D. Ros, N. Dikaios, and K. Thielemans. Scatter Simulation Including Double Scatter. In *IEEE Nuclear Science Symposium Conference Record, 2005*, volume 3. IEEE, 2005.

T. G. Turkington and J. M. Wilson. Attenuation Artifacts and Time-of-Flight PET. In *2009 IEEE Nuclear Science Symposium Conference Record (NSS/MIC)*, pages 2997–2999. IEEE, 2009.

J. van Sluis, J. de Jong, J. Schaar, W. Noordzij, P. van Snick, R. Dierckx, R. Borra, A. Willemsen, and R. Boellaard. Performance Characteristics of the Digital Biograph Vision PET/CT System. *Journal of Nuclear Medicine*, 60 (7):1031–1036, 2019.

S. Vandenberghe and P. K. Marsden. PET-MRI: A Review of Challenges and

Solutions in the Development of Integrated Multimodality Imaging. *Physics in Medicine and Biology*, 60(4):R115, 2015.

S. Vandenberghe, E. Mikhaylova, E. D'Hoe, P. Mollet, and J. S. Karp. Recent Developments in Time-Of-Flight PET. *European Journal of Nuclear Medicine and Molecular Imaging physics*, 3(1):3, 2016.

D. Vandendriessche, J. Uribe, H. Bertin, and F. De Geeter. Performance Characteristics of Silicon Photomultiplier Based 15-cm AFOV TOF PET/CT. *European Journal of Nuclear Nedicine and Molecular Imaging Physics*, 6(1):8, 2019.

Y. Vardi, L. A. Shepp, and L. Kaufman. A statistical model for positron emission tomography. *Journal of the American Statistical Association*, 80(389):8–20, 1985.

E. Veklerov and J. Llacer. Stopping Rule for the MLE Algorithm Based on Statistical Hypothesis Testing. *IEEE Transactions on Medical Imaging*, 6(4): 313–319, 1987.

E. Veklerov, J. Llacer, and E. J. Hoffman. MLE Reconstruction of a Brain Phantom Using a Monte Carlo Transition Matrix and a Statistical Stopping Rule. *IEEE Transactions on Nuclear Science*, 35(1):603–607, 1988.

P. Wadhwa, K. Thielemans, O. Bertolli, N. Efthimiou, E. Emond, B. A. Thomas, M. Tohme, G. Delso, W. Hallett, R. Gunn, D. Buckley, and C. Tsoumpas. Implementation and Validation of Image Reconstruction for PET Data From GE SIGNA PET/MR Scanners In the STIR Library. *IEEE Nuclear Science Symposium and Medical Imaging Conference (NSS/MIC)*, 2018.

P. Wadhwa, K. Thielemans, N. Efthimiou, K. Wangerin, N. Keat, E. Emond, T. Deller, O. Bertolli, D. Deidda, G. Delso, et al. PET Image Reconstruction Using Physical and Mathematical Modelling For Time of Flight PET-MR Scanners in the STIR Library. *Methods*, 2020.

Z. Walker, F. Gandolfo, S. Orini, V. Garibotto, F. Agosta, J. Arbizu, F. Bouwman, A. Drzezga, P. Nestor, M. Boccardi, D. Altomare, C. Festari, and F. Nobili. Clinical Utility of FDG PET in Parkinson's Disease and Atypical Parkinsonism Associated with Dementia. *European Journal of Nuclear Medicine and Molecular Imaging*, 45(9):1534–1545, 2018.

G. Wang. High Temporal-resolution Dynamic PET Image Reconstruction Using a New Spatiotemporal Kernel Method. *IEEE Transactions on Medical Imaging*, 38(3):664–674, 2018.

G. Wang and J. Qi. PET Image Reconstruction Using Kernel Method. *IEEE Transactions on Medical Imaging*, 34(1):61–71, 2014.

Z. Wang, A. C. Bovik, H. R. Sheikh, and E. P. Simoncelli. Image Quality Assessment: From Error Visibility to Structural Similarity. *IEEE Transactions on Image Processing*, 13(4):600–612, 2004.

C. C. Watson. New, Faster, Image-based Scatter Correction for 3D PET. *IEEE Transactions on Nuclear Science*, 47(4):1587–1594, 2000.

C. C. Watson. Extension of Single Scatter Simulation to Scatter Correction of Time-of-Flight PET. *IEEE Transactions on Nuclear Science*, 54(5):1679–1686, 2007.

C. C. Watson, D. Newport, and M. E. Casey. A Single Scatter Simulation Technique for Scatter Correction in 3D PET. In *Three-dimensional image reconstruction in radiology and nuclear medicine*, pages 255–268. Springer, 1996.

C. Westbrook and C. Kaut. *MRI in Practice*. Blackwell Science, Oxford, 2nd edition edition, 1998. ISBN 0-632-04205-2.

C. B. Wilson, D. E. Snook, B. Dhokia, C. V. J. Taylor, I. A. Watson, A. A. Lammertsma, R. Lambrecht, J. Waxman, T. Jones, and A. A. Epenetos. Quantitative Measurement of Monoclonal Antibody Distribution and Blood Flow using Positron Emission Tomography and 124-Iodine in Patients with Breast Cancer. *International Journal of Cancer*, 47(3):344–347, 1991.

H. Zaidi. Scatter Modelling and Correction Strategies in Fully 3-D PET. *Nuclear Medicine Communications*, 22(11):1181–1184, 2001.

H. Zaidi and M-L. Montandon. Scatter Compensation Techniques in PET. *PET Clinics*, 2(2):219–234, 2007.

X. Y. Zhang, Z. L. Yang, G. M. Lu, G. F. Yang, and L. J. Zhang. PET/MR Imaging: New Frontier in Alzheimer's Disease and Other Dementias. *Frontiers in Molecular Neuroscience*, 10, 2017.

Appendix A

Software Implementation of Acquired Data for GE SIGNA PET/MR in STIR

This appendix provides the C++ code for the software implementations that were made in open-source software, STIR to make it compatible with acquired GE data. It also describes the software implementations specific to GE SIGNA PET/MR.

A.1 Reading the List of Events from LM File in STIR

The LM file extracted from the scanner is opened, and the stream of events is read as described in the C++ code here. Each coincidence event is read as a record and has four bytes.

```
Succeeded
CListModeDataGESigna::
open_lm_file()
{
  info(boost::format("CListModeDataGESigna: opening file %1%")
  % listmode_filename);
#if 0
  shared_ptr<std::istream> stream_ptr(new std::fstream(
  listmode_filename.c_str(), std::ios::in | std::ios::binary));

if (!(*stream_ptr))
    {
      return Succeeded::no;
    }

stream_ptr->seekg(12492704);
current_lm_data_ptr.reset(
new InputStreamWithRecords<CListRecordT, bool>(stream_ptr,
        4, 16,
        ByteOrder::little_endian != ByteOrder::get_native_order()));
#else

  if(!GEHDF5Wrapper::check_GE_signature(listmode_filename))
  {
     return Succeeded::no;
  }
#endif

  GEHDF5Wrapper inputFile(listmode_filename);
  shared_ptr<Scanner> tmp = inputFile.get_scanner_sptr();
```

```
  shared_ptr<ProjDataInfo> proj_data_tmp(ProjDataInfo::
  ProjDataInfoCTI(tmp,2,tmp->get_num_rings()-1,
  tmp->get_num_detectors_per_ring()/2,
  tmp->get_max_num_non_arccorrected_bins(),
  false));

  this->set_proj_data_info_sptr(proj_data_tmp);

  current_lm_data_ptr.
  reset(
        new InputStreamWithRecordsFromHDF5<CListRecordT>(
        listmode_filename, 6, 16));

  return Succeeded::yes;
}
```

A.2 Calculation of Emission Data

The code presented below demonstrates the implementations that were made to read the detector axial and transaxial positions and the timing bin information for each coincidence event within STIR. This information is further used to calculate the segment, axial, transaxial and view positions for respective events to map each event within the correct histogram bin in STIR.

```

#if STIRIsNativeByteOrderBigEndian
  // Do byteswapping first before using this bit field.
  TODO
#else
```

```
    boost::uint16_t eventLength:2;
    /* Event Length : Enum for the number of bytes in the event */
    boost::uint16_t eventType:1;
    /* Event Type : Coin or Extended types */
    boost::uint16_t hiXtalShortInteg:1;
    /* High Crystal Short Integration on / off */
    boost::uint16_t loXtalShortInteg:1;
    /* Low Crystal Short Integration on / off */
    boost::uint16_t hiXtalScatterRec:1;
    /* High Crystal Scatter Recovered on / off */
    boost::uint16_t loXtalScatterRec:1;
    /* Low Crystal Scatter Recovered on / off */
    boost::int16_t  deltaTime:9;
    /* TOF 'signed' delta time (units defined by electronics */
    boost::uint16_t hiXtalAxialID:6;
    /* High Crystal Axial Id */
    boost::uint16_t hiXtalTransAxID:10;
    /* High Crystal Trans-Axial Id */
    boost::uint16_t loXtalAxialID:6;
    /* Low Crystal Axial Id */
    boost::uint16_t loXtalTransAxID:10;
    /* Low Crystal Trans-Axial Id */
#endif
}; /*-coincidence event*/
```

A.2.1 Non-TOF

The detector positions read for each coincidence event as described in the code above is converted in STIR space. The tangential and axial coordinates for each detector pair read from the LM file is in scanner space. Although STIR and

scanner have the same conventions for axial detector numbering, it numbers the detectors with opposite conventions as compared to STIR along the tangential direction (demonstrated in Figure 3.5). This incongruity is accounted by flipping the crystal number as described in the code below (total number of crystals in tangential direction for GE SIGNA are 448, and they are numbered from 0 to 447): $447 - loXtalTransAxID$; $447 - hiXtalTransAxID$.

```
class CListEventDataGESigna
{
 public:
  inline bool is_prompt() const { return true; }
  inline Succeeded set_prompt(const bool prompt = true)
  {
    //if (prompt) random=1; else random=0; return Succeeded::yes;
    return Succeeded::no;
  }
  inline void get_detection_position(
  DetectionPositionPair<>&  det_pos) const
  {
    det_pos.pos1().tangential_coord() = 447 - loXtalTransAxID;
    det_pos.pos1().axial_coord() = loXtalAxialID;
    det_pos.pos2().tangential_coord() = 447 - hiXtalTransAxID;
    det_pos.pos2().axial_coord() = hiXtalAxialID;
  }
  inline bool is_event() const
    {
      return (eventType==COINC_EVT)
      /* && eventTypeExt==COINC_COUNT_EVT)*/;
     }
```

A.2.2 TOF

The TOF bin information is read for each event from the LM file for each coincidence event. This information is stored within the *deltaTime* field of the LM file as a signed bin number ranging from −175 to 175. The read TOF bin number from scanner space is converted into STIR space using: $detpos.timingpos() = get\_tof\_bin()$ for positive bin number and $detpos.timingpos() = -get\_tof\_bin()$ for negative bin number.

```
inline void get_detection_position(
DetectionPositionPair<>& det_pos) const
  {
    if (deltaTime<0)
    {
      det_pos.pos1().tangential_coord() = 447-loXtalTransAxID;
      det_pos.pos1().axial_coord() = loXtalAxialID;
      det_pos.pos2().tangential_coord() = 447-hiXtalTransAxID;
      det_pos.pos2().axial_coord() = hiXtalAxialID;
      det_pos.timing_pos() = -get_tof_bin();
    }
    else
    {
      det_pos.pos1().tangential_coord() = 447-hiXtalTransAxID;
      det_pos.pos1().axial_coord() = hiXtalAxialID;
      det_pos.pos2().tangential_coord() = 447-loXtalTransAxID;
      det_pos.pos2().axial_coord() = loXtalAxialID;
      det_pos.timing_pos() = get_tof_bin();
    }
  }
  inline bool is_event() const
```

```
    {
      return (eventType==COINC_EVT)
      /* && eventTypeExt==COINC_COUNT_EVT)*/;
     }
  inline int get_tof_bin() const
     {
         return static_cast<int>(deltaTime);
     }
private:
```

A.3 Reading the TOF Histogram Directly from the Scanner

The scanner not only stores emission data in the LM format but also stores it in histogram format. It stores the emission data within the TOF histogram, which is a series of viewgrams starting from viewgram 0 to viewgram 223. Each viewgram is stored as an array of size of $1981 \times 27 \times 357$. Each cell of the viewgram array is stored as an 8-bit unsigned character. An example of the histogram HDF5 structure is presented in Figure A.1.

Chunks of the data can be read from the array stored in the HDF5 file. The exact location of the chunk is obtained by defining the offset (which is the starting position of the chunk), count (which corresponds to the number of elements that are to be read), stride (which corresponds to the number of elements to be skipped within individual selected elements) and block (size of the block to be selected). A hyperslab defines this selected chunk of data.

The code below reads the histogram data as a list of the viewgram for each

view_num (view number) and accesses the array for each viewgram using the address: $m\_address$ = "$/SegmentData/\ Segment2/3D\_TOF\_Sinogram/view$". The *initialise_proj_data_data* function initialises each viewgram as an array within STIR by defining the dimensions of the hyperslab.

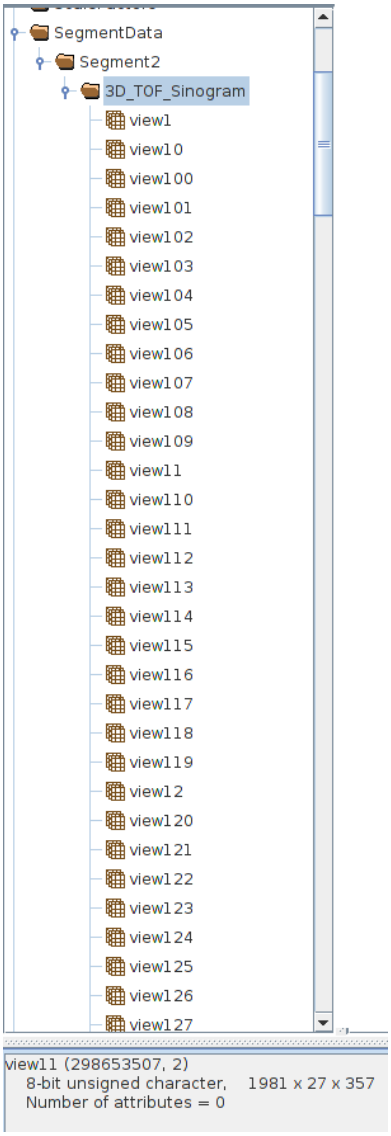

Figure A.1: This figure demonstrates an example of the HDF5 file opened with the HDF View application. The HDF5 file shown in this figure is an example of the 'rdf.1.1' file or the raw histogram file. The HDF5 files have a number of fields and each field can further have sub-fields.

```
Succeeded GEHDF5Wrapper::initialise_proj_data_data
(const std::string& path,  const unsigned int view_num)
{
    if(path.size() == 0)
    {
        if(is_signa)
        {
          m_address = "/SegmentData/Segment2/3D_TOF_Sinogram/view";
            if(view_num > 0)
            {
              std::ostringstream datasetname;
              datasetname << m_address << view_num;
              m_dataset_sptr.reset(new H5::DataSet(file.openDataSet
              (datasetname.str())));

              m_dataspace = m_dataset_sptr->getSpace();

            }

            {
                m_NX_SUB = 1981;     // hyperslab dimensions
                m_NY_SUB = 27;
                m_NZ_SUB = 357;
                m_NX = 45;          // output buffer dimensions
                m_NY = 448;
                m_NZ = 357;
            }
        }
        else
            return Succeeded::no;
```

```
    }
    else
        m_address = path;
    return Succeeded::yes; }
```

A hyperslab is selected and read as the output using the code below. Since the data is stored as an unsigned 8-bit character in the array as can be seen in figure A.1, the output is defined as *unsigned char*.

```
Succeeded GEHDF5Wrapper::get_from_dataset
(const std::array<unsigned long long int, 3>& offset,
 const std::array<unsigned long long int, 3>& count,
 const std::array<unsigned long long int, 3>& stride,
 const std::array<unsigned long long int, 3>& block,
 Array<1, unsigned char> &output)
{
    m_dataspace.selectHyperslab(H5S_SELECT_SET,
    count.data(), offset.data());
    m_memspace_ptr= new H5::DataSpace(3, count.data());
    m_dataset_sptr->read(output.get_data_ptr(),
    H5::PredType::STD_U8LE, *m_memspace_ptr, m_dataspace);
    output.release_data_ptr();
    return Succeeded::yes;
}
```

A viewgram buffer is initialised below to finally store the entire viewgram of size $224 \times 1981 \times 27 \times 357$ read from the acquired TOF histogram from the GE SIGNA PET/MR (as described in code above) within STIR.

```
void ProjDataFromHDF5::initialise_viewgram_buffer()
{
const unsigned int num_tof_poss = 27;
```

```
const unsigned int max_num_axial_poss = 1981;
const unsigned int get_num_viewgrams = 224;
unsigned int total_size = get_num_tangential_poss()
* num_tof_poss * max_num_axial_poss;

this->tof_data.resize(IndexRange4D(get_num_viewgrams,
get_num_tangential_poss(), num_tof_poss, max_num_axial_poss));

Array<1,unsigned char> buffer(total_size);

 for (int view_num = get_min_view_num();
 view_num <= get_max_view_num(); view_num++)
{
    m_input_hdf5_sptr->initialise_proj_data_data("", view_num + 1);

    std::array<unsigned long long int, 3> stride = {1, 1, 1};
    const std::array<unsigned long long int, 3> count
    = {max_num_axial_poss, num_tof_poss,
    static_cast<unsigned long long int>(get_num_tangential_poss())};

    std::array<unsigned long long int, 3> offset = {0,0,0};

    std::array<unsigned long long int, 3> block = {1, 1, 1};

m_input_hdf5_sptr->get_from_dataset(offset, count, stride,
block, buffer);

std::copy(buffer.begin(), buffer.end(),
tof_data[view_num].begin_all());
}
```

There is a segment incongruity between scanner and STIR space which is accounted in the code presented below (which is demonstrated in figure 3.5). This code defines a map between the scanner segment and STIR segment number for the GE scanners acquired data.

```
void ProjDataFromHDF5::initialise_segment_sequence()
{
    segment_sequence.resize(2*get_max_segment_num()+1);
    segment_sequence[0] = 0;

    for (int segment_num = 1; segment_num<=get_max_segment_num();
    ++segment_num)
    {
      segment_sequence[2*segment_num-1] = segment_num;
      segment_sequence[2*segment_num] =  -segment_num;
    }
}
```

The stored viewgrams are translated within STIR space using the code below.

```
Viewgram<float>
ProjDataFromHDF5::
get_viewgram(const int view_num, const int segment_num,
             const bool make_num_tangential_poss_odd) const
{
    if (make_num_tangential_poss_odd)
error("make_num_tangential_poss_odd_not_supported_by_Proj
DataFromHDF5");
    Viewgram<float> ret_viewgram =
    get_empty_viewgram(view_num, segment_num);
    ret_viewgram.fill(0.0);
```

```
    const unsigned int num_tof_poss = 27;
   // const unsigned int max_num_axial_poss = 1981;

    // PW Attempt to flip the tangential and view numbers.
   for (int tang_pos = ret_viewgram.get_min_tangential_pos_num(),
   i_tang = 0; tang_pos <= ret_viewgram.get_max_tangential_pos_num(),
   i_tang<=static_cast<unsigned long long int>
   (get_num_tangential_poss())-1; ++tang_pos, ++i_tang)
      for(int i_axial=0, axial_pos =
     seg_ax_offset[find_segment_index_in_sequence(segment_num)];
     i_axial<= static_cast<unsigned long long int>
     (get_num_axial_poss(segment_num))-1 ,
     axial_pos <= seg_ax_offset[find_segment_index_in_sequence
     (segment_num)]+
     static_cast<unsigned long long int>
     (get_num_axial_poss(segment_num))-1;
     i_axial++, axial_pos++)
        for (int tof_poss = 0; tof_poss <=
        num_tof_poss-1; tof_poss++)
       {
        ret_viewgram[i_axial][-tang_pos] +=
            static_cast<float> (tof_data[223-view_num][i_tang]
            [tof_poss][axial_pos]);
             }
    return ret_viewgram;
}
```

A.4 Implementation of Normalisation Correction in STIR

The normalisation effects acquired by the scanner after each scan are stored in HDF5 file as:

- Detection Efficiency Factors: These are stored as an array of size 448×45.
- Geometric Correction Factors: These are stored as a list of viewgrams of size 1981×357.

The code below reads the detection efficiency and geometric correction factors from the 'norm' file. The function that reads these factors is: *read_norm_data*. The function called '*get_bin_efficiency*' calculates the normalisation correction factors using equation 3.1 within STIR space.

```
void
BinNormalisationFromGEHDF5::
read_norm_data(const string& filename)
{
  m_input_hdf5_sptr.reset(new GEHDF5Wrapper(filename));
  this->scanner_ptr = m_input_hdf5_sptr->get_scanner_sptr();

  proj_data_info_cyl_uncompressed_ptr.reset(
    dynamic_cast<ProjDataInfoCylindricalNoArcCorr *>(
    ProjDataInfo::ProjDataInfoCTI(scanner_ptr,
    /*span=*/1, scanner_ptr->get_num_rings()-1,
    /*num_views,=*/scanner_ptr->get_num_detectors_per_ring()/2,
    /*num_tangential_poss=*/scanner_ptr->
    get_max_num_non_arccorrected_bins(),
    /*arc_corrected =*/false)
```

```
    ));

  efficiency_factors =
  Array<2,float>(IndexRange2D(0,scanner_ptr->get_num_rings()-1,
          0, scanner_ptr->get_num_detectors_per_ring()-1));



 {
  const int num_rings = scanner_ptr->get_num_rings();
  const int num_detectors_per_ring
  = scanner_ptr->get_num_detectors_per_ring();

  m_input_hdf5_sptr->initialise_efficiency_factors("");
  std::array<unsigned long long int, 2> stride = {1, 1};
  const std::array<unsigned long long int, 2> count  = {45, 448};
  std::array<unsigned long long int, 2> offset = {0,0};
  std::array<unsigned long long int, 2> block = {1, 1};
  unsigned int total_size = num_rings*num_detectors_per_ring;
  stir::Array<1, float> buffer(0, total_size-1);
  m_input_hdf5_sptr->get_from_2d_dataset(offset, count, stride,
  block, buffer);
  std::copy(buffer.begin(), buffer.end(),
  efficiency_factors.begin_all());
  }

geometric_factors =

   Array<3,float>(IndexRange3D(0, max_num_view_num-1, 0,
   max_num_axial_poss-1,
    min_tang_pos_num, max_tang_pos_num));
```

```
  {
  ret_array.resize(IndexRange3D
  (max_num_view_num,
  max_num_axial_poss, max_num_tangential_poss));

for(int i_view = 0;
i_view <= proj_data_info_cyl_uncompressed_ptr->get_max_view_num();
 ++i_view)
        {
        // Viewgram and geometric correction factors are
        initialised.

            m_input_hdf5_sptr->
            initialise_geo_factors_data("",modulo(i_view,16)+1);

        // Here the data is read from the HDF5 array.

            std::array<unsigned long long int, 2> stride = {1, 1};
            std::array<unsigned long long int, 2> count =
            {max_num_axial_poss, max_num_tangential_poss};
            std::array<unsigned long long int, 2> offset = {0, 0};
            std::array<unsigned long long int, 2> block = {1, 1};
            unsigned int total_size = max_num_axial_poss *
            max_num_tangential_poss;
            stir::Array<1, unsigned int> tmp(0, total_size-1);

            m_input_hdf5_sptr->get_from_2d_dataset(offset, count,
            stride, block, tmp);
            std::copy(tmp.begin(),tmp.end(),
```

```
            ret_array[i_view].begin_all());
}
            //PW Flip view and tangential positions here.

for(int view_num =
proj_data_info_cyl_uncompressed_ptr->get_min_view_num();
view_num <=
proj_data_info_cyl_uncompressed_ptr->get_max_view_num();
++view_num)

for (int tang_pos =
proj_data_info_cyl_uncompressed_ptr->get_min_tangential_pos_num(),
i_tang = 0; tang_pos <=
proj_data_info_cyl_uncompressed_ptr->get_max_tangential_pos_num(),
i_tang<=max_num_tangential_poss-1; ++tang_pos, ++i_tang)

for(int axial_pos = 0; axial_pos <= max_num_axial_poss-1;
axial_pos++)
      {
      geometric_factors[223-view_num][axial_pos][-tang_pos] =
      ret_array[view_num][axial_pos][i_tang];
     }
        //PW Currently the scale factors are hardcorded.
        //! \todo Get these from HDF5 file.
         geometric_factors *= 2.2110049e-4;
           }
}
```

```
float
BinNormalisationFromGEHDF5::
get_bin_efficiency(const Bin& bin, const double start_time,
const double end_time) const {
    const DetectionPosition<>& pos1 = detection_position_pair.pos1();
    const DetectionPosition<>& pos2 = detection_position_pair.pos2();

float lor_efficiency_this_pair = 1.F;

if (this->use_detector_efficiencies())
{
lor_efficiency_this_pair =1/
(efficiency_factors[pos1.axial_coord()][447-pos1.tangential_coord()]
* efficiency_factors[pos2.axial_coord()][447-pos2.tangential_coord()]);
}

if (this->use_geometric_factors())
  {
 //   int segment_num_span1 = uncompressed_bin.segment_num;
total_efficiency +=
view_efficiency*geometric_factors[uncompressed_bin.view_num()-1]
[find_axial_pos_in_span2_from_span1
(const_cast<Bin>(bin),uncompressed_bin)+
seg_ax_offset[find_segment_index_in_sequence
(find_segment_pos_in_span2_from_span1(const_cast<Bin>(bin),
uncompressed_bin))][uncompressed_bin.tangential_pos_num()];
  }
}
```

A.5 Implementation of Randoms Correction in STIR

The randoms correction factors are calculated using the single events that are stored within the LM HDF5 file. LM HDF5 file stores the singles for each second starting from the scan start time. The code below defines each second as a *slice* and reads the singles per slice for each detector pair.

```
unsigned int
SinglesRatesFromGEHDF5::
read_singles_from_listmode_file
(const std::string& _listmode_filename)
{

    unsigned int slice = 0;

    //PW Open the list mode file here.
    m_input_sptr.reset(new GEHDF5Wrapper(_listmode_filename));



    SinglesRates::scanner_sptr = m_input_sptr->get_scanner_sptr();
    // Get total number of bins for this type of scanner.
    const int total_singles_units =
    SinglesRates::scanner_sptr->get_num_singles_units();



    m_num_time_slices =
    m_input_sptr->get_exam_info_sptr()->
    get_time_frame_definitions().get_num_frames();
```

```
    // Allocate the main array.
    m_singles_sptr.reset
    (new Array<2, unsigned int>
    (IndexRange2D(0, m_num_time_slices - 1, 0,
    total_singles_units - 1)));

    m_input_sptr->initialise_singles_data();

    while ( slice < m_num_time_slices)
    {
        m_input_sptr->get_dataspace(slice+1,
        (*m_singles_sptr)[slice] );
        ++slice;
    }

    //PW Modify this bit of code too.
    if (slice != m_num_time_slices)
    {
error("\nSinglesRatesFromGEHDF5: Couldn't read all records in the
file. Read %d of %d. Exiting\n",
slice, m_num_time_slices);
        //TODO resize singles to return array with new sizes
    }

    _times = std::vector<double>(m_num_time_slices);
    for(unsigned int slice = 0;slice < m_num_time_slices;++slice)
        _times[slice] = slice+1.0;

    assert(_times.size()!=0);
    _singles_time_interval = _times[1] - _times[0];
```

```
    // Return number of time slices read.
    return slice;

}
```

The singles rate is read and stored within STIR space using the function called *read_singles_from_listmode_file* as implemented in the code above.

The code below calculates the randoms correction sinogram in STIR space using the singles rate.

```
DetectorEfficiencies
efficiencies(IndexRange2D(num_rings,
num_detectors_per_ring));

{
SinglesRatesFromGEHDF5  singles;
singles.read_singles_from_listmode_file
(_listmode_filename);
   // efficiencies
   if (true)
    {
       //singles.write(std::cout);
       for (int r=0; r<num_rings; ++r)
            for (int c=0; c<num_detectors_per_ring; ++c)
      {
            DetectionPosition<> pos(c,r,0);
            double time_init = 0.;
            int time_final =
            static_cast<double>
            (singles.get_num_time_slices());
```

```
        efficiencies[r][c]=
        singles.get_singles_rate(pos, time_init, time_final);
        }
  }


shared_ptr<GEHDF5Wrapper> m_input_sptr;
m_input_sptr.reset(new GEHDF5Wrapper(_listmode_filename));
int num_slices = m_input_sptr->get_exam_info_sptr()->
get_time_frame_definitions().get_num_frames();

Bin bin;
Bin uncompressed_bin;

for (bin.segment_num() = proj_data.get_min_segment_num();
 bin.segment_num() <= proj_data.get_max_segment_num();
 ++ bin.segment_num())
  {

for
(bin.axial_pos_num() = proj_data.get_min_axial_pos_num
(bin.segment_num());
bin.axial_pos_num() <= proj_data.get_max_axial_pos_num
(bin.segment_num());
++bin.axial_pos_num())
{
    Sinogram<float> sinogram =
    proj_data_info_ptr->get_empty_sinogram
    (bin.axial_pos_num(),bin.segment_num());
```

```
        const float out_m = proj_data_info_ptr->get_m(bin);

        const int in_min_segment_num
        =proj_data_info_ptr->get_min_ring_difference
        (bin.segment_num());

        const int in_max_segment_num =
        proj_data_info_ptr->
        get_max_ring_difference
        (bin.segment_num());

// now loop over uncompressed detector-pairs

        {
        for (uncompressed_bin.segment_num() = in_min_segment_num;
        uncompressed_bin.segment_num() <= in_max_segment_num;
        ++uncompressed_bin.segment_num())

        for (uncompressed_bin.axial_pos_num()
        = uncompressed_proj_data_info_ptr->
        get_min_axial_pos_num(uncompressed_bin.segment_num());
        uncompressed_bin.axial_pos_num() <=
        uncompressed_proj_data_info_ptr->
        get_max_axial_pos_num(uncompressed_bin.segment_num());
        ++uncompressed_bin.axial_pos_num() )
          {
            const float in_m = uncompressed_proj_data_info_ptr->
            get_m(uncompressed_bin);
            if (fabs(out_m - in_m) > 1E-4)
              continue;
```

```
// views etc
if (proj_data.get_min_view_num()!=0)
  error("Can only handle min_view_num==0\n");
for (bin.view_num() = proj_data.get_min_view_num();
 bin.view_num() <= proj_data.get_max_view_num();
 ++ bin.view_num())
  {

for (bin.tangential_pos_num() = -half_fan_size;
     bin.tangential_pos_num() <= half_fan_size;
     ++bin.tangential_pos_num())
  {
    uncompressed_bin.tangential_pos_num() =
      bin.tangential_pos_num();
    for (uncompressed_bin.view_num() =
    bin.view_num()*mashing_factor;
     uncompressed_bin.view_num() <
    (bin.view_num()+1)*mashing_factor;
     ++uncompressed_bin.view_num())
      {

    int ra = 0, a = 0;
    int rb = 0, b = 0;
    uncompressed_proj_data_info_ptr->
    get_det_pair_for_bin(a, ra, b, rb, uncompressed_bin);

    float coincidence_time_window = 0.00000000457f;
    /*(*segment_ptr)[bin.axial_pos_num()]*/
```

```
            sinogram[bin.view_num()][bin.tangential_pos_num()]
            +=
            num_slices*
            coincidence_time_window*
            efficiencies[ra][447-a]*
            efficiencies[rb][447-b%num_detectors_per_ring];
            }}}}
        }
        proj_data.set_sinogram(sinogram); }
```